POLITECNICO DI TORINO

Department of Mechanical and Aerospace Engineering

Master of Science in Automotive Engineering

ACADEMIC YEAR 2023/2024

Simulation of the dynamic behavior of a self-driving rover for off-road applications

Supervisor:
Prof. Aurelio Somà

Co-supervisor:
Dr. Francesco Mocera
Dr. Salvatore Martelli

Candidate:
Daniele Montagni

Acknowledgements

I wish to acknowledge the help provided by the staff in the DIMEAS of the Politecnico di Torino and the staff of Ecothea. I would also like to show my deep appreciation to my supervisor Professor Aurelio Somà who gives me the opportunity to work on this project and helped me finalize it. I would like to thank my co-supervisors Dr. Salvatore Martelli and Dr. Francesco Mocera for all their help and advice with this thesis, assisting and guiding me throughout this project.

Abstract

Technological advancements in agriculture are continuously evolving to meet the growing demand for food. In recent years, agricultural technology has been shifting towards a new paradigm: Agriculture 4.0. However, a new role within this system needs to be introduced. Various rover models have been developed in recent years to enable autonomous decision-making. This thesis focuses on studying the dynamic behavior of such vehicles in an environment that simulates real-world conditions, proposing improvements. The first phase explores the steering systems commonly adopted in agriculture, followed by a brief theoretical explanation of their operation, evaluating which system might yield better results theoretically. Subsequently, multi-body simulations are conducted to study the dynamic behavior, reporting contacts and a structure as close as possible to the real rover. For this purpose, a simplified model of an agricultural rover was developed using multi-body software. The study specifically compares the behavior of three rovers employing three different steering systems. At the end of the analysis, the best system from a dynamic perspective will be defined by observing variations in forces, lateral deviation, and other parameters that will be introduced, while also considering the feasibility of the existing model and the economic cost required for implementation.

Sommario

I progressi tecnologici in ambito agricolo sono in continua evoluzione per rispondere alla crescente domanda di viveri. Negli ultimi anni, la tecnologia agricola sta evolvendo verso un nuovo paradigma chiamato Agricoltura 4.0. Tuttavia, nonostante questo sistema sia già ben consolidato, è necessaria l'introduzione di una nuova figura. Negli ultimi anni, sono stati sviluppati diversi modelli di rover, progettati per attuare decisioni in modo autonomo. Questa tesi si concentra sull'analisi del comportamento dinamico di tali veicoli, simulando condizioni simili a quelle reali, con l'obiettivo di proporre dei miglioramenti. Nella prima fase, vengono analizzati i principali sistemi di sterzatura impiegati in agricoltura, seguiti da una breve spiegazione teorica sul loro funzionamento, per valutare quale sistema possa offrire i migliori risultati in teoria. Successivamente, vengono eseguite simulazioni multi-body per studiare il comportamento dinamico, riproducendo contatti e strutture il più possibile vicini al rover reale. A tal fine, è stato sviluppato un modello semplificato di rover agricolo utilizzando un software di simulazione multi-body. Lo studio si concentra sulla comparazione del comportamento di tre rover, ciascuno dotato di un diverso sistema di sterzatura. Al termine dell'analisi, verrà individuato il sistema migliore dal punto di vista dinamico, osservando le variazioni delle forze, le deviazioni laterali e altri parametri che verranno introdotti, prestando attenzione alla fattibilità del modello esistente e ai costi economici necessari per l'implementazione.

Contents

List of Figures

List of Tables

1 Introduction

Throughout human evolution, agriculture has consistently progressed along with population growth. Each increase in the number of people has been met with advances in production techniques. In the past centuries, particular attention has been paid to the gradual reduction of actual hours of human physical labor in the fields. This was achieved first with the introduction of animal labor as a source of energy, then with the use of steam-powered machinery, and finally with the development of the first prototype tractors, similar to those still in use today.

Figure 1.1: Agriculture evolution [1] [2]

Agriculture technologies are rapidly evolving towards a new paradigm, Agriculture 4.0. Within this paradigm, the integration of digitization, automation, and artificial intelligence significantly improves crop production processes, including weed control and pest control. This change presents both challenges and opportunities, as the transition from manual and animal methods to automated and mechanized methods in developing countries helps bridge the digital divide [3]. Agriculture places a strong emphasis on environmental sustainability, and there are several techniques that help minimize environmental impact. Conservation agriculture is a method which includes crop diversification, permanent soil cover and minimal soil disturbance. This approach requires specialized equipment, such as tools for direct drilling of seeds into the ground at precise sowing depths and densities. Agricultural robotics can improve these ecological practices by allowing spot-on pest control and precise management of nutrients, pests, diseases and weeds through mechanical removal or targeted application of chemicals.

Agriculture 4.0 is currently well-structured, thanks also to economic policies aimed at its diffusion. Using various types of sensors, it is possible to obtain a wealth

of information and create maps for each field, accessible at any time through a cloud that stores all the data reported. This allows information on the type of soil, including naturally occurring chemical elements and moisture levels, to be acquired, allowing targeted and effective remedies, reducing waste and optimizing resources.

To complete this paradigm, it is necessary to introduce autonomous vehicles, generally referred to as drones or connected unmanned vehicles. These vehicles can independently carry out monitoring operations, perform plant-health treatments, perform various tasks and even assist during the harvest period; some prototypes can also directly perform it. To illustrate the crucial role of information management in modern agriculture, the Figure 1.2 illustrates the different steps and elements involved in digital farming: sensors monitor crops to generate data, which is acquired from a platform; Intervention options are provided and processed by specific software and AI, which allow the producer to decide how to act on crops. However,

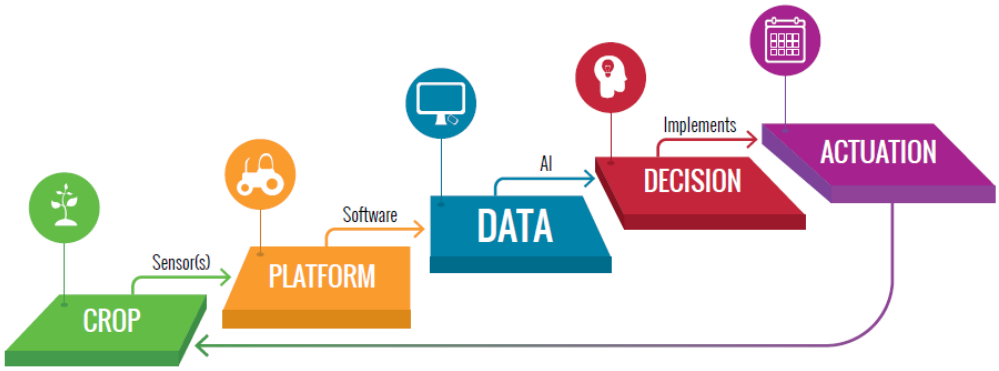

Figure 1.2: Information based cycle for advanced agriculture [3]

this technology is complex and it can be difficult for end users to have the necessary knowledge and familiarity with the whole process and its components. Agricultural robotics can integrate all these steps on a platform or specialise in specific aspects. Drones and other monitoring platforms provide real-time information, produce images, capture various agronomic parameters and alert farmers to crop trends, soil conditions and the appearance or risk of pests, diseases and weeds.

Technical improvements in new agricultural technologies should: optimise production efficiency, optimise quality, minimise environmental impact and minimise risks associated with production [3]. The need to introduce such vehicles is not only a "technological" requirement, but also a social one. If one analyses the data provided by INAIL [4], [5] n the trend of accidents at work in agriculture, it can be seen that more than 25,000 cases of agricultural accidents are reported each year,

with over 130 resulting in the worst possible outcome Figure 1.3.This is certainly a statistic which makes us reflect on current working conditions.

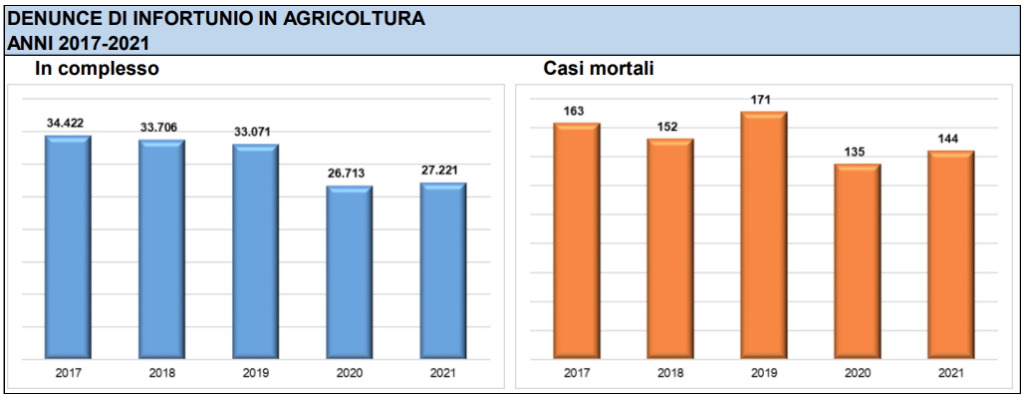

Figure 1.3: Injuries trend [4]

The analytical study of the trend of multiple fatal accidents, reported to INAIL, has confirmed that certain circumstances have occurred. The majority of reported fatal accidents in agriculture are on tractors, which can be attributed to the high number of hours of use for various applications.
The most frequent type of injury is crushing, the driver being crushed due to the overturning of the vehicle while performing an incorrect manoeuvre. In addition, accidents occur where the worker is hit by a vehicle after getting out of the vehicle which has not been stopped properly. The remaining parts of accidents are due to contact with moving parts during malfunctions, maintenance, lack of adequate protective equipment or operator negligence.

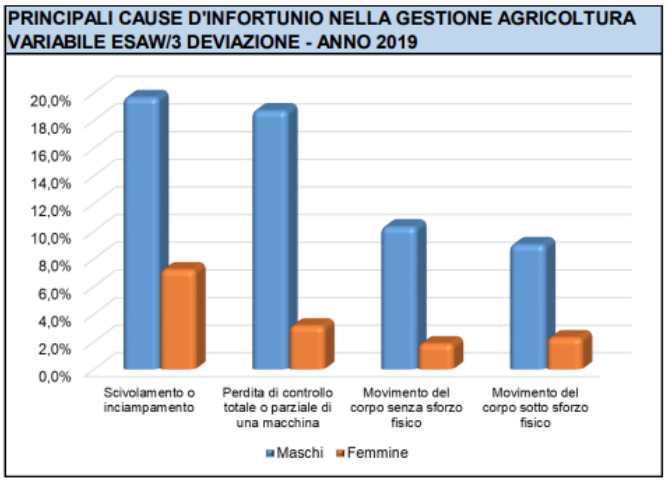

Figure 1.4: Causes of injures [4]

An important and representative data point concerns the average age of agri-

cultural workers and the distribution of occupational accidents and diseases by age. Figure 1.5 shows the age distribution of accidents, and it is clear that as people age more, so do the number of accidents. In agriculture, the tendency is to work until a relatively advanced age, which entails greater risks. As you age, your hearing, vision and reflexes tend to decrease, making it more difficult to drive and increasing the risk of injury. Considering all these factors, it is clear that reducing the tasks assigned to humans and increasing the activities performed by drones or autonomous rovers could positively affect the injury trend. Although lethal products are rarely used in agriculture at typical concentrations, there is a significant chemical or biological risk. Prolonged exposure to these substances (especially in the case of plant protection treatments where these substances are sprayed) can lead to the development of cancer and neurodegenerative diseases over the years.

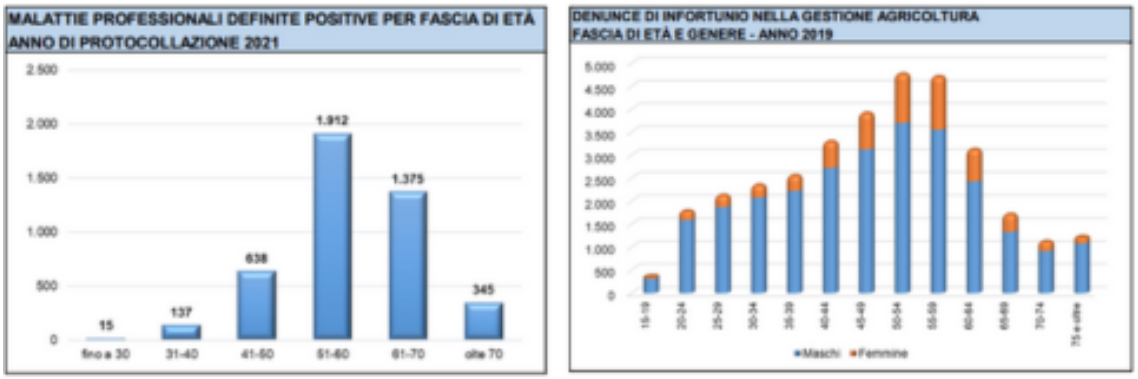

Figure 1.5: Distribution of injuries by age [4] [5]

This is the context for the company *Ecothea*, which designs, prototyping and develops innovative systems to introduce and spread sustainable mobility, especially in agriculture. The prototype developed included 'SMILLA', a four-wheeled rover designed for agricultural work. The aim of this thesis is to improve the model of the rover, in particular the steering system. Currently, the rover is able to drive using the so-called 'slip-steering', which means that it can steer by applying different torque to the wheels on both sides. This method of guidance has proved ineffective, especially under conditions of high friction; therefore, it was necessary to explore other methods that could be applied.

To achieve this, the behavior of the vehicle was simulated using a multi-body analysis software, *Adams View*, to safely test different types of steering systems. This allowed us to assess the boundary conditions that could affect steering efficiency, such as ground conditions, turning radii and operating speeds, ultimately determining the best solution.

2 State of Art

2.1 Steering mechanisms in agriculture

In the automotive field, the ability of a vehicle to steer is implemented in several ways. The systems adopted are also in use for other types of vehicles such as off-road vehicles and agriculture machinery. In the following paragraphs, the main steering method used in agriculture will be briefly described.

One of the most widely used methods both for passenger cars and agricultural machinery is the so-called coordinated steering. In this case the right and the left wheels on the same axle are connected through a mechanism so that the rotation of one wheel is coordinated with the other one [6].

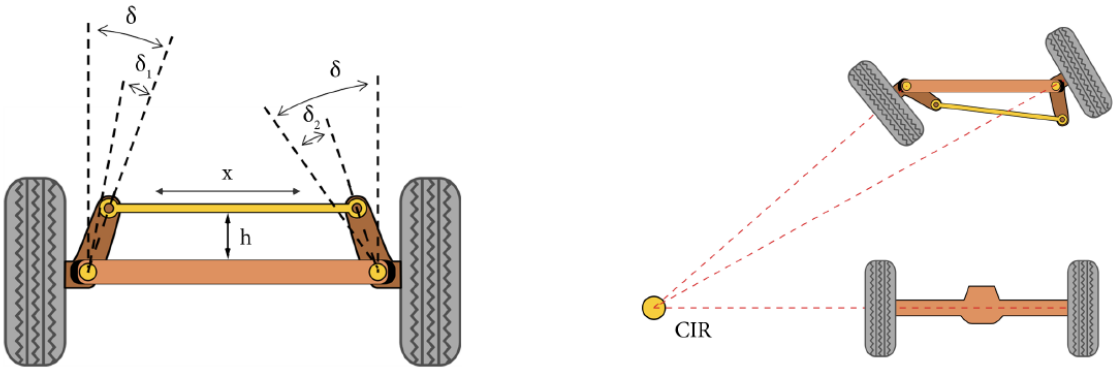

Figure 2.1: Ackerman steering mechanism

Depending on the parameters of the elements that make up the steering mechanism, different relationships can be achieved between the two wheels. A specific case of interest is ensuring the vehicle travels along an arc where all four wheels revolve around the same center-line. This condition can be realized by implementing the Ackerman steering mechanism, in which the length of its elements and the angle between them are defined by the track T of the vehicle and the wheelbase L (in Figure 2.1 α and β are the angle of internal and the esternal wheel in a turn) .

$$cot(\alpha) + cot(\beta) = \frac{T}{L} \tag{1}$$

By employing this relation, it is possible to obtain full rolling contact with the road, reducing to a minimum the sliding actions that will wear out the tires. The result is that the wheels will have different angles when performing a turn, ensuring that all wheels follow concentric circles [7].

A particular case of the previous system involves the implementation of 2 or

4 independent wheels, which are actuated individually by an electric motor or hydraulic system. In this case, the left and right wheels are not connected by a physical mechanism. However, with precise control, it is possible to achieve the Ackerman condition [6]. Moreover, since all the wheels are independent, it is possible to perform specialized maneuvers. Advances in electric motor and battery technology have enabled the replacement of traditional steering systems with independent steering modules for each of the four wheels, each powered by its own electric motor. Unlike conventional two- or four-wheel steering systems, where wheel orientations are mechanically linked, this new configuration allows each wheel to turn independently, offering greater flexibility and removing the limitations imposed by mechanical linkages. By properly coordinating the wheel orientations, the vehicle's maneuverability can become omnidirectional. This system is particularly advantageous in crowded environments, such as those found in agriculture, as it allows for zero-radius turning and lateral movement [8].

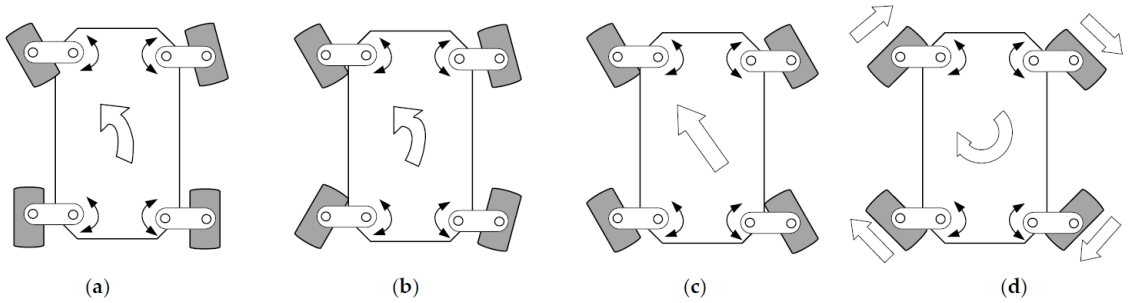

Figure 2.2: Possible steering modes: (**a**) Ackermann steering; (**b**) double Ackermann steering; (**c**) crab steering; (**d**) zero-radius turning. [9]

A further classification regarding the previous two models can be made based on the number of wheels involved in steering. In agriculture, as in the automotive field, the most commonly used system is front-wheel steering (FWS), where only the wheels on the front axle are engaged during a turn. This system is typically adopted in rigid-body tractors. [10]. Besides this system, there is also rear-wheel steering (RWS), adopted in forklifts and a few other applications, as harvesters [10], and all-wheel steering (AWS) or four-wheel steering (4WS), employed in high-performance sports cars to enhance dynamics at high speeds and telehandlers. Considering a four-wheel vehicle, it can be said that four-wheel steering is superior to two-wheel steering. It reduces the turning radius by around 21%, maintaining the same steering angle, and reduces the space required for a turn [11]. All-wheel steering also guarantees improved steering response and increased vehicle stability, especially at high speeds.

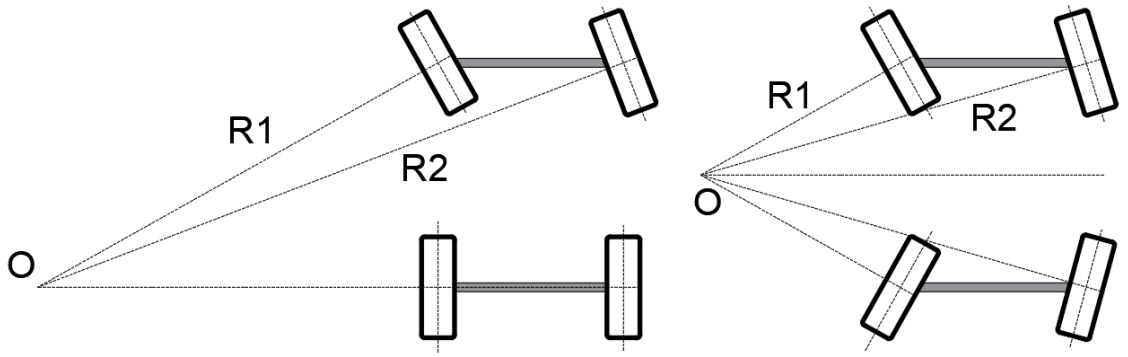

Figure 2.3: 2WS vs 4WS

An interesting aspect of all-wheel steering (AWS) is the phase relationship between the front and rear wheels. Specifically, at high speeds, the steering operates *in-phase*, meaning both the front and rear wheels turn in the same direction, helping to improve stability. Conversely, at low speeds, the steering operates *out-of-phase*, where the front and rear wheels turn in opposite directions, [12]. In agriculture, it is often necessary to perform maneuvers in tight spaces, and an AWS vehicle could be useful for optimizing operations. Four-wheel steering (4WS) involves two degrees of freedom, such as the steering angles of the front and rear axles. As a result, in four-wheel steering, the angles cannot be easily linked mechanically without introducing additional kinematic constraints to reduce the degrees of freedom to one. By employing an electronic control system or a steer-by-wire system, four-wheel steering can be implemented in an Ackermann manner without compromise [10].

A system that is mainly diffused in construction machinery but with few applications in agriculture field, is the articulated steering. In the pure articulated system the degree of freedom that allows steering is the rotation of the axle or the rotation of the front or rear part of the chassis, while the wheels are not allowed to rotate [6]; in agriculture, instead of the pure articulated system, a combined system, both articulated and Ackerman steering is used; some examples are *Dualsteer*® [13] and *Supersteer*® [14].

In Figure 2.5 the generic schematic of an articulated steering is shown, the actuation is performed at the point h, where the joint is placed. The steering action is obtained by changing the corresponding articulated angle gamma. A unique feature of articulated vehicles is their method of steering, which is accomplished by rotating one unit against the other in the yaw plane using an articulation joint. Therefore, articulated vehicles are often designed with similar-sized front and rear units such that they will have a negligible off-tracking error, which simplifies the path-tracking

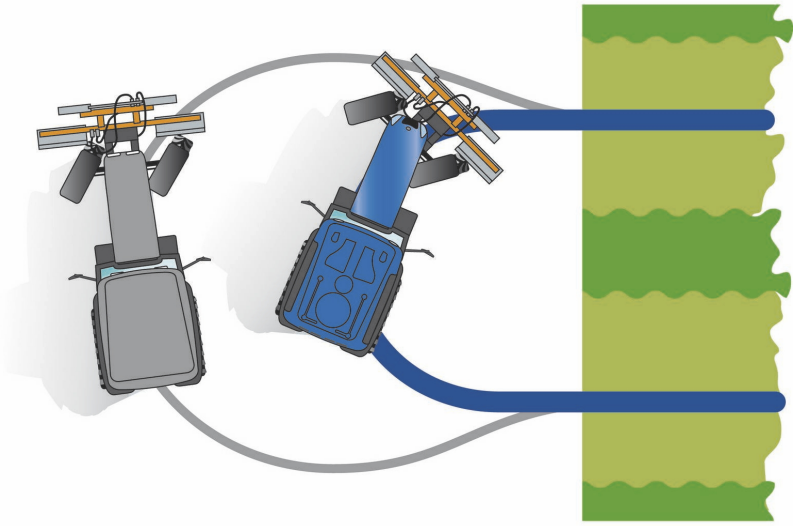

Figure 2.4: *Supersteer* system [14]

problem [15]. A limitation in vehicles that use articulated steering is the angle of articulation. If this angle becomes too large, instability may occur, but increasing it can result in very small turning radii. Therefore, a compromise between performance and safety/stability is necessary [16].

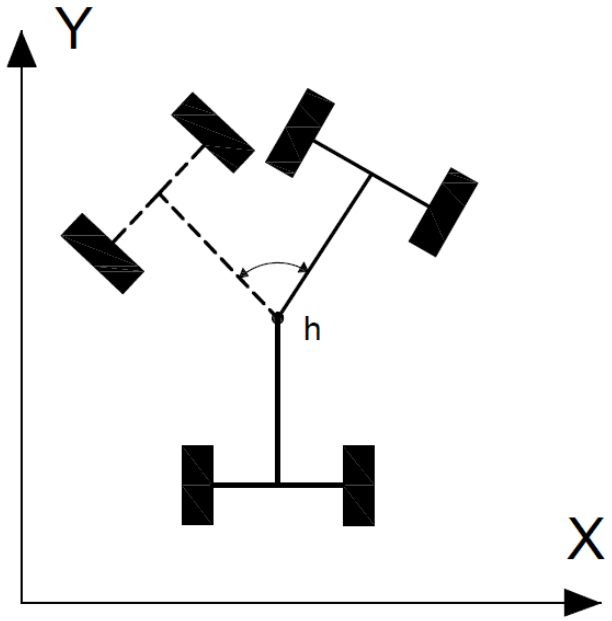

Figure 2.5: Articulated vehicle model [15]

A system rarely used in vehicle is the slip-steering or skid-steering. There is not an actual steering mechanism, in fact, the steering is obtained through the difference

of torque between the two sides of the vehicle, since here the controller evaluated a gradient of torque, this method is also called *torque vectoring*. This type of steering system is employed in those field where in-wheel motors or, in general, independent source of traction for each wheel are adopted, such as agriculture or construction. This allows to control independently the torque applied at each wheel, in a quick and precise way, making torque vectoring control strategies easy [17].

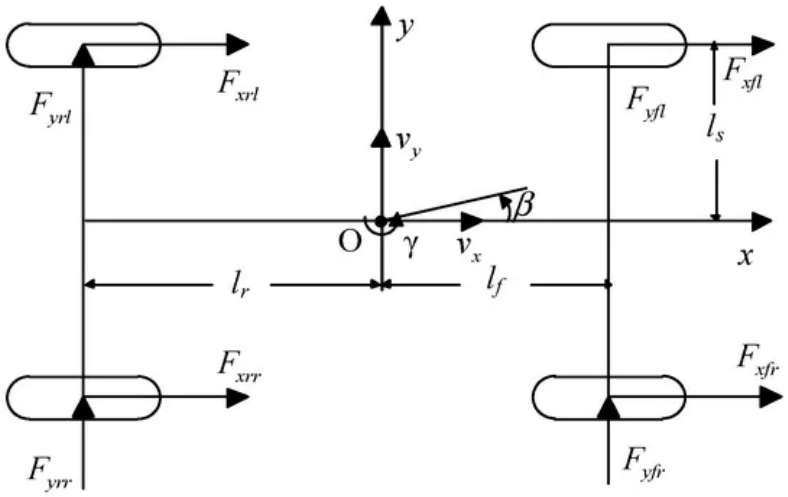

Figure 2.6: Slip steering [17]

In the automotive field it is used to improve cornering stability for high performance vehicles, but not as principle steering system. In fact, in certain cases, slip steering is also combined with active front steering, active rear steering and four wheel steering. Before the advent of electric motors, slip steering was either actuated through active and semi-active differentials or through individually controlled wheel brakes. Nevertheless, both these actuation are less effective than electric motors because of slower dynamics, lower efficiency and flexibility. [18] The appearance of four wheel independent drive (4WID) electric vehicles opens up the possibility of differential steering system (DSS) by coupled control of left and right in-wheel motors, which eliminates the restrictions of a traditional steering system completely. Slip steering was realized by giving a tire speed differential between the left and right tires. And the wheel torque difference between the left and right tires, which controlled the tire velocity difference, was defined as a function of the steering wheel angle.

2.2 Steering theory

2.2.1 Wheel steering

For the analysis of a generic vehicle's steering, a simplified approach using a kinematic model can be adopted. This method is particularly suitable for modelling agricultural vehicles, as their operating speeds are relatively low.

To effectively use the kinematic model, it is necessary to consider a vehicle moving at a low speed, ensuring that both the inner and outer wheels can steer without slipping. When these conditions are met, the wheels rotate purely, without lateral slippage [6].

Considering a front-wheel steering vehicle, the condition representing kinematic steering is known as the Ackerman condition. This condition describes the relationship between the steering angles of the front wheels, equation 2, ensuring that they trace different circumferences while sharing the same center of rotation.

$$cot(\alpha) + cot(\beta) = \frac{T}{L} \tag{2}$$

The relation in equation 2 it is obtain staring from the equation 3, these relations comes from the model in Figure 2.7.

$$tan(\delta_1) = \frac{l}{R1 - \frac{t}{2}} \quad , \quad tan(\delta_2) = \frac{l}{R1 + \frac{t}{2}} \tag{3}$$

By implementing the Ackerman mechanism, which imposes this condition on the wheels, the vehicle can achieve steering where each wheel follows its own path, allowing for smoother and more accurate turns, as it is shown in the Figure 2.7.

As shown in the equation 2, this relationship is a function of two parameters characteristic of each vehicle: the pitch (L) and the track (T) (distance between wheels centers). Therefore, a different relationship between the angles is valid for each vehicle.

To further simplify the discussion, the so-called bicycle model can be introduced, in which the vehicle is represented as an equivalent system with a single front wheel capable of steering and a rear wheel, as depicted in Figure 2.8. In this model, a third angle, δ, is defined, which results as the average of δ_1 and δ_2. This way, the fictitious wheel is positioned at the center of the track and travels along a third circumference, sharing the same center of rotation.

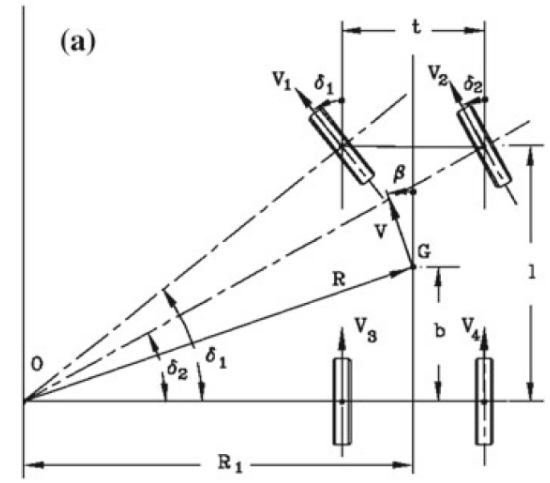

Figure 2.7: Generic front wheel steering vehicle

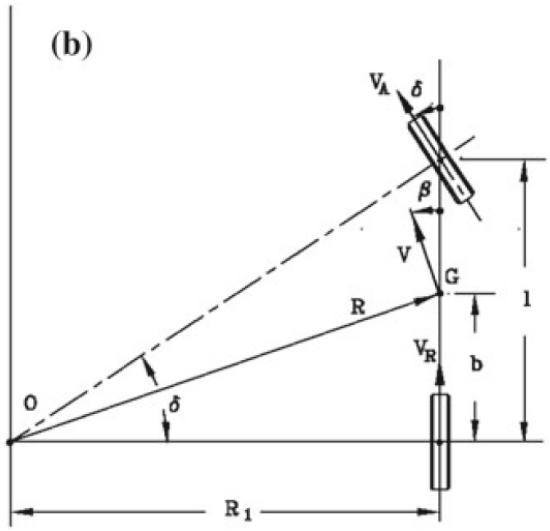

Figure 2.8: Bycicle model

This simplification can be adopted making a fundamental assumption, $t/2 << R_1$, the half track of the vehicle should be much lower than the turning radius. In this way $tan(\delta_{f1})$ and $tan(\delta_{f2})$ are function only of R_2 and l, and it is true:

$$tan(\delta_{f1}) = tan(\delta_{f2}) = tan(\delta_f) = \frac{l}{R_1} \tag{4}$$

The value of R can be obtained by some algebraically passage observing Figure 2.8 and considering equation 4, the final relation is reported in equation 5.

$$R = \sqrt{b^2 + R_1^2} = \sqrt{b^2 + l^2 \cdot (cotg(\delta_f))^2} \tag{5}$$

Imposing that the distance between the centre of mass of the vehicle and the rear axle is much smaller than the turning radius, $R_1 >> b$, it is possible to simplify the equation.

$$R \approx l \cdot cotg(\delta_d) \approx \frac{l}{\delta_f} \tag{6}$$

Finally, it is possible to linearize the cotangent since δ_f is a small angle, and turning the equation 6, it is obtained the equation 7.

$$\frac{1}{R \cdot \delta_f} = \frac{1}{l} \tag{7}$$

What is reported in equation 7, is the formulation of the curvature gain and it has an important physical meaning. The curvature gain is the the ration between the response of the vehicle, in terms of curvature, $\frac{1}{R}$, of the trajectory, and the input which causes it. It is also can be seen as a sort of transfer function for directional control.

Another transfer function that can be introduced in the kinematic model is the ratio $\frac{\beta}{\delta}$, defined as side slip angle gain. Where β is defined as in Figure 2.8, and it is the angle between the direction of the speed vector and the symmetry axis of the vehicle. The side slip angle, β, referred to the centre of mass can be obtained by some algebraic relation and the relation obtain is reported in equation.

$$\beta = arctang\left(\frac{b}{R_1}\right) \tag{8}$$

Substituting the equation 5, of R_1, it is obtained the final relation of the side slip angle gain, equation 10.

$$\beta = arctang\left(\frac{b}{R_1}\right) = arctang\left(\frac{b}{\sqrt{R^2 - b^2}}\right) \approx arctang\left(\frac{b}{R}\right) \approx \frac{b \cdot \delta_f}{l} \tag{9}$$

$$\frac{\beta}{\delta_f} \approx \frac{b}{l} \tag{10}$$

So far the dissertation is not considering forces and masses. To enter more into details with the steering theory it is possible to introduce the *steady state high speed cornering model*. In this model are introduced some assumption, the vehicle is travelling at constant speed, V, on a constant radius of curvature R on a level ground, it is not considered any aerodynamic forces and self aligning moment of the

tyre.

The initial model is the monotrack model, it is reported in Figure 2.9, where $R >> b$, with an additional assumption that the side slip angle β is small.

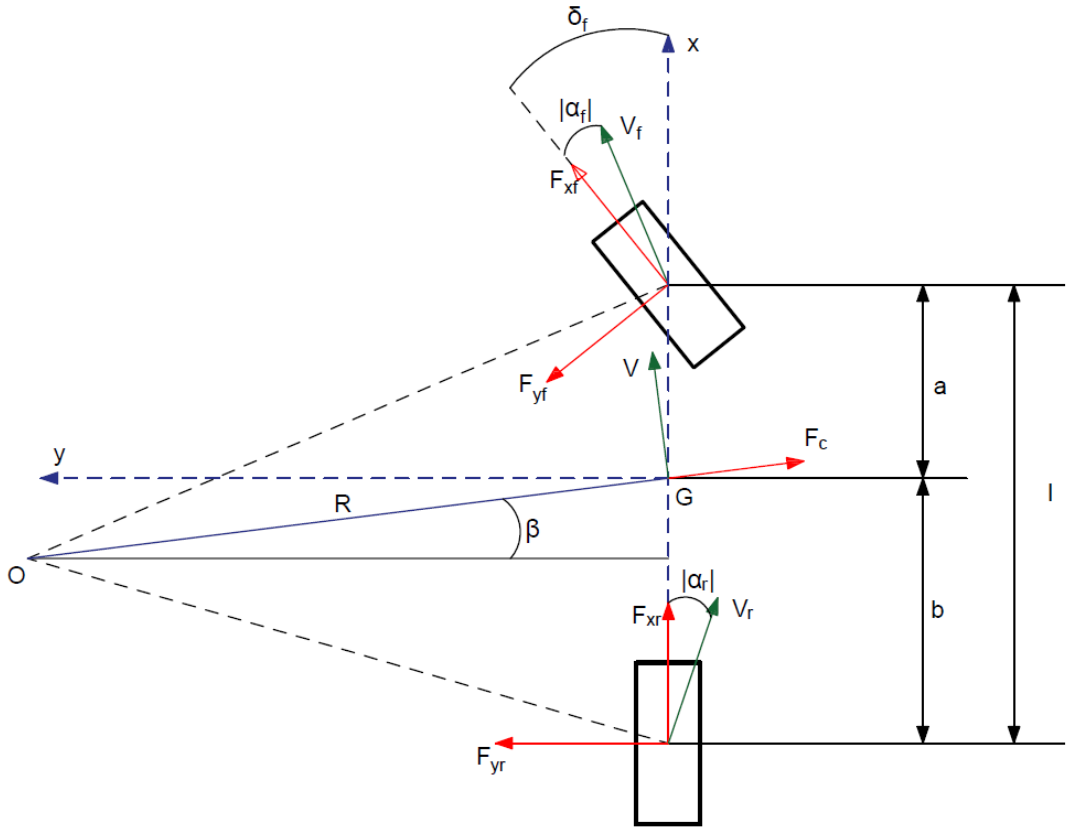

Figure 2.9: Bicycle model

Now it is possible to define the centrifugal force applied at the centre of the mass as reported in equation.

$$F_c = \frac{m \cdot V^2}{R} \tag{11}$$

For each tyre two forces can be applied one in x and y direction (F_{xf}, F_{xr}, F_{yf} and F_{yr}). One the forces are defined, it is possible to write two equation of equilibrium, one translation along y axis and one rotational about G point, (equation 12 and equation 13).

$$\frac{m \cdot V^2}{R} \cdot cos(\beta) = F_{xf} \cdot sin(\delta_f) + F_{yf} \cdot cos(\delta_f) + F_{yr} \tag{12}$$

$$F_{xf} \cdot sin(\delta_f) \cdot a + F_{yf} \cdot cos(\delta_f) \cdot a - Fyr \cdot b = 0 \tag{13}$$

The equilibrium equation can be simplified asopting the assumption that angle δ_f and b are small. The equilibrium along y axis and about G can be rewritten as reported in equations 14 and 15.

$$\frac{m \cdot V^2}{R} = F_{yf} + F_{yr} \tag{14}$$

$$F_{yf} \cdot a - F_{yr} \cdot b = 0 \tag{15}$$

To go further into details it is possible to assume the characteristic of the tyre to be linear, which means that they should work in the first part of the diagram in Figure 2.10. The characteristic of the tyre describe the behaviour of the tyre, in sense that the lateral force that the tyre exerts to the ground is function of the side slip angle. The absolute value of the side force F_y grows almost linearly at first as α increases, then, when the limit conditions of sliding are approached, in a slower way. Eventually it remains constant, or decreases slightly, when sliding conditions are reached.

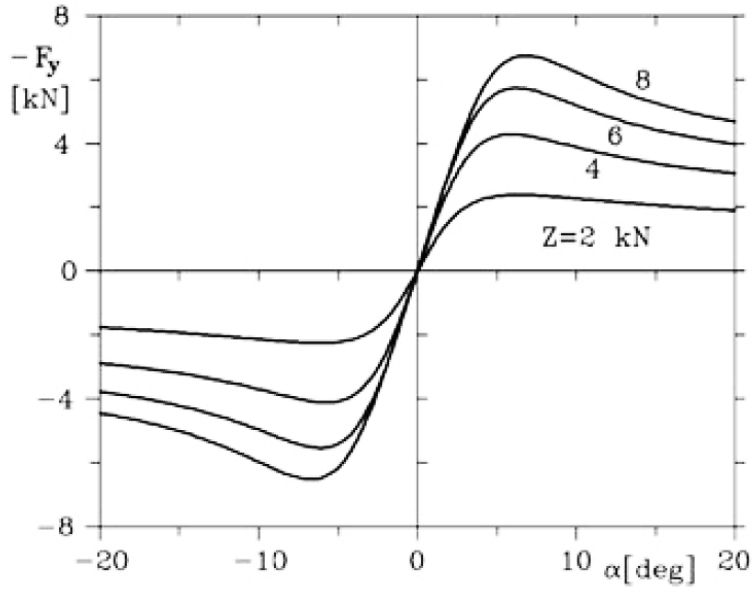

Figure 2.10: $F_y(\alpha) - characteristic$[19]

For small value of the side slip angle the cornering force increases linearly with α.

$$F_{yf} = -C_f \cdot \alpha_f \tag{16}$$

Where $C_\alpha = \frac{\partial F_x}{\partial \alpha}$ is always negative, since a positive angle causes a negative side force. The cornering stiffness or cornering power C is usually expressed as a positive number so it is arbitrarily defined and written as the derivative changed in sign. The lateral forces exerted by the front and the rear tyre can be evaluated as reported in equation 17 and equation 18. Where α_f and α_r are the side slip angle of the tyre while C_f and C_r are the cornering stiffness of front and rear wheels, that correspond to the slope of the graph in Figure 2.10.

$$F_{yf} = -C_f \cdot \alpha_f \tag{17}$$

$$F_{yr} = -C_r \cdot \alpha_r \tag{18}$$

Reversing the equations 14 and 15, it is possible to obtain the relation of F_{ys} and F_{yr}. These relations can be substituted in equations 17 and 18, finally the formulation of the side slip angles.

$$\alpha_f = -\left(\frac{m \cdot V^2}{R}\right)\left(\frac{b}{l \cdot C_f}\right) \tag{19}$$

$$\alpha_r = -\left(\frac{m \cdot V^2}{R}\right)\left(\frac{a}{l \cdot C_r}\right) \tag{20}$$

Equation 19 and equation 20 are useful to determine the curvature gain, side slip angle gain and acceleration gain, the relations are reported in equations 21, 22 and 23, avoiding all the passages needed to reach those relations.

$$\frac{1}{R \cdot \delta_f} = \frac{1}{l} \cdot \frac{1}{1 + K_{US} \cdot \frac{V^2}{g \cdot l}} \tag{21}$$

$$\frac{V^2}{R \cdot \delta_f} = \frac{V^2}{l} \cdot \frac{1}{1 + K_{US} \cdot \frac{V^2}{g \cdot l}} \tag{22}$$

$$\frac{\beta}{\delta_f} = \frac{b}{l} \cdot \left(1 - \frac{m \cdot a \cdot V^2}{b \cdot l \cdot C_r}\right) \cdot \frac{1}{1 + K_{US} \cdot \frac{V^2}{g \cdot l}} \tag{23}$$

In these equations appear the term, K_{US}, which is the under-steering coefficient. It is useful to understand the behaviour of the vehicle.

$$K_{US} = \frac{m \cdot g}{l} \cdot \left(\frac{b}{C_f} - \frac{a}{C_r}\right) \tag{24}$$

Observing equation 21 and varying the sign of the under-steering coefficient, it

is possible to investigate the behaviour of the vehicle. In Figure 2.11 is reported a graph with the trend of the curvature gain as a function of the vehicle speed, for positive and negative under-steering coefficient.

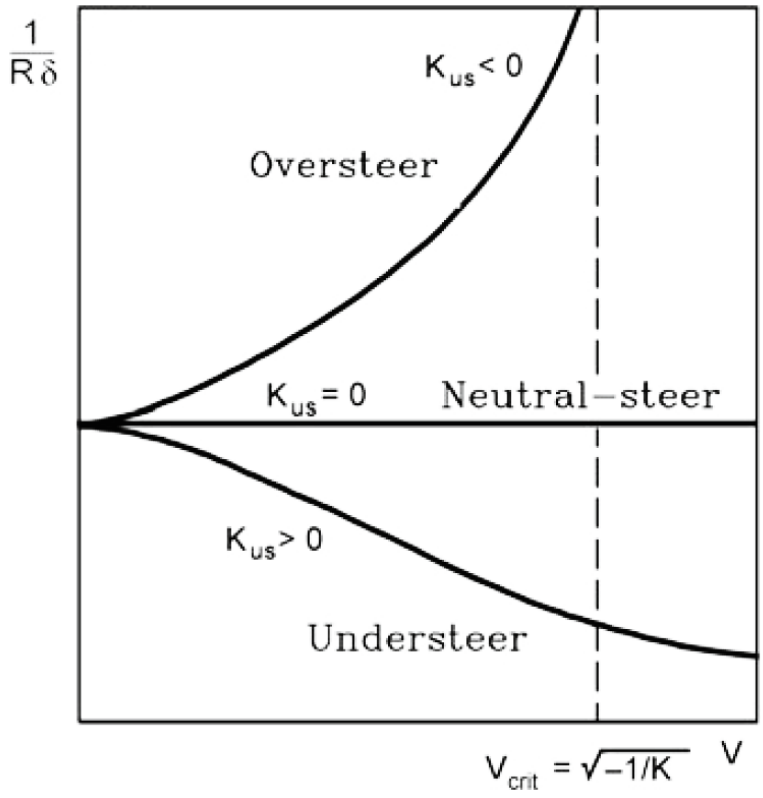

Figure 2.11: Curvature gain trend [6]

If $K_{US} > 0$ it is possible to define the characteristic speed, V_{car}, as reported in equation 26. The value of the curvature gain decrease with increasing speed, which means that the vehicle is less responsive. The vehicle in this condition is called under-steering.

$$V_{car} = \sqrt{\frac{g \cdot l}{K_{US}}} \tag{25}$$

The value of the curvature gain at the characteristic speed is:

$$\frac{1}{R \cdot \delta_f}(V = V_{car}) = \frac{1}{2 \cdot l} \tag{26}$$

This means that the curvature gain above the characteristic speed is constant and it is limited to the value of $1/(2 \cdot l)$, as it is also possible to see in Figure.

If $K_{US} < 0$ it is possible to introduce the critical speed, V_{crit}, as reported in

equation 27. The vehicle curvature gain increases with increasing speed, till the critical speed, where the curvature gain tends to infinite, meaning that the vehicle is unstable. A vehicle behaving in this way is said to be over-steering.

$$V_{crit} = \sqrt{-\frac{g \cdot l}{K_{US}}} \tag{27}$$

As last case, K_{US}, the curvature gain is constant and equal to the value characterizing the kinematic steering, which means that the response of the vehicle to a steering input is, at any speed, equal to that in kinematic conditions. A vehicle in this condition is called neutral-steering.

Besides the effect of the under-steering coefficient, there are other additional effects that can be taken into account. A vehicle's directional behaviour is strongly influenced by the presence of longitudinal forces between tires and road. Considering the linearized model of the tires, this effect can be easily accounted for, by using the elliptical approximation:

$$\left(\frac{F_y}{F_{yo}}\right)^2 + \left(\frac{F_x}{F_{xo}}\right)^2 = 1 \tag{28}$$

Where F_{xo} and F_{yo} are respectively the maximum longitudinal and the maximum lateral force that the tires are able to transfer to the ground. In particular the lateral force is limited by the maximum cornering stiffness C_o, while the longitudinal force is constrained by the friction coefficient ($F_{yo} = -C_o \cdot \alpha$ and $F_{xo} = \mu_{zp} \cdot F_{zf}$).

The variation in the cornering stiffness is given by the equation 29.

$$C_f = C_{of} \cdot \sqrt{1 - \left(\frac{F_{xf}}{\mu_{xp} \cdot F_{zf}}\right)^2} \tag{29}$$

When a longitudinal force is applied, a reduction in the cornering stiffness is obtained. Observing equation 21, it is possible to say that any reduction in front cornering stiffness, meaning that a front longitudinal force is applied, a reduction in the curvature gain is obtained, the vehicle is more understeer or less oversteer. The opposite is true if it is applied to the rear wheels.

During a turn an inevitable load transfer happens between the internal and external side of the vehicle. It is made of two contribution, one coming from the roll moment, generated by the side force applied at the body centre of gravity and the second comes from the side force applied at the body centre of gravity, which generate a front and a rear lateral force.

In road vehicle, the roll stiffness is given by two contribution, one coming from the

stiffness of the sprig and the other coming from the anti-roll bar. Since in agriculture vehicle the anti-roll bar is generally not implemented, the total roll stiffness is called χ and it is considered made of the front and the rear contribution (χ_f and χ_r). During a turn the vehicle tends to rotate around the roll centre due to a roll moment M_x, producing a rotation of the vehicle Φ.The roll moment about the roll axis since the roll centre is not aligned with the centre of gravity is:

$$M_x = F_y \cdot h \tag{30}$$

the roll angle obtained is:

$$\Phi = \frac{M_x}{\chi} = \frac{F_y \cdot h}{\chi} = \frac{F_y \cdot h}{\chi_f + \chi_r} \tag{31}$$

From the equilibrium equation around the centre of gravity, considering the forces reported in Figure, is obtain the following relation:

$$F_y \cdot h = \Delta F_z \cdot t \tag{32}$$

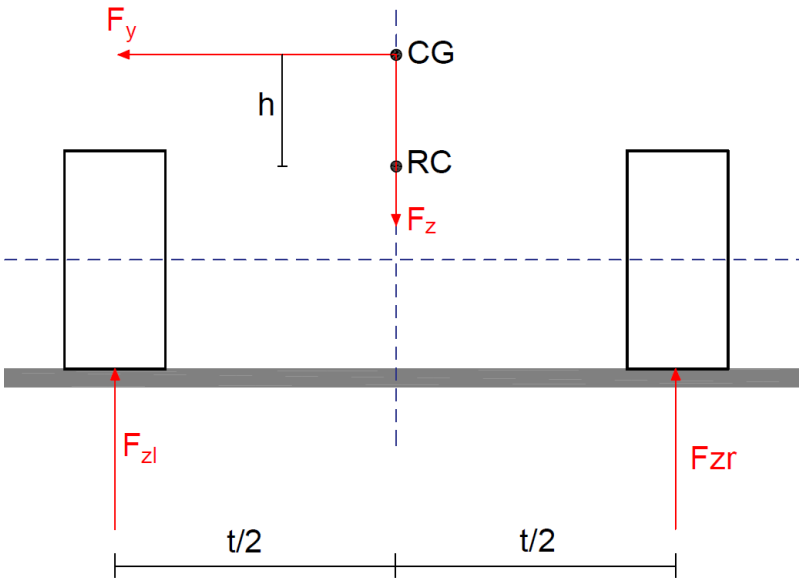

Figure 2.12: Rotation equilibrium

, considering equation 30 and equation 32, it true that:

$$M_x = \Delta F_z \cdot t \tag{33}$$

Finally the front and the rear component of load transfer are obtained.

$$\begin{aligned} \Delta F_{zf} &= \frac{M_{xf}}{t_f} = \left(\frac{F_y \cdot h}{t_f}\right) \cdot \frac{\chi_f}{\chi_f + \chi_r} \\ \Delta F_{zr} &= \frac{M_{xr}}{t_r} = \left(\frac{F_y \cdot h}{t_r}\right) \cdot \frac{\chi_r}{\chi_f + \chi_r} \end{aligned} \tag{34}$$

The second contribution is evaluated starting from a lateral equilibrium reported in Figure 2.13.

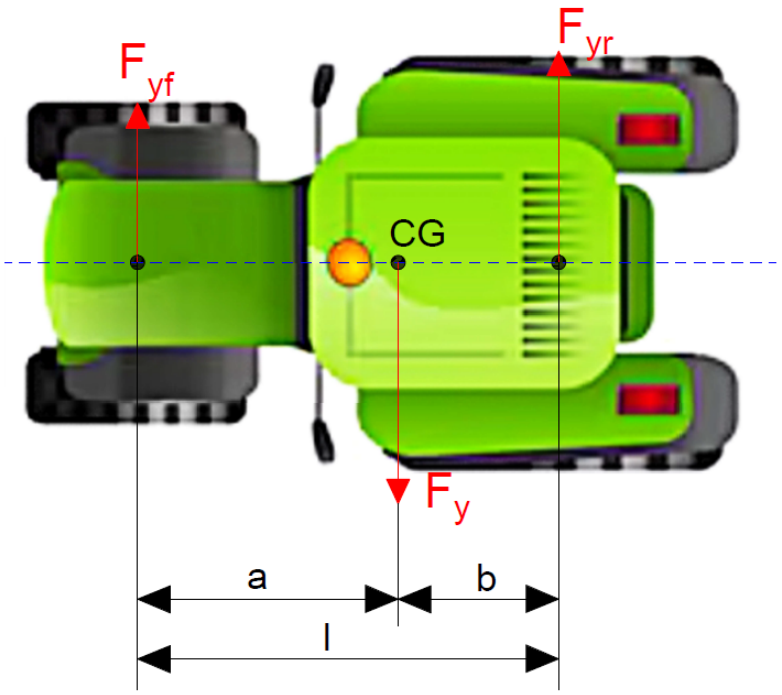

Figure 2.13: Lateral equilibrium

$$\begin{aligned} F_{yf} &= F_y \cdot \frac{b}{l} \\ F_{yr} &= F_y \cdot \frac{a}{l} \end{aligned} \tag{35}$$

On each axle the load transfer is evaluated as the rotation equilibrium with respect to the couple of vertical forces.

$$\begin{aligned} \Delta F_{zfRC} &= F_{yf} \cdot \frac{h_{RCf}}{t_f} = F_y \cdot \frac{b}{l} \cdot \frac{h_{RCf}}{t_f} \\ \Delta F_{zrRC} &= F_{yr} \cdot \frac{h_{RCr}}{t_r} = F_y \cdot \frac{a}{l} \cdot \frac{h_{RCr}}{t_r} \end{aligned} \tag{36}$$

The total lateral load transfer is made of the two contribution is:

$$\begin{aligned} \Delta F_{zf} &= \frac{F_y}{t_f} \cdot \left(h \cdot \frac{\chi_f}{\chi_f + \chi_r} + \frac{b}{l} \cdot h_{RCf} \right) \\ \Delta F_{zr} &= \frac{F_y}{t_r} \cdot \left(h \cdot \frac{\chi_f}{\chi_f + \chi_r} + \frac{a}{l} \cdot h_{RCr} \right) \end{aligned} \tag{37}$$

As stated at the beginning of this paragraph, the lateral load transfer has an influence on the behaviour of the vehicle during a turn. A variation in the vertical force will end in a variation in the cornering stiffness. The characteristic of this phenomenon is depicted in Figure 2.14.

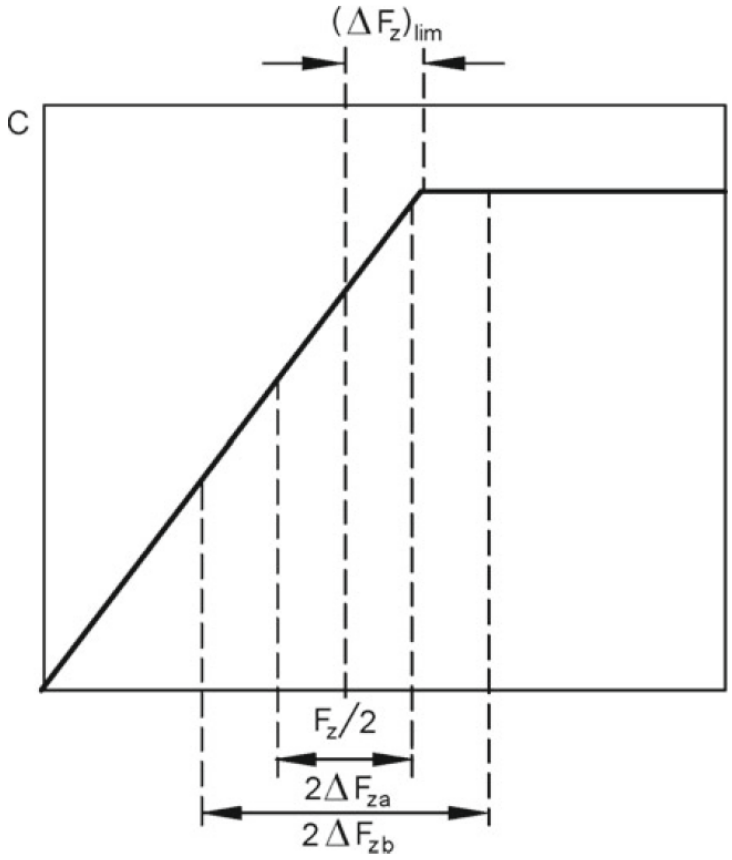

Figure 2.14: Effect of load transfer on the cornering stiffness [19]

Now it is important to make a fundamental consideration. In Figure it can be noticed that after a certain vertical load, F_{zo}, the cornering stiffness is saturated to a maximum constant value, C_o. This means that an excessive load transfer will give rise to saturation in the contact force.

In conclusion the side slip stiffness on an axle can be written as:

$$C_i = \frac{1}{2} \cdot \left(C_{oi} + \Delta F_z \cdot \frac{\partial C_i}{\partial F_z} \right) \sqrt{1 - \left(\frac{F_x}{\mu_{xp} \cdot (F_z + \Delta F_z)} \right)^2} + \frac{1}{2} \cdot \left(C_{oi} - \Delta F_z \cdot \frac{\partial C_i}{\partial F_z} \right) \sqrt{1 - \left(\frac{F_x}{\mu_{xp} \cdot (F_z - \Delta F_z)} \right)^2} \tag{38}$$

2.2.2 Torque differential steering

Trajectory of a vehicle in pneumatic tires may be controlled by applying differential longitudinal forces to the tires on the right and left side instead of steering some of the wheels. If the two wheels of the *i-th* axle, considering t is the track, produce a longitudinal force:

$$F_{xiLR} = \frac{F_{xi}}{2} \pm \Delta F_{xi} \tag{39}$$

Once the force is determined, it is possible to evaluate the control torque as:

$$M_{zc} = \sum_{\forall i} \Delta F_{xi} \cdot t_i \tag{40}$$

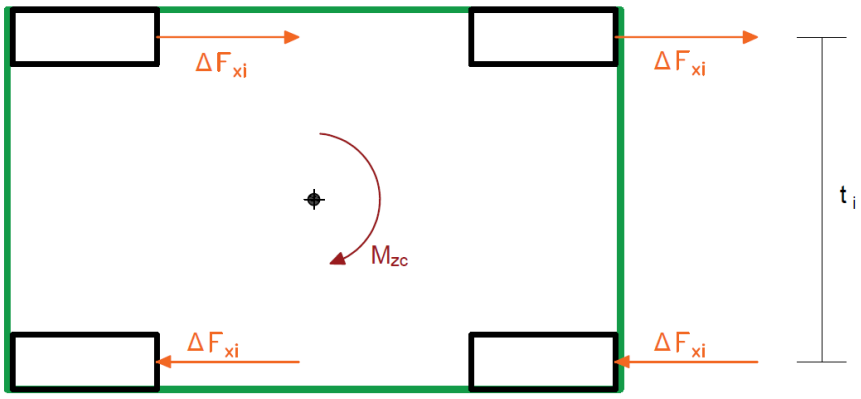

Figure 2.15: Yawing moment

If the longitudinal slip σ of the tires is small enough, the longitudinal force is proportional to the longitudinal slip. It vanished when $\sigma = 0$, free rolling condition is present, to increase with almost linear law for values of σ about -0.25 to about 0.25 [19]. The linear law is reported in the following equation:

$$F_x = C_\sigma \cdot \sigma \tag{41}$$

where the constant C_σ, can be defined as slip stiffness or longitudinal stiffness and can be considered as the slope of the characteristic: $C_\sigma = \frac{\partial F_x}{\partial \sigma}$. The characteristic is shown in Figure 2.16. In the first part of the curve the slip stiffness is roughly proportional to the load. As notices in Figure 2.16, the characteristic $F_x(\sigma)$ is function of the vertical load. This means that the ability to steer is connected to the weight loaded on the vehicle.

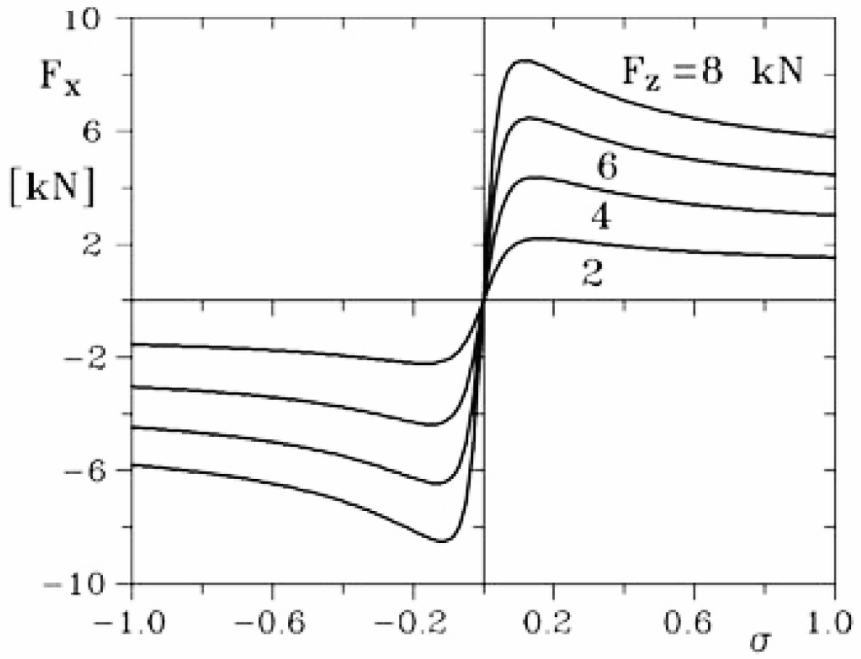

Figure 2.16: $F_x(\sigma)$*characteristic* [19]

The yawing moment can thus be expressed as:

$$M_{zc} = N_\sigma \cdot \Delta\sigma \tag{42}$$

Where:

$$N_\sigma = \sum_{\forall i} C_{\sigma i} \cdot t_i \tag{43}$$

The value of the control yawing moment is inserted in the equation of the vehicle model. The system in equation is obtained through a set of passages considering forces on the wheels, aerodynamic forces and accelerations, for sake of simplicity, it is taken already at the final form, as reported in book *"Automotive chassis"* [6].

$$\begin{cases} mV(\dot{\beta} + r) + m\dot{V}\beta = Y_\beta \cdot \beta + Y_r \cdot r + Y_\delta \cdot \delta + F_{ye} \\ J_z \cdot \dot{r} = N_\beta \cdot \beta + N_r \cdot r + N_\delta \cdot \delta + M_{ze} + M_{zc} \end{cases} \tag{44}$$

In automotive field the yawing moment has only a control purpose in sense that it helps the lateral control and stability. Analysing equation 44, it is possible to understand that removing the contribution of the steering angle δ, the only action that will give a steering action is the yawing moment.

3 Materials and methods

In this section will be briefly described the software used for the simulation and for data processing; following by the detail of the models construction.

3.1 Software

Thanks to the increase in computational capacity, simulations are becoming increasingly useful, as they allow for the analysis of more complex systems and have now become an integral part of vehicle design. The idea behind multi-body simulation is to build models composed of rigid or deformable bodies, connected by mass less elements [20]. Each body can be assigned properties of mass and inertia that are independent of the element's shape, but representing the properties of the physical model.

Since agricultural vehicles, and vehicles in general, operate in various environments and with different machinery throughout their life-cycle, their dynamic behavior is influenced accordingly. Multi-body simulations allow for testing vehicle models in all possible environmental conditions that a vehicle might encounter [21]. By conducting simulations that closely mimic reality within a safe environment, once a comprehensive understanding of a vehicle's dynamic properties and acceptable behavior is achieved, a real prototype can then be developed and tested in the real world [20][21].To accurately analyze different types of terrain, the wheel-terrain interaction must be properly defined. Multi-body models allow for the implementation of various relationships that account for wheel and terrain deformation, contact pressure, and the area involved in the contact. The wheel-terrain contact is crucial as it determines traction performance and, consequently, the vehicle's functionality [21].

The models that will be presented in the following subsection are built completely in Adams view. *Adams view* is a multi-body software which allows to build a simplify model of a vehicle connecting simple shape element through rotational, of translation or more complex joint.

3.2 Models

In this section are presented three models with three different steering system: independent four wheel steering, skid/slip steering and four wheel steering adopting the Ackerman mechanism. These models are based on the same structure as is shown in Figure 3.1. The following models are built completely on *Adams View* [22].

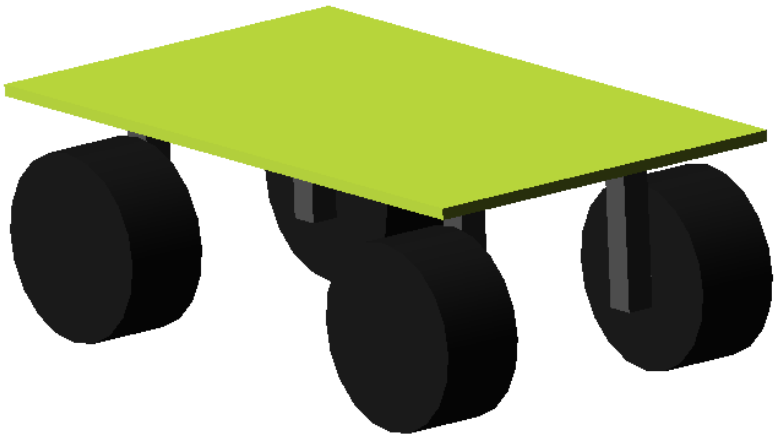

Figure 3.1: Multi-body model

The base structure is composed of three main component; the first element is a square light-green element represents the chassis, the dimensions are reported in Table 1.

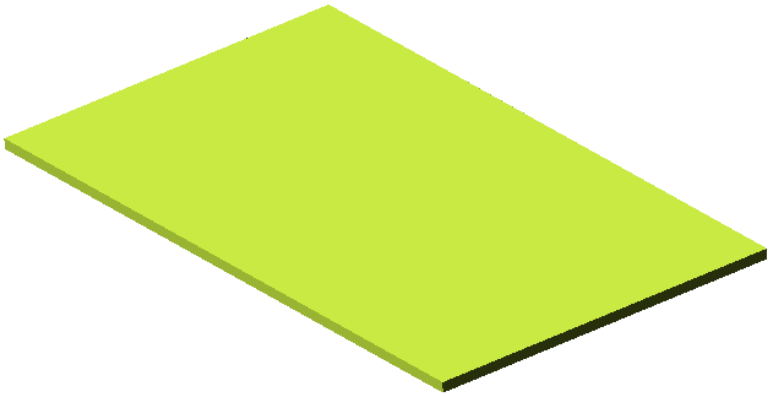

Figure 3.2: Chassis

Length $[mm]$	**Width** $[mm]$	**Depth** $[mm]$
1700	1100	20

Table 1: Dimension of the chassis

Thanks to the multi-body analysis it is possible to use a simple rectangular based and change its internal parameters are reported in Table 2.

Mass $[kg]$	200
Ixx $[kg \cdot mm^2]$	$1.3 \cdot 10^7$
Iyy $[kg \cdot mm^2]$	$1.2 \cdot 10^7$
Izz $[kg \cdot mm^2]$	$8.0 \cdot 10^5$

Table 2: Inertia and mass of the chassis

The second element are actually the four wheels. Each wheel is built as a cylinder, the dimensions are reported in Table 3.

Radius $[mm]$	**Width** $[mm]$
330	300

Table 3: Dimension of a wheel

Since a wheel of this type is not a model representing a real wheel. To implement the real behaviour of the wheels adopted in the rover, the parameters, regarding inertia and mass, reported in Table 4 are assigned to each wheels.

Mass $[kg]$	4
Ixx $[kg \cdot mm^2]$	$9.94 \cdot 10^4$
Iyy $[kg \cdot mm^2]$	$5.72 \cdot 10^4$
Izz $[kg \cdot mm^2]$	$5.72 \cdot 10^4$

Table 4: Inertia and mass of the wheels

The last elements are the support, gray boxes in Figure. To simplify the simulation these boxes are considered without inertia, the only contribution that they give is of the mass of 4 kg. The role of the support is to allow the steering action of the wheels through hinges, the degree of freedom can be locked in case of slip steering or left free in case of rotation of the wheels.

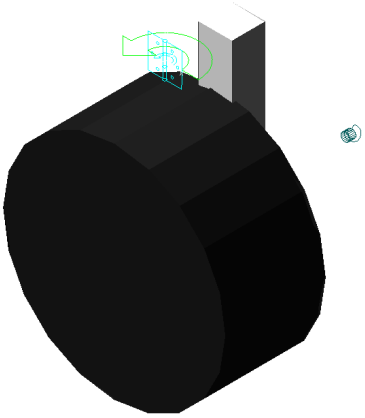

Figure 3.3: Wheel and support

As sad before four hinges are placed between each support and the chassis, while between each support and each wheel is present a *bushing joint*. This element enables the implementation of a real joint, that into consideration that a real connection is not infinitely stiff. By setting properly the parameters of the bushing joint is possible to account for the deformation of the wheel. The parameter chosen are reported in Table 5 how has been proposed in the thesis [23]. The bushing joints, as defined, allow allow the rotation of the wheel to provide the propulsion power.

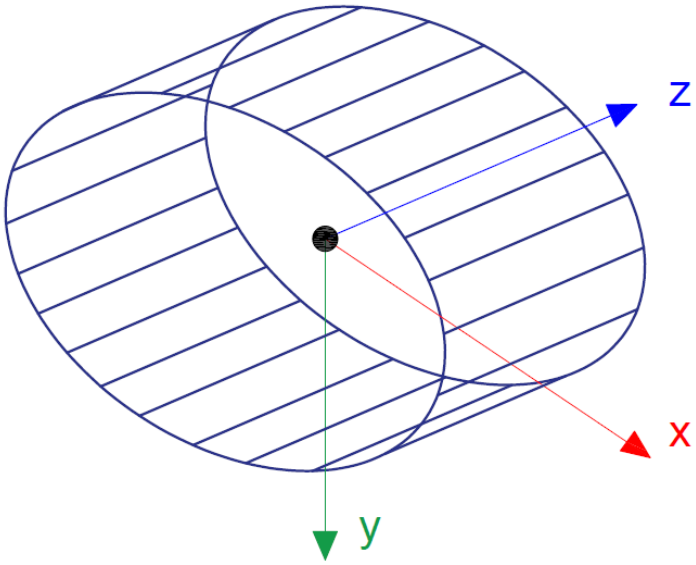

Figure 3.4: Bushing joint

Of paramount importance is the choice of the law governing the contact between

		X	Y	Z
Traslational	**Stiffness** [N/mm]	500	500	$1.0 \cdot 10^6$
	Damping [Ns/mm]	4	4	1000
Rotational	**Stiffness** [Nmm/deg]	$1.0 \cdot 10^8$	$1.0 \cdot 10^8$	0
	Damping [Nmms/deg]	$1.0 \cdot 10^8$	$1.0 \cdot 10^8$	0

Table 5: Parameters of the bushing joints [23]

each tire and the ground. They exist several model that describe the tyre-soil interaction. Since these models are derived from complex theories and are defined by intricate empirical equations that require precise and optimal definitions of a set of constants and parameters—dependent on several vehicle variables, such as penetration depth and slip velocity, the decision was to use the command provided by *Adams view*. This command, called contact, it is described by the equation 45 and it is characterized by the parameters reported in Table 6, as suggest a previous research [23].

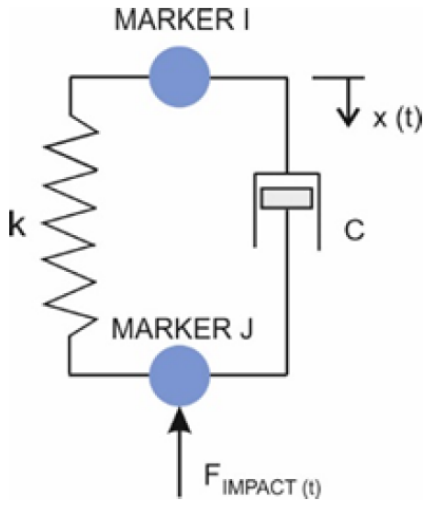

Figure 3.5: Functioning of contact function [24]

$$F = \begin{Bmatrix} Max(0, k(x_1 - x)^S - STEP(x, x_1 - d, c_{max}, x_1, 0) \cdot \dot{x} & , x < x_1 \\ 0 & , x > x_1 \end{Bmatrix} \quad (45)$$

Where x_1 is the distance between *MARKER I* and *MARKER J* at the beginning, C_{max} is the damping at the penetration d and g is the actual penetration. Note that if $g < d$ the value of the damping is a cubic step function of g else, if $g > d$ the damping coefficient is maximum [24].

The model provided by *Adams view* can be considered as a simplify model, besides some of the constant parameters are actually varying during the simulation, increasing the level of approximation of the reality. Otherwise to simplify the computational cost and the model complexity it is not important to define in a precise way the tyre-soil contact, as the main objective of this thesis is focused on the analysis of steering systems.

Normal Force : Impact	
Stiffness k	300
Force Exponent S	2.0
Damping C_{max}	1.0
Penetration Dept d	$1.0 \cdot 10^{-2}$
Friction Force: Coulomb	
Static Coefficient	0.7
Dynamic Coefficient	0.6

Table 6: Contact parameters

Once the model is built, it is possible to continue with the design of controllers for each type of steering. In addition, the concept of dummy body and longitudinal controller will be introduced in the following two sections.

3.2.1 Dummy body

In *Adams view* it is needed an element able to give the reference position. This element is called dummy-body, it is a small box with mass and inertia are negligible, so that there is no influences. The dummy body is connected to the trajectory through a point-to-curve constraint, while the connection between the vehicle and the dummy body is performed via controller, that will be exploited in the following section. To better explain how the dummy body is bound with the trajectory, you can observe the Figure 3.6. It is possible to notice that to allow the constraint has

been created a "marker" placed in the center of the box mass; then the origin of this marker, DM_{POS}, will be bound to the curve.

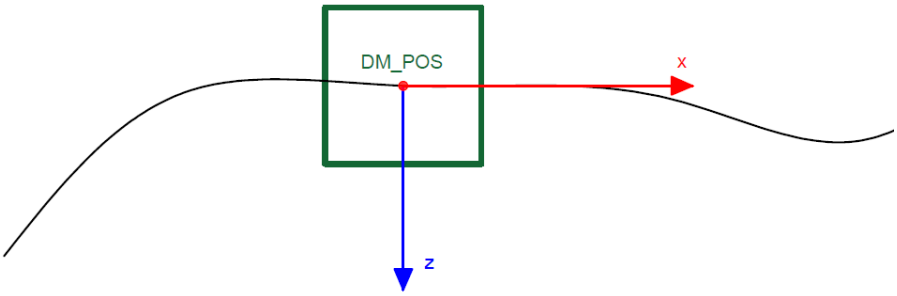

Figure 3.6: Dummy body

3.2.2 Longitudinal control

As the simulation has started, the dummy body is travelling at constant speed. To allow the vehicle to move at a constant speed, and in this way follow the dummy body, a controller is implemented. The action applied by the controller is proportional to the distance error and to its derivative, the difference in speed. The distance error is expressed as show in equation 46, where x_{DB} and x_{CH} are respectively the coordinate of the dummy body and the centre of the front axle measured along the x axis of a reference system placed on the centre of the front axle. In practise Δx measure the value of the coordinate x of the dummy body.

$$\Delta x = x_{DB} - x_{CH} \tag{46}$$

Regarding the speed error the consideration are mainly the same done for the distance error. In fact, in equation 47 V_{DB} and V_{CH} are respectively the speed of the dummy body and of the centre of the front axle.

$$\Delta V = V_{DB} - V_{CH} \tag{47}$$

The final action is a torque. In order to reduce to a minimum the distance error and the speed error, the controller should be perfectly tuned by chosen the adequate value of the constant K_p and K_d present in equation 48. Since the tuning constant are different for each model, considering that a steering system can induce an bigger decrease in the speed during a turn with respect to another, the parameters that

has been chosen are reported in Section 4.1.

$$T_{long} = K_p \cdot \Delta x + K_d \cdot \Delta V \tag{48}$$

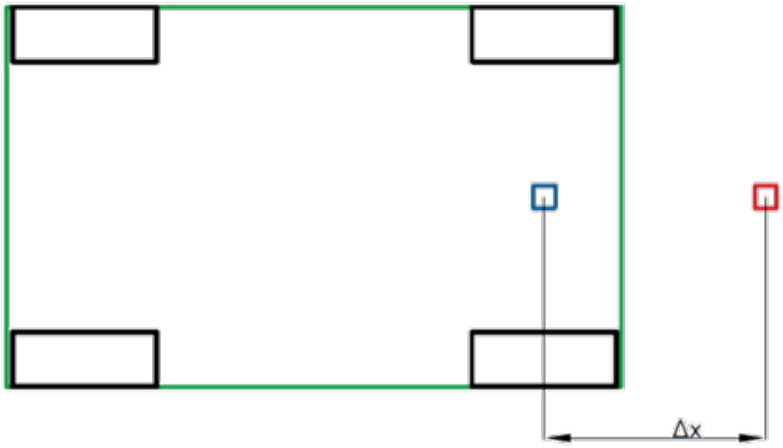

Figure 3.7: Longitudinal error

3.2.3 Slip steering

The model is a direct derivation of the model described in section 3.2. Since there is not an action of the wheels in term of rotation, the hinged are locked and all the wheel are kept in the same direction for the entire simulation.

Steering is achieved through a torque differential between the right and left wheels. In the literature, various methods are available for controlling lateral position using the torque vectoring paradigm. These approaches are generally quite complex and, therefore, difficult to implement in Adams. To simplify the discussion in this thesis, a proportional controller was chosen. The torque contribution that enables steering is determined by first evaluating the angular error ($\Delta\alpha$) between the vehicle's current direction and the desired direction, as shown in the equation 49. Where Δz and Δx are measured from the center of the vehicle's front axle, as illustrated in the Figure 3.8.

$$\Delta\alpha = tan^{-1}\left(\frac{\Delta z}{\Delta x}\right) \tag{49}$$

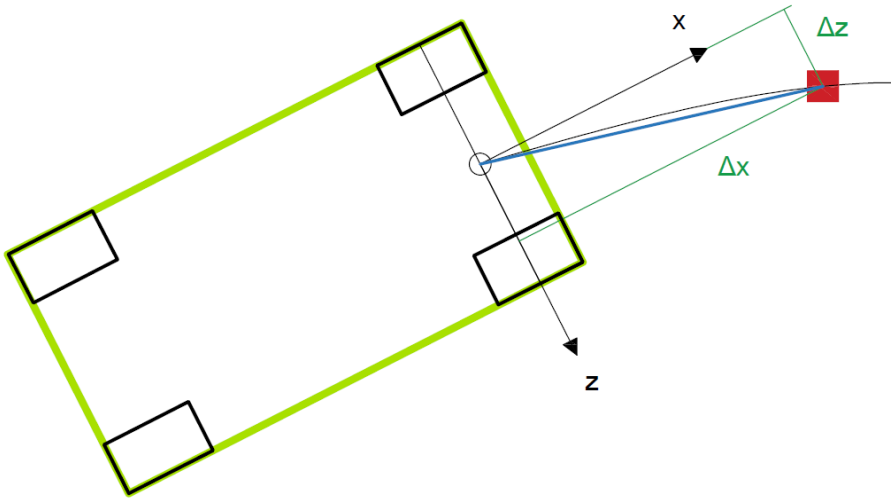

Figure 3.8: Slip steering

After calculating the angular error, the torque contribution, which is proportional to the angular error, is computed as shown in the equation 50. This contribution is added to the right wheel and subtracted from the left wheel (equations 51,52). If there is no 'longitudinal' torque contribution (T_{lat}), which is calculated by the longitudinal controller, the 'lateral' torque contributions will be opposite in sign, causing the vehicle to rotate around its own axis.

$$T_{lat} = k_p \cdot \Delta\alpha \tag{50}$$

$$T_{tot_r} = T_{long} + T_{lat} \tag{51}$$

$$T_{tot_l} = T_{long} - T_{lat} \tag{52}$$

k_p	$7.7 \cdot 10^4$

Table 7: Parameters of skid steering

3.2.4 Independent steering

The model described in this section describe the behaviour of an agriculture vehicle adopting an independent steering system. The starting model is the one described before and it is depicted in Figure 3.1. As said before, the element performing the steering is the support connected to the chassis through a hinge. This joint is placed

at the contact surface between the upper face of the support and the chassis and it allows the rotation of the support around the marker placed at the centre of the wheel, as it is possible to see in Figure 3.9. While, other constraints are common with the main model, the support and the wheel are connected to a bushing joint and the tyre-soil contact is the same as for the other models, which parameters are reported in Table 6.

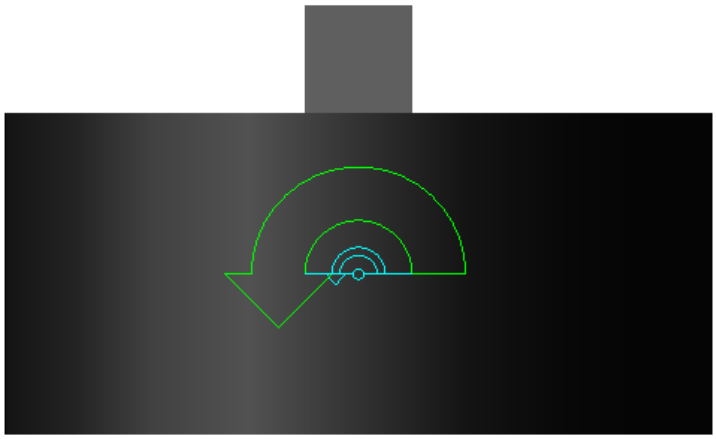

Figure 3.9: Independent wheel rotation

To implement this system, a lateral control was developed. This controller can evaluate the angle that needs to be applied to the wheels based on the angular difference between the vehicle's current direction and the desired direction. The angular difference is calculated using Equation 53, in which P is a constant parameter.

$$\Delta\alpha = tan^{-1}\left(\frac{\Delta z}{P}\right) \tag{53}$$

In Figure 3.10 it is shown in red the dummy body, and the two parameter Δz from the centre of the from axle to the dummy body in lateral direction (z) of the reference frame placed in the centre of the front axle.

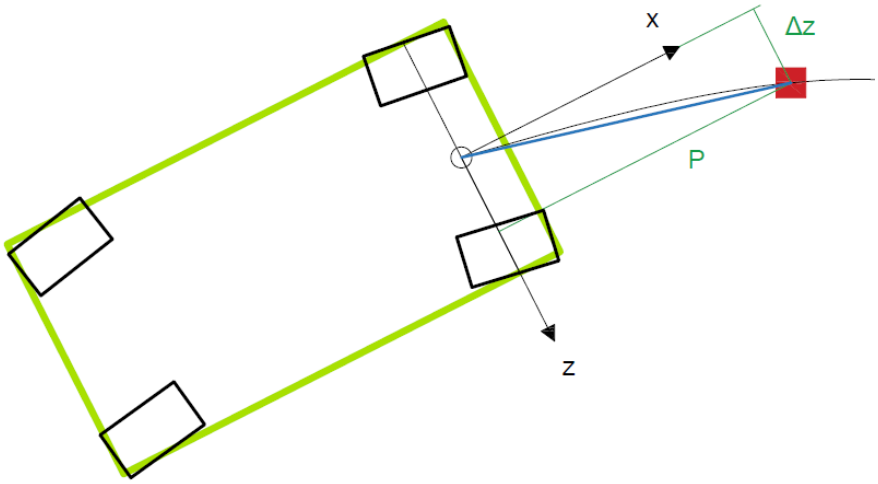

Figure 3.10: Independent wheel steering

Finally the value of the angle to be given to the front wheels is shown in the equation 54. How it is possible to see the value of the angle is defined using a proportional controller, so that the angle assigned to the wheel is proportional to the angular difference evaluated in the equation 53.

$$\alpha_{steer} = k_p \cdot \Delta\alpha \tag{54}$$

The angle assigned to the front left and front right wheel is the one evaluated in equation 54. The rear wheels angle is set to the same value of the front with opposite sign. Even if generally in vehicles with all wheel steering the rear wheels angle is a percentage of the front angle.

The constant of the controller k_p, is tuned based on the path described in section 3.3. The main parameter to be observed during the design of the controller, is the later error, Δz in Figure 3.10, in fact, the chose of the constant was made trying to minimize the lateral error.

k_p	60
P	600

Table 8: Parameters of independent steering

3.2.5 Ackerman steering

The Ackerman steering can be obtained designing a mechanism which respect the Ackerman condition, but it is actually a coordinated steering system for a particular

case. During the modeling process has been chosen to reduce the computational cost, by reducing the number of degree of freedom, implementing a mathematical relation between the front left wheel and the front right wheel. In this way it is possible to avoid a physical mechanism able to apply the Ackerman condition, avoiding so three more elements in the model.

The starting model is the one described in section 3.2. This time the 4 hinges allow the rotation between the supports and the chassis along an axis passing through the centre of the upper face of the support as it is shown in Figure. The tyre-soil contact is in common with the main model, as for what concern the bushing joint parameters and the dimensions of the vehicle.

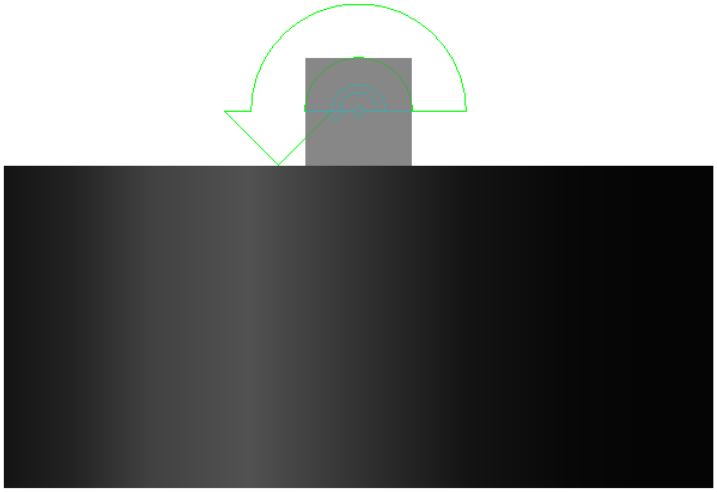

Figure 3.11: Vehicle model and dummy body

The lateral control is obtained through a proportional controller, which evaluates one of the front wheel angle value, as proportional to an angular error between the vehicle and the dummy body. The front wheel value is defined using equation 55, the relation is close to the one adopted for the independent steering system.

$$\alpha_{steer} = k_p \cdot tan^{-1}\left(\frac{\Delta z}{P}\right) \tag{55}$$

The value for the other angle is determined considering the Ackerman condition reported in equation 2.7, by rearranging the relation, it is then obtain the equation 56. In which β is the angle of the other wheel. as depicted in Figure 3.10.

$$\beta = cot^{-1}\left(\left(\frac{T}{L}\right) - cot(\alpha)\right) \tag{56}$$

The value of k_p and of P, from equation 55 are chosen during the design of the controller. In this phase the vehicle is testes on the path presented in section 3.3, the value of these constants are summarized in Table 9.

k_p	38
P	600

Table 9: Parameters of Ackerman steering

3.3 Virtual test environment

In order to test the developed models it is needed a common trajectory, representative of the main manoeuvres used in agriculture. This path it is used to tuned the constant of the controllers, and it is a sort of validation for the models. The trajectory in Figure 3.12 presents two manoeuvres, at first there is a double lane change, performed to analyse the behaviour of the vehicle in case of evasive maneuver to avoid an obstacle. The second part represents the typical maneuver performed in an orchard or vineyard during an activity. It is composed of two switchback turns, one on the left and one on the right, and finally an exit maneuver with a hairpin turn. The distance between the line have been chosen taking into account the spacing used in row construction. Typically, this spacing depends on the type of crop present in the plantation. For vineyards, the row spacing is generally between 1.5 and 2 meters for Guyot training systems, while for pergola systems, the spacing is between 4 and 5 meters. For fruit orchards, such as apples, pears, and plums, the row spacing is around 3 meters. Taking into account the previously done consideration and considering that the lateral dimension of the vehicle is 1.4 m, it has been chosen a distance between the line of the trajectory in the second part of 2 meters. By doing so the vehicle has to perform switchback turn of 1 meter.

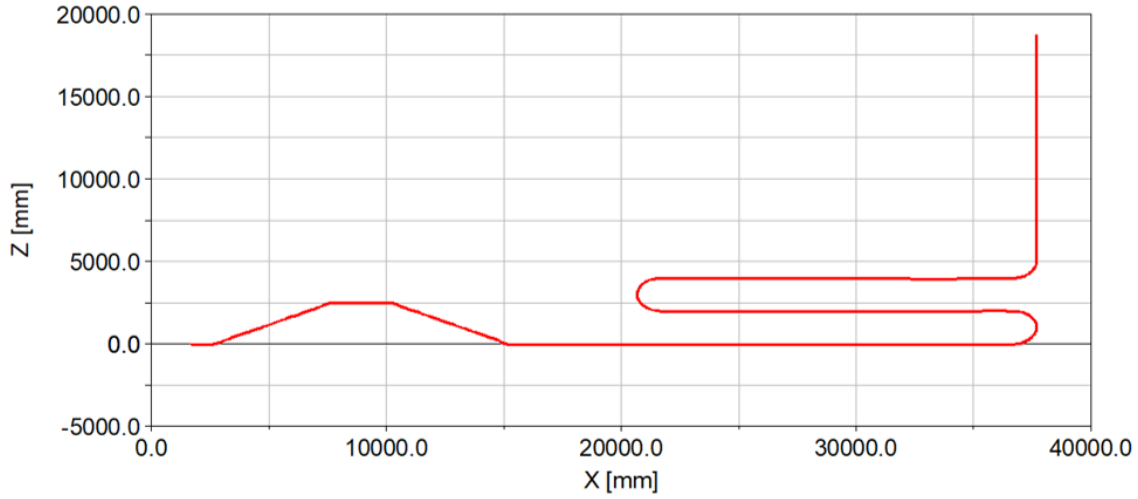

Figure 3.12: Overall test

In addition to the validation test, the models have been subjected to a sensitivity test. To conduct these tests, the path shown in the figure was constructed, it is a straight line with switch back turn at a certain point and for each simulation, one of the radii listed in the table 10 was tested.

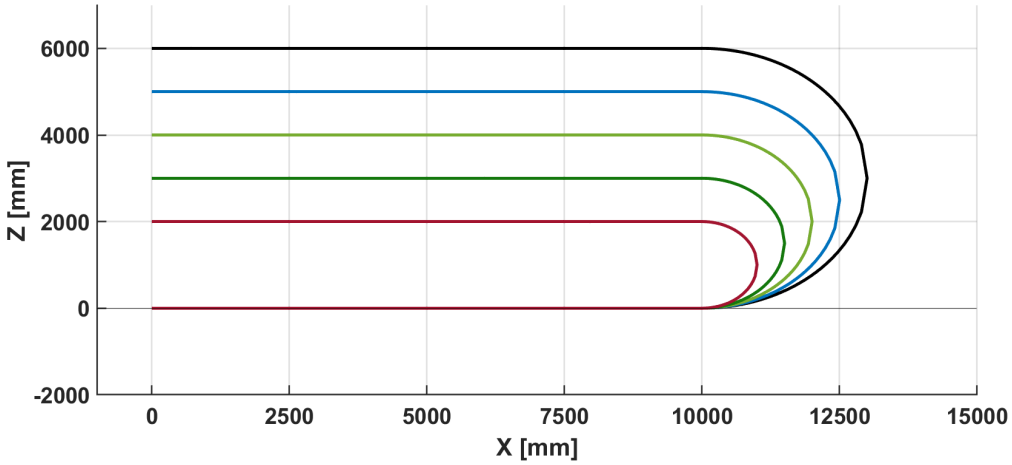

Figure 3.13: Sensitive analyses on radius

At the end of this test it is possible to define which is the sensibility of the vehicle to variation of the turn radius, in terms of lateral forces between wheels and ground, and lateral deviation. The objective of this test and the following test is also to analyze if possible lateral overturning during the maneuver, a very important aspect today in agriculture to avoid loss of load, damage to crops and equipment.

	Rasius $[m]$
TEST 1	1
TEST 2	1.5
TEST 3	2
TEST 4	2.5
TEST 5	3

Table 10: Sensitivity test radii

Another interesting test involves varying the vehicle's speed. Specifically, the speed is incremented to determine whether all models can perform the maneuver at any speed or if a limit speed can be identified. This might seem like a trivial test, but finding the model that can operate at even slightly higher speeds while maintaining safety can result in significant time savings, given the large number of such maneuvers typically performed in a field. The trajectory is shown in the figure 3.13; it is the same as in the previous test, but with a fixed radius set to *3* m, allowing for testing at higher speeds. In table 11 are reported the value of the speed for each test.

	Speed $[m/s]$
TEST 6	0.4
TEST 7	1
TEST 8	1.5
TEST 9	2
TEST 10	3
TEST 11	4

Table 11: Sensitivity test speed

3.4 Three-dimensional analyses

So far the analyses it is made on a 2D environment. To complete the dissertation, it is required to observe if the lateral slope or the longitudinal slope has influences on the dynamic behaviour. To investigate this phenomenon a new environment test path is generated. The trajectory is the one reported in Figure 3.14, it is composed of a right turn of a radius of *3* m.

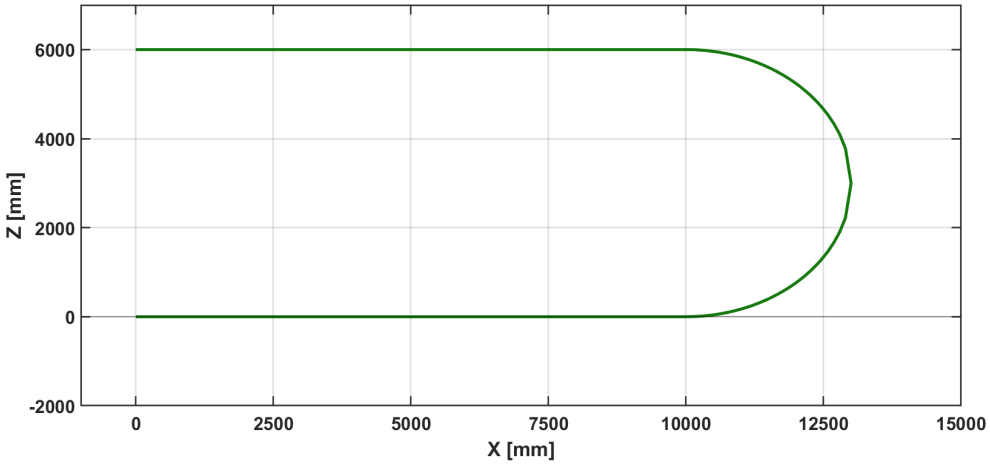

Figure 3.14: Trajectory for the vertical analyses

The vehicle is travelling at *0.5 m/s* and it is forced to face a lateral slope imposed by the object in Figure 3.15. The dimensions are reported in Figure 3.16.

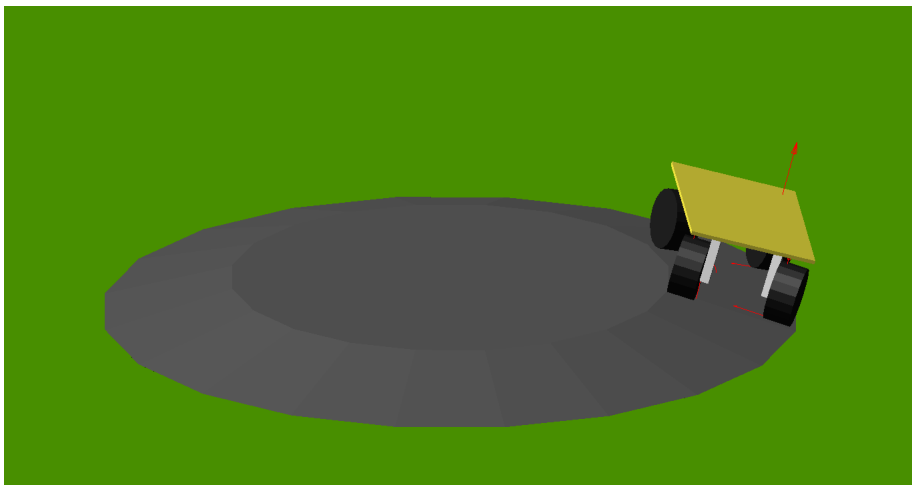

Figure 3.15: Obstacle

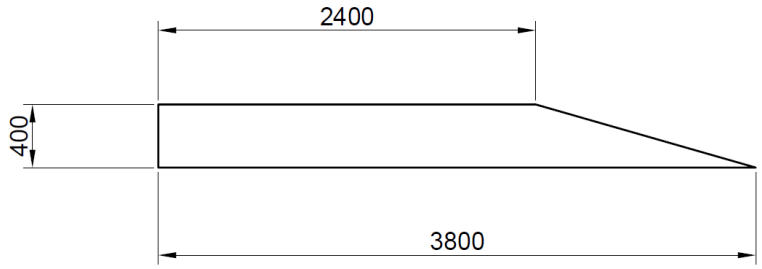

Figure 3.16: Obstacle (dimensions in *mm*)

To perform this type of analysis it was necessary to tune the lateral control again, especially for the transition from plane ground to tilted ground. With the previously defined constant most of the simulation end with a failure. The new parameters are reported in Table 12.

	Independent	Ackerman	Slip
k_p	60	38	$2.5 \cdot 10^5$
L	600	1800	-

Table 12: Lateral control parameter

3.4.1 Suspension

Besides the previous test a test on how the vertical displacement influenced the lateral behaviour has to be done. What it is required to confirm is a behaviour that it was found in the real prototype, When the rover encounters a bump or a pothole with one wheel, one of the others will loss the contact with the soil. This phenomenon will end in a dangerous condition, since the absence of contact will nullify the lateral force the wheel can exert on the ground and moreover, an overload on the remaining three wheels it is obtained. To better highlight this phenomenon a simulation using only a bump without lateral slope is done.

In Figure 3.17 is shown how the wheel on the left lost the contact due to the rigid chassis, when the wheel on the right is on the obstacle.

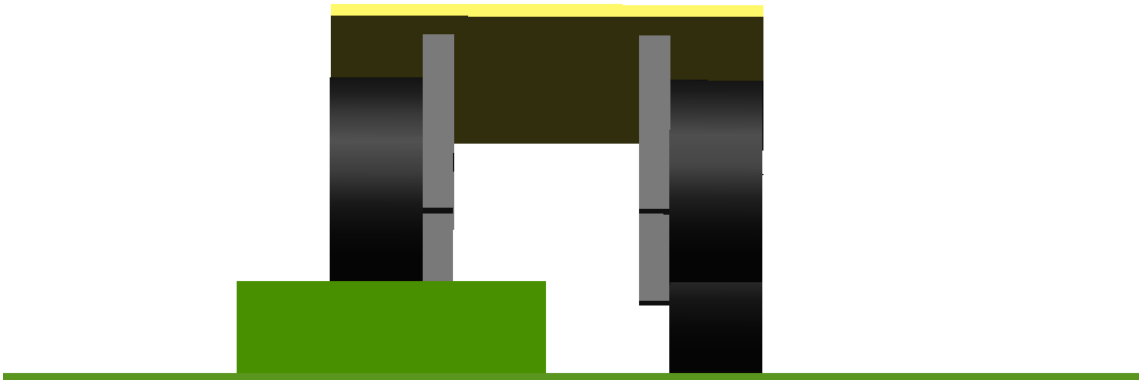

Figure 3.17: Simulation of a bump

Even though the vehicles in agriculture field and in general off-road vehicle are not adopting any suspension system, it is interesting to observe if the presence of an approximated suspension system could improve the vertical performance of the

vehicle, as well as the lateral behavior. Actually, they exist several example of front axle articulation in agriculture tractor that allow for accommodating the variations of terrain, in Figure 3.18 are reported some constructive solutions adopted by the leading tractor manufacturers.

Figure 3.18: Agriculture suspension system [1],[25],[14]

The model adopted for the simulation is the one depicted in Figure 3.19. This model is built to take into account the composition of the pre-existing prototype. Since the supports are connected directly to the chassis rigidly or by a hinge, four independent suspension need to be implemented. Now the supports are connected to the chassis through a hinge that allows the rotation around of the support (in the slip steering case the rotation is rigidly constrained) and that allows the vertical translation. Between the chassis and each support a spring with a stiffness of $4000\ N/m$ and a damping of $400\ Ns/m$ is placed, this will control the vertical translation approximating a real suspension.

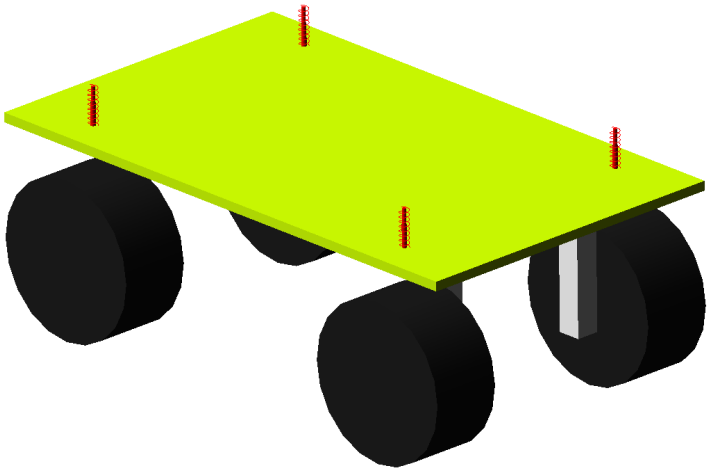

Figure 3.19: Model implementing a suspension

4 Comparison and Results

In this section will be present the main results of all the simulation, analyzing graph and comparison parameters. For each of the previously explained models will be reported a set of graph regarding the controls efficiency and the dynamic behaviour of the vehicle, for the trajectory tested.

4.1 Models comparison

4.1.1 Independent steering

The model adopting the independent steering system has been tested on the trajectory reported in Figure 3.12. As said before this trajectory has been specifically design to evaluate how the rover is moving inside an environment which try to simulate a real working condition. As first analysis the efficacy of the longitudinal control. For this model after several try the parameters of the longitudinal proportional-derivative controller has been chosen as reported in Table 13.

k_p	1200
k_d	600

Table 13: Longitudinal control parameters independent steering

With the controller shown above, the longitudinal error observed in the testing path is illustrated in Figure 4.1. Recalling that this parameter is evaluated as the distance between the dummy body and the vehicle's reference point, it is clear that the controller has been well-tuned. This is evidenced by the fact that only eight peaks appear throughout the entire test, indicating that the vehicle remains sufficiently close to the dummy body most of the time. Upon more detailed analysis of the graph in Figure 4.1, the presence of each peak can be explained. Starting from the left, the first small positive peak indicates that the vehicle is slightly distant from the dummy body, likely due to the initial speed of the vehicle being lower than the reference speed to prevent a failed simulation. At the start of the simulation, the vehicle is almost stationary, and a starting speed of *100 mm/s* is assigned to the chassis to prevent abrupt increases in torque as it attempts to match the dummy body's speed. In response to this positive peak, the controller applies torque to the wheels, causing the vehicle's speed to increase and bringing the longitudinal error back to zero. A steady-state condition is then reached, where the center of the front axle aligns with the dummy body marker. After reaching stability, the

vehicle performs its first turn, causing a slight decrease in speed and an increase in the distance between the bodies, resulting in another positive peak. The controller then increases the speed to compensate for the variation in distance, before reducing it again to around *400 mm/s*, stabilizing the longitudinal error close to zero. The remaining peaks follow the same pattern, with the largest peaks corresponding to the two turn-back maneuvers and the final one representing the vehicle's exit maneuver.

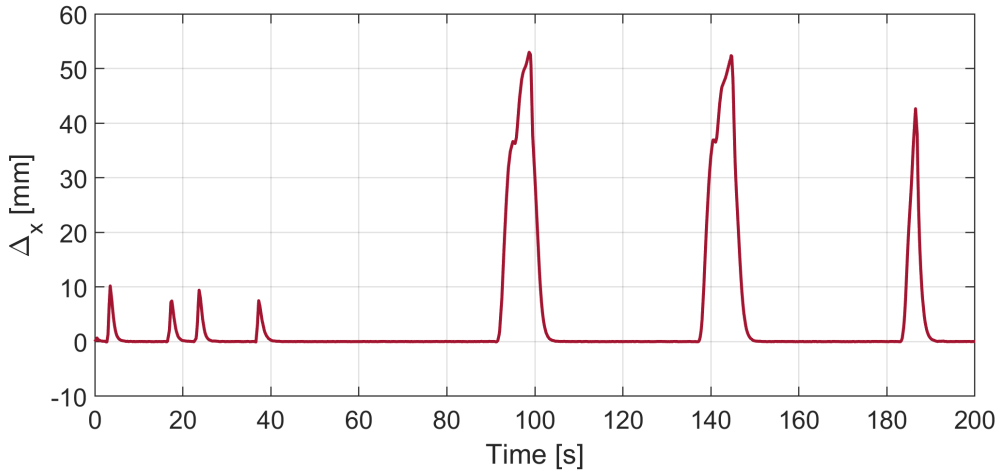

Figure 4.1: Longitudinal error - independent steering

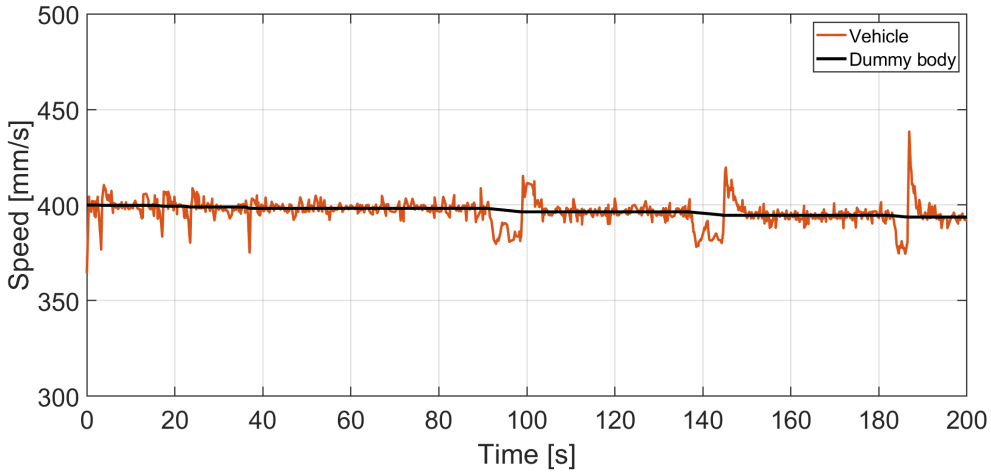

Figure 4.2: Speed of vehicle and dummy body - independent steering

As further confirmation of the controller's effective operation, the trend of the vehicle's speed is shown in Figure 4.2. It can be observed that the controller consistently tries to maintain the vehicle's speed close to the reference value, while also accounting for variations in the distance between the vehicle and the dummy body. Regardless of the sharpness of the curves, the vehicle's speed never drops below *370*

mm/s, demonstrating the controller's ability to keep the speed stable throughout the test.

The final aspect analyzed is the lateral precision of the steering controller, which also helps evaluate the performance of the current steering system. In particular, in Figure 4.3, the lateral error between the dummy body and the vehicle is shown, defined similarly to the longitudinal error in equation 46. Throughout the test path, the controller effectively maintains a small lateral error, indicating it has been well-tuned. The peaks observed occur during turns in the path and are caused by a slight delay between the dummy body and the vehicle, as well as the dynamics of the model. However, each time a perturbation arises, the controller successfully corrects the vehicle's position, keeping the lateral error as close to zero as possible without inducing any oscillation.

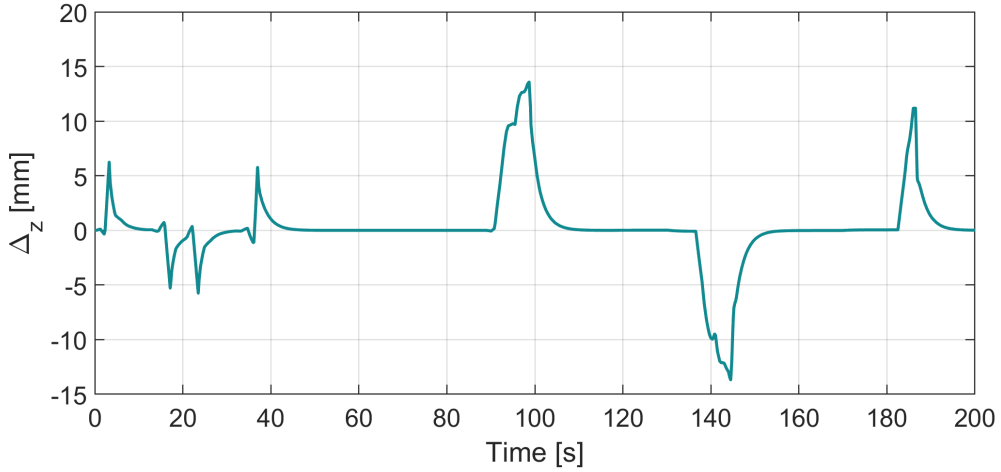

Figure 4.3: Lateral error - independent steering

In Figure 4.4 and in Figure 4.5 the lateral force trend is displayed. Analyzing the three main peaks, it is evident that during turns, there is a load transfer from the inside to the outside of the turn, as described in section 2.2.1 in Figure 2.12. In particular, when the vehicle approaches a right turn, the vertical load on the left side increases due to this load transfer, resulting in a corresponding rise in lateral force on the left wheels. This can be observed in Figure 4.4 , where in the first major peak, the blue line (indicating the lateral force on the front left wheel) is higher than the orange line (representing the front right wheel), confirming that the vehicle is turning to the right. A similar but inverse behavior occurs during the second turn, which is to the left. In this case, the right side of the vehicle is more heavily loaded than the left, resulting in higher lateral forces on the right wheels.

The same pattern is seen for the third main peak and even in the smaller peaks, though it is less pronounced.

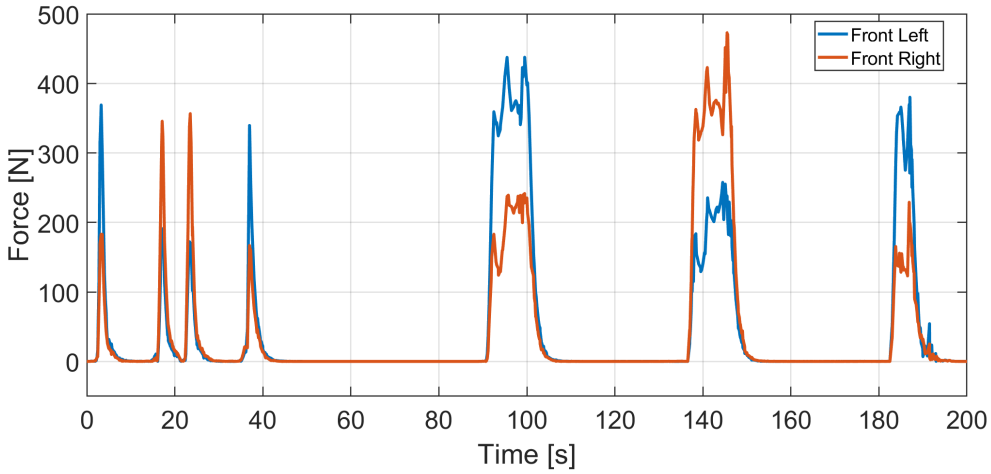

Figure 4.4: Lateral force front axle - independent steering

The behaviour previously explained works in the same way for the rear axle. In Figure 4.5 is reported the trend of the lateral forces on rear wheels.

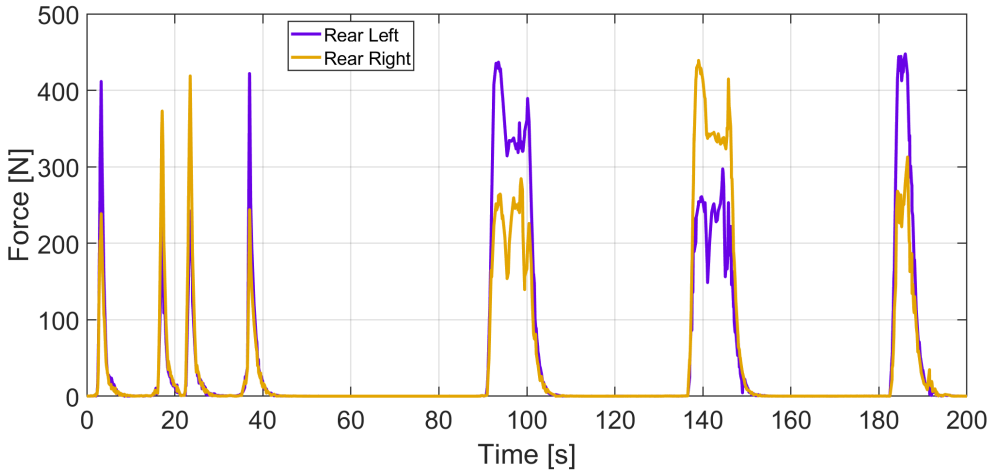

Figure 4.5: Lateral force rear axle - independent steering

4.1.2 Ackerman steering

The model using the Ackerman steering system was tested on the trajectory shown in Figure 3.12. The calibration process yielded the values listed in Table 14. For these calibration parameters, the results related to longitudinal error, vehicle speed, and lateral error are explained in detail below.

k_p	1100
k_d	700

Table 14: Longitudinal control parameters Ackerman steering

As explained for the independent steering model, the effectiveness of the longitudinal controller is evaluated by analyzing the longitudinal error and the vehicle's speed. The longitudinal error shows some variations due to the turns within the path. At each disturbance, the controller reduces the longitudinal error. Compared to the previous model, the peaks are slightly lower, but there are smaller peaks before each disturbance.

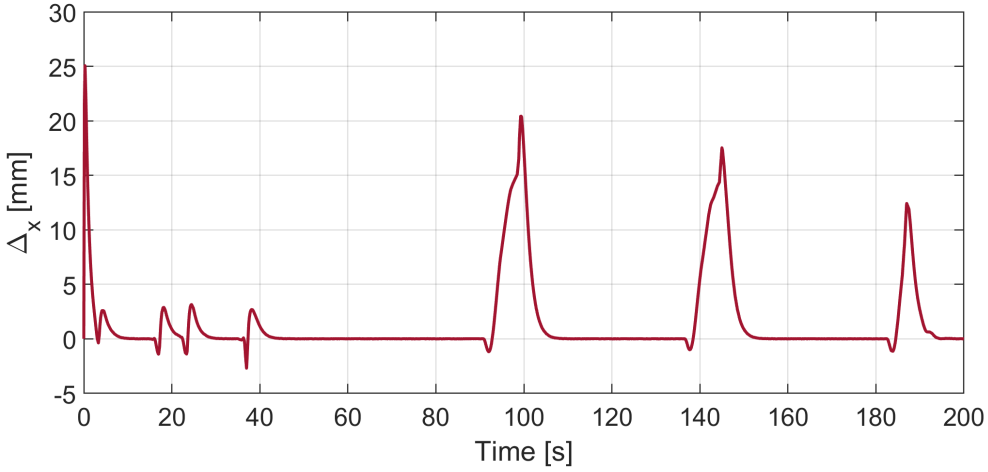

Figure 4.6: Longitudinal error - Ackerman steering

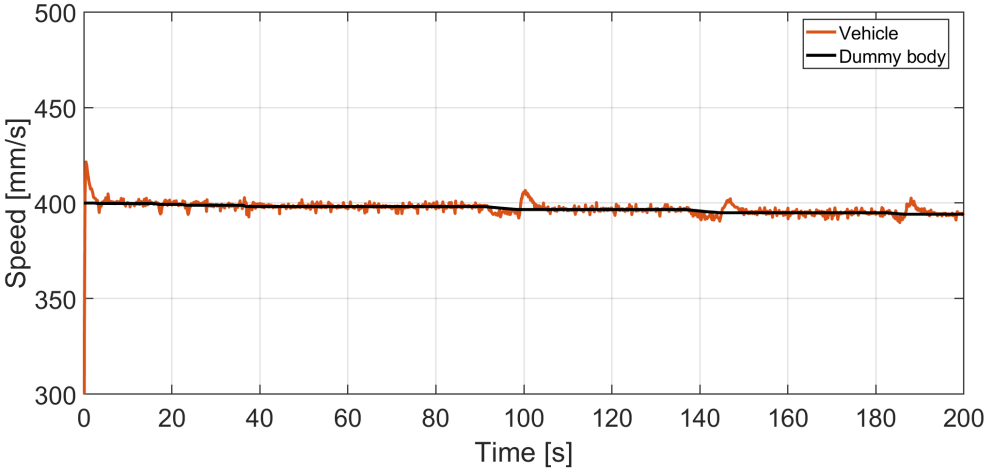

Figure 4.7: Speed of vehicle and dummy body - Ackerman steering

In Figure 4.7,the trend of the vehicle's speed is displayed. After the initial seconds of simulation, during which the vehicle accelerates from *100 mm/s*, this initial speed is intentionally set to prevent extreme variations in the torque applied to the wheels, the vehicle speed stabilizes around the reference value.

Considering the lateral behavior, the graph in Figure 4.8 reveals several peaks. After each turn, the controller successfully reestablishes an equilibrium condition, bringing the lateral error close to zero. The performance in terms of lateral error is nearly equivalent to that of the independent steering system. The lateral error in the Ackerman system varies almost continuously, whereas the independent steering system exhibits two or three distinct steps in the lateral error. This discrepancy can be attributed to the less precise nature of the steering system, particularly regarding how the steering angles are defined. In the Ackerman steering system, the angles between the inside and outside wheels during a turn are different, and the relationship between them is optimized to achieve an almost perfect turn without tire slipping. Conversely, in the independent steering system, the angles are set to be equal, which is not an optimal choice. In areas where no turns are present, the controller effectively restores a steady-state condition, allowing the vehicle to proceed without lateral oscillations.

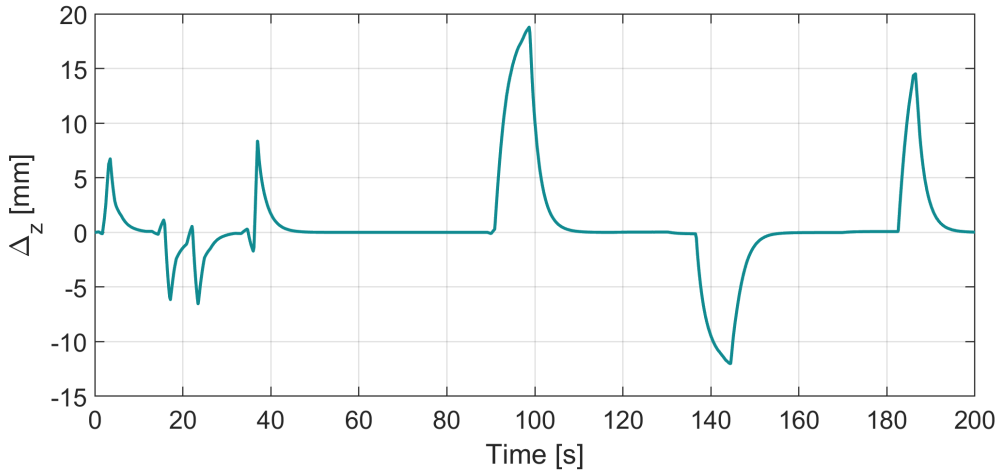

Figure 4.8: Lateral error - Ackerman steering

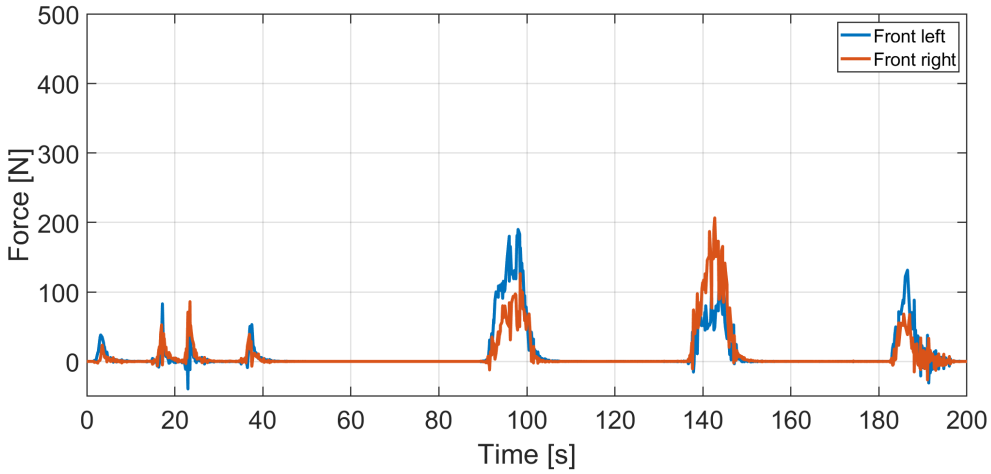

Figure 4.9: Lateral force front wheel - Ackerman steering

In Figure 4.9 and in Figure 4.10 the trends of the lateral forces are presented. The observations made for the independent steering case apply here as well. Specifically, the wheel on the outside of the turn experiences an increase in vertical load, which induces a higher lateral force compared to the inside wheel. Notably, the maximum value of the lateral force in this scenario is only half of the maximum amplitude observed in the independent wheels case. This indicates that, under the same conditions—such as vehicle speed and turning radius—the lateral force exerted by each wheel in the Ackerman system is lower. Consequently, by employing the Ackerman mechanism, the vehicle can operate under more challenging conditions in terms of friction and speed while executing a turn, before reaching the saturation point of the lateral forces, and also the structure is less stressed.

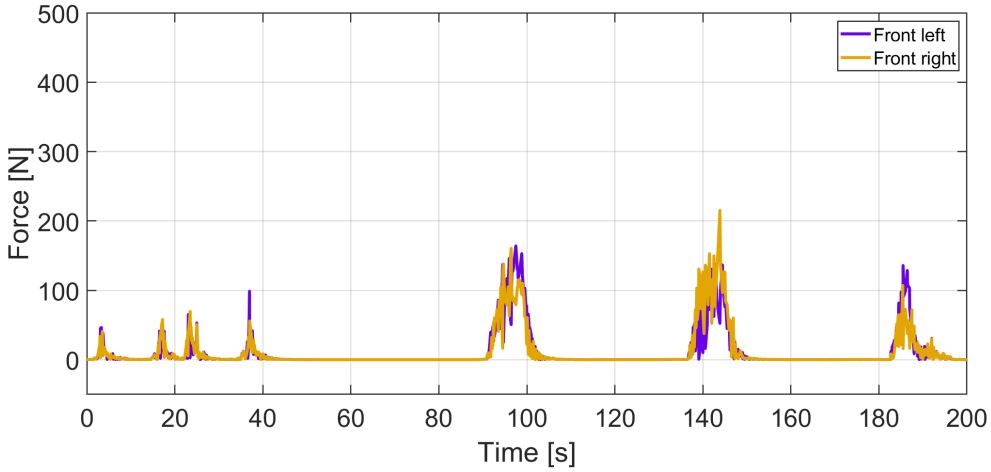

Figure 4.10: Lateral force rear wheel - Ackerman steering

4.1.3 Slip steering

The model utilizing torque vectoring control strategies has been tested on the designated testing path, with the constants for the longitudinal controller presented in Table 15. Its calibration process proved to be particularly challenging for this specific model. On several occasions, certain combinations of parameters caused the simulation to fail, even though the conditions applied were consistent with those of the other models. This issue was primarily attributed to the jerky movements of the model, which resulted in significant fluctuations across all variables. To mitigate simulation failures, one potential solution is to increase the number of simulation steps or to reduce the step size. However, both approaches would lead to an extended simulation time.

k_p	1400
k_d	600

Table 15: Longitudinal control parameters slip steering

The vehicle speed is adjusted based on the evaluation of the longitudinal error, as depicted in Figure 4.12. Similar to the other models, the graph displays several prominent peaks; however, compared to the Ackerman and independent steering systems, each peak exhibits significant oscillations. This behavior is evident during the simulation, where the vehicle rotates in discrete steps and oscillates around the reference trajectory. This can be understood also observing Figure 4.14, which shows the path traced by the center of the rear axle in comparison to the reference trajectory.

The amplitude of the peaks is comparable to those observed in Figures 4.1 and 4.6. All the oscillations depicted in Figure 4.13 are a result of the steering action; the differential torque induces slippage that causes the vehicle to decelerate. Consequently, the vehicle alternates between moving closer to and further away from the reference trajectory.

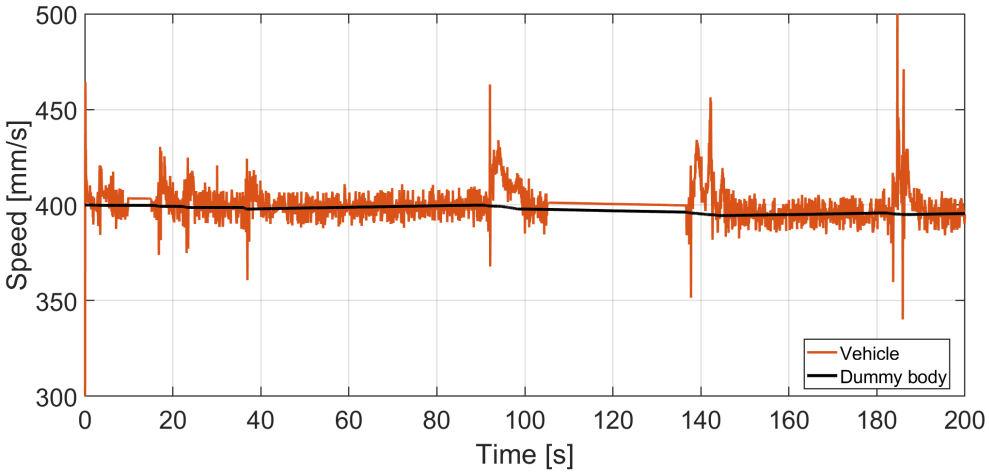

Figure 4.11: Speed of vehicle and dummy body - Slip steering

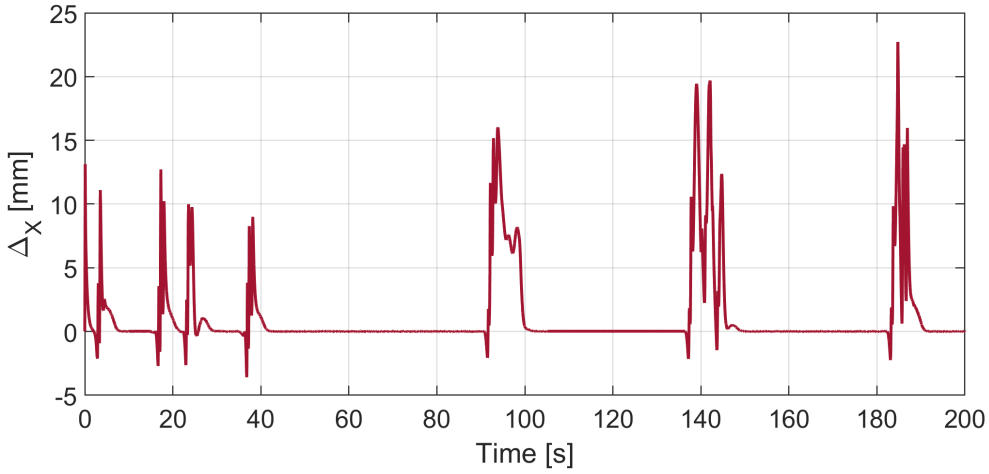

Figure 4.12: Longitudinal error - Slip steering

The efficacy of the lateral controller is assessed by observing the lateral error shown in Figure 4.13. When a turn occurs, a perturbation is introduced, prompting the controller to apply a differential torque between the two sides. After encountering this perturbation, the controller successfully maintains the lateral error close to zero, demonstrating effective operation. However, the peaks observed during turns are higher compared to those in previous models, indicating that this type of steering is less effective. Additionally, the main peaks exhibit numerous rapid oscillations, which stem from the nature of the steering system, suggesting an unstable condition.

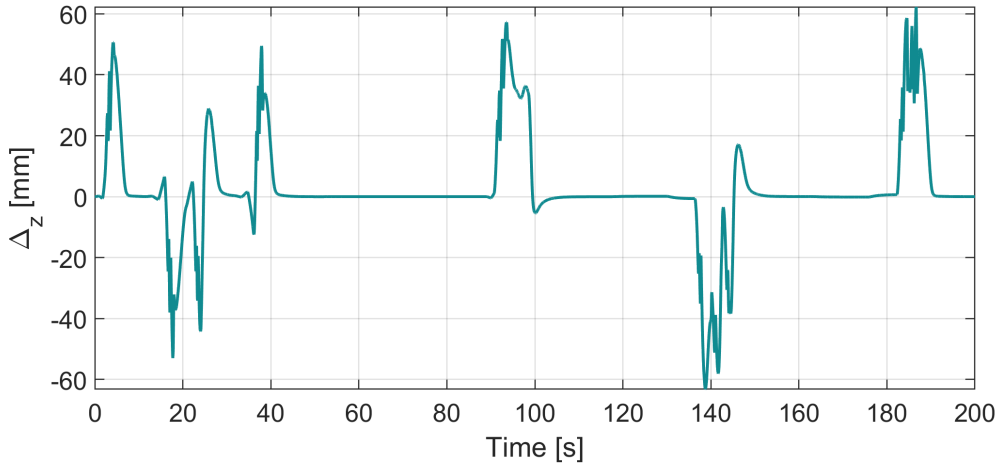

Figure 4.13: Lateral error - Slip steering

To highlight the controller's poor performance and the jerky movement of the rover, one can refer to Figure 4.14. The trace left by the center of the rear axle deviates significantly from the reference trajectory. Even during small turns, the lateral error at the rear is noticeably high, although the jerky movement is less apparent. In contrast, during larger turns, the abrupt movements become highly visible, as evidenced by the resultant sliding of the rear wheels. This erratic behavior could potentially lead to contact between the rover and the cultivated row, resulting in damage and hazardous situations.

Figure 4.14: Trace of rear axle - Slip steering

This behavior is less pronounced in the models utilizing the independent steering system and the Ackerman steering system, as shown in Figures 4.15 and 4.16. In both cases, the traces are smooth and continuous, demonstrating consistent movement during small turns as well as sharp hairpin turns, without any jerks. This confirms that the first two models exhibit superior performance in this aspect.

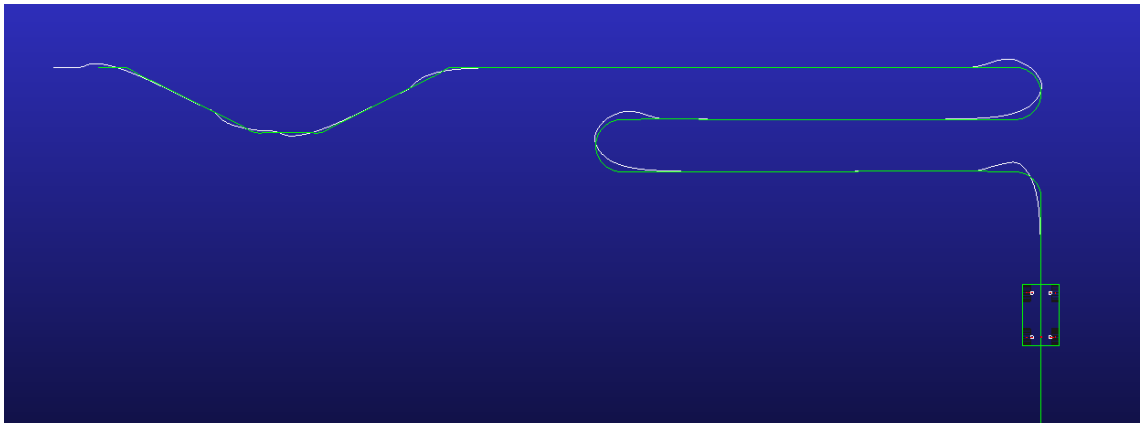

Figure 4.15: Trace of rear axle - Independent steering

Additionally, since steering is also implemented in the rear axle, the rear wheels have a reduced tendency to be dragged laterally. In fact, the steering on the rear axle enhances the vehicle's ability to maintain its trajectory, ensuring that the center of the rear axle stays aligned with the intended path.

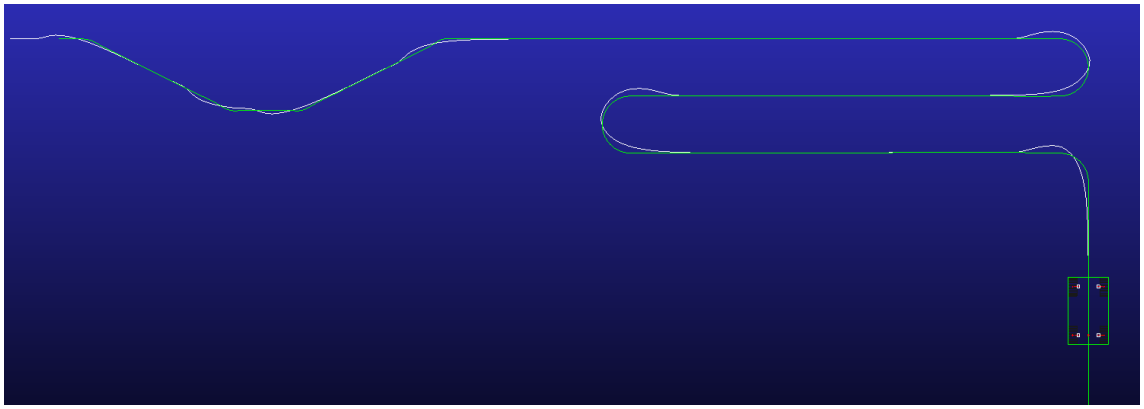

Figure 4.16: Trace of rear axle - Ackerman steering

The final aspect analyzed here is the lateral force behavior for the slip steering system. The graphs in Figure 4.17 and Figure 4.18 present numerous oscillations, making their interpretation quite challenging. These oscillations further confirm the jerky movement of the vehicle. Unlike the independent steering and Ackerman systems, it is difficult to clearly identify a lateral load transfer in this case. However, as the lateral force diminishes during the oscillations, approaching zero, the vehicle enters a condition where it cannot exert sufficient force, leading to instability. For the three larger peaks, the amplitude of the lateral force is actually lower, due to the lateral slip that occurs. This slip is intrinsic to the slip steering system and can be interpreted as a form of lateral force saturation, limiting the vehicle's performance during sharp turns.

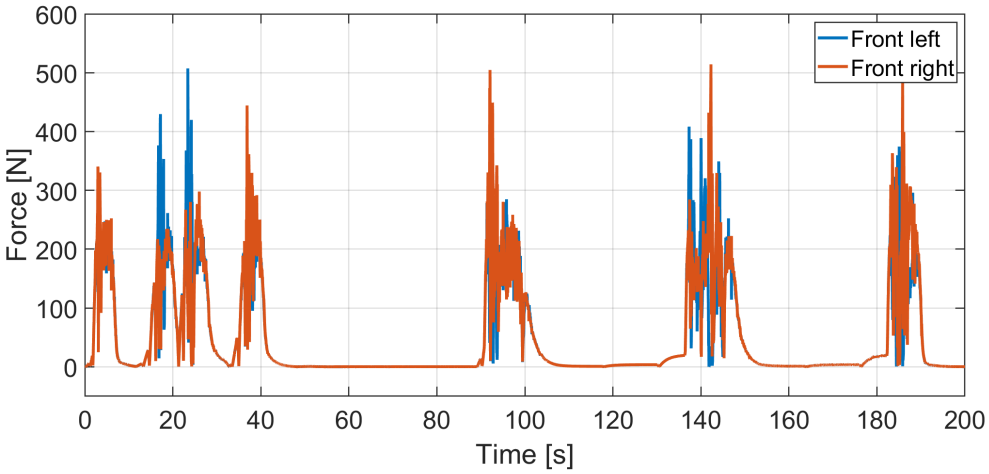

Figure 4.17: Front left lateral forces - Slip steering

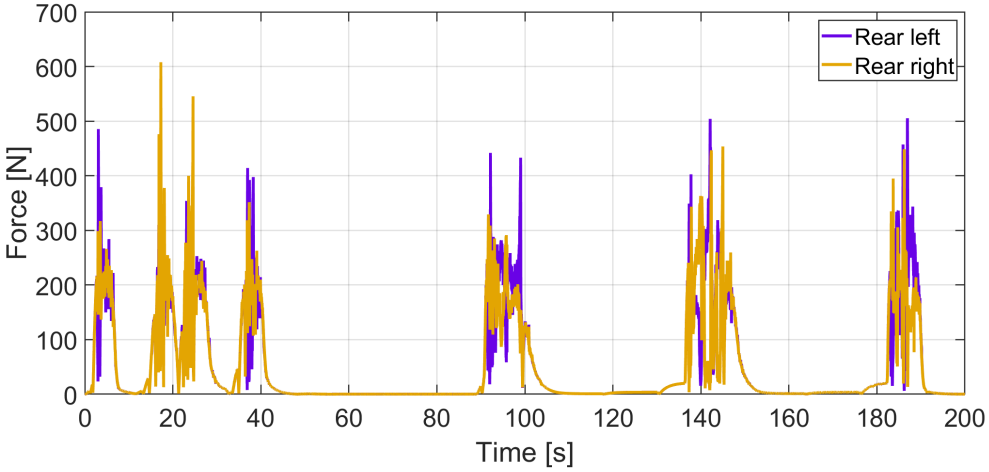

Figure 4.18: Rear left lateral forces - Slip steering

4.1.4 Radius Sensitivity test

This section presents the results of the sensitivity analysis on the turning radius. The goal of this test is to observe how variations in the turning radius affect key vehicle parameters. In the subsequent discussion, not only will the lateral behavior be analyzed in terms of lateral deviation and lateral force, but also the deceleration caused by approaching a turn will be evaluated by observing the longitudinal error. This will provide a more comprehensive understanding of how different turning radii impact the vehicle's dynamic response.

Ackerman steering Starting with the Ackerman steering system, the longitudinal behavior is analyzed first. From Figure 4.19, it can be observed that as the

turning radius increases from 1 meter (*TEST 1*) to 3 meters (*TEST 5*), the longitudinal error decreases. This indicates that when the vehicle navigates a turn with a larger radius, the deceleration is slightly lower, which is an expected outcome. Additionally, it is noteworthy that as the turning radius increases, the number of oscillations in the longitudinal error decreases, along with a reduction in their amplitude. This suggests a smoother overall movement with less pronounced variations as the vehicle navigates turns with larger radii.

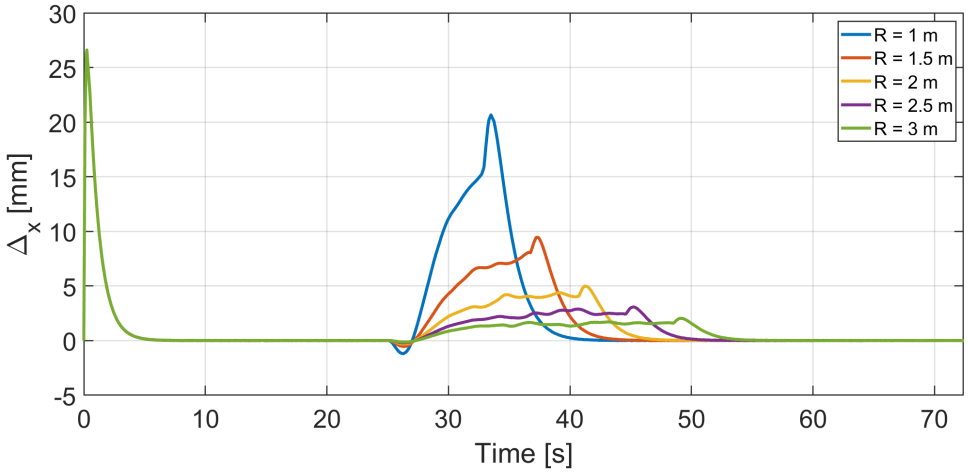

Figure 4.19: Longitudinal error - Radius sensitivity test (Ackerman steering)

To examine the lateral behavior, we start by analyzing the lateral error presented in Figure 4.20. The trend of the lateral error is quite similar to that of the longitudinal error. Specifically, as the radius of curvature increases, the lateral error decreases. Even when the radius is as small as 1 meter (*TEST 1*), the maximum lateral error reaches approximately *20 mm*. This indicates that even for tight turns, the controller performs effectively.

The Ackerman steering system under investigation demonstrates the ability to handle very small turning radii, which is a crucial feature for agricultural vehicles, where maneuverability in confined spaces is often required.

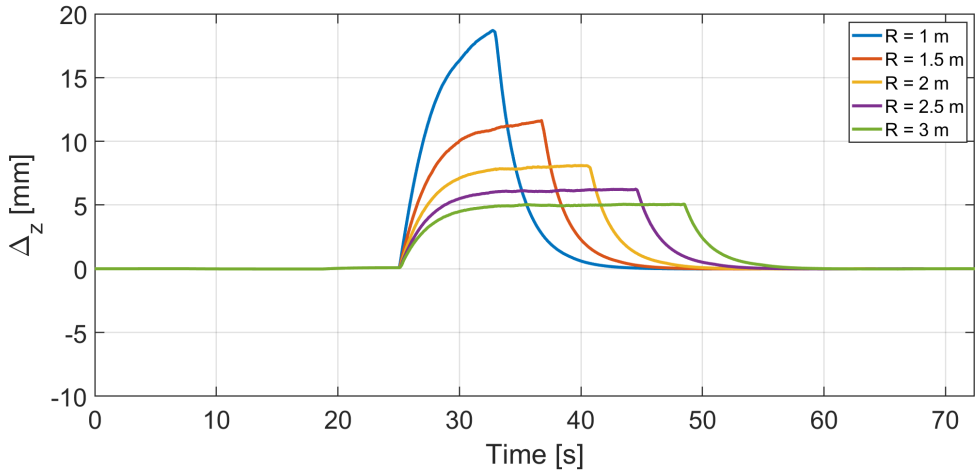

Figure 4.20: Lateral error - Radius sensitivity test (Ackerman steering)

Before analyzing the behavior of the lateral force, it's important to review some theoretical concepts to establish the expected outcomes. By examining Equation 11, we can deduce that, while keeping both the vehicle's mass and speed constant, an increase in the turning radius results in a decrease in centrifugal force. Since the centrifugal force is distributed between the front and rear axles, as shown in Figure 2.13, and initially divided equally between the wheels on each axle, the force exerted on each individual wheel decreases as the radius increases. This is precisely what we observe in the simulation results in Figure 4.21. Here, it is evident that the lateral force on the front left wheel decreases with an increase in the turning radius, aligning with the theoretical expectations.

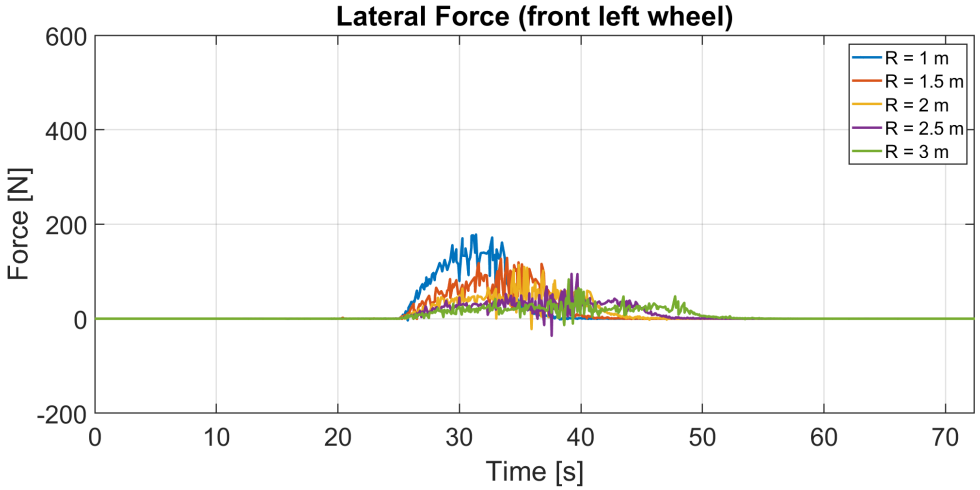

Figure 4.21: Front left force - Radius sensitivity test (Ackerman steering)

To complete the discussion, Figures 4.22 and 4.23 display the steering angles of

the front left and front right wheels, respectively. Both graphs follow a similar trend to the longitudinal and lateral error: as the turning radius increases, the steering angle of the wheels decreases. This behavior is consistent with the theoretical relationships described in Equation 4 and Equation 6. These equations indicate that when the turning radius increases the steering angle δ_f decreases. Additionally, these graphs highlight the interaction between the left and right wheels in the Ackerman steering system, where the angle of the inner and outer wheels adjusts proportionally to ensure optimal turning with minimized tire slippage. This illustrates the Ackerman geometry's role in facilitating smooth and efficient cornering.

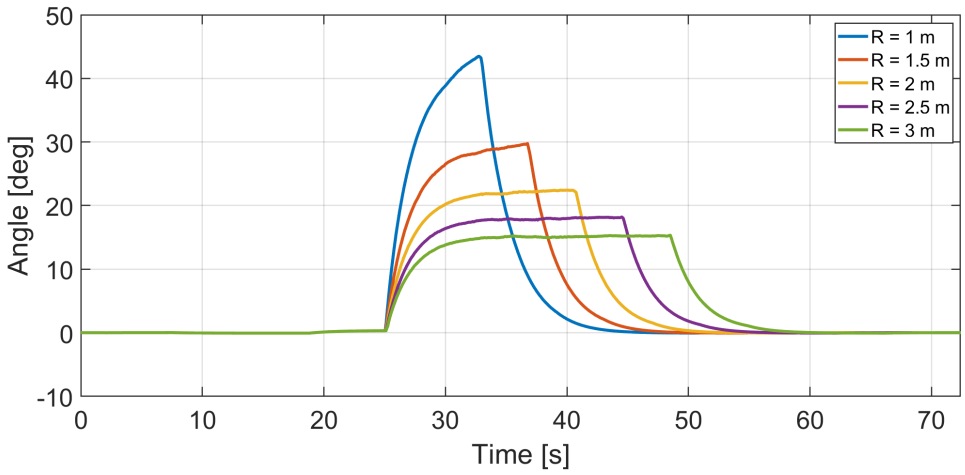

Figure 4.22: angle left - Radius sensitivity test (Ackerman steering)

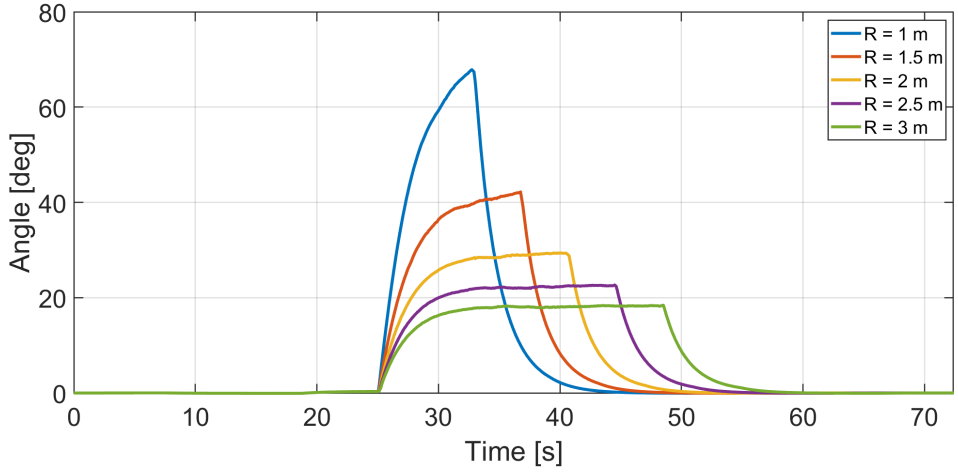

Figure 4.23: angle right - Radius sensitivity test (Ackerman steering)

A further consideration is necessary regarding the steering limits of agricultural vehicles. In front-wheel steering systems commonly used in such vehicles, the maxi-

mum steering angle typically ranges between 50° and 60°. In Figure 4.22, the highest steering angle corresponds to the right wheel, as the vehicle is approaching a right turn, while the left wheel shows a smaller angle. For *TEST 1*, which represents a turning radius of 1 meter, the right wheel's steering angle exceeds this typical limit, indicating that such a tight turn would not be feasible for standard agricultural vehicles. However, in *TEST 2*, with a radius of 1.5 meters, the right wheel's steering angle reduces to approximately 40°, which is within the acceptable range. This suggests that a turning radius of 1 meter is beyond the practical limit for such vehicles, and the realistic minimum radius for maintaining acceptable steering angles lies somewhere between 1 meter and 1.5 meters. This information is critical for designing steering systems that meet the operational constraints of agricultural machinery.

Independent steering The results of the sensitivity analysis on the independent steering system are presented in this section. As observed with the Ackerman steering model, the longitudinal error decreases as the turning radius increases. However, in the case of the independent steering system, the reduction in longitudinal error occurs more rapidly. This is due to the fact that the outer wheel's steering angle is less incorrect when compared to the Ackerman steering model, especially in cases with larger turning radii. In Figures 4.23 and 4.22, it can be observed that for a radius of *2.5 m* and *3 m*(*TEST 4* and *TEST 5*), which correspond to the largest turning radii in the analysis, the difference between the left and right steering angles is less than 5°. This close alignment of steering angles ensures smoother turning behavior and reduces longitudinal error. On the other hand, for *TEST 1*, where the turning radius is the smallest (1 meter), the error in one of the wheel's steering angles reaches 30°, leading to a much higher longitudinal error, as shown in Figure 4.24. This confirms that tighter turns result in significant deviations between the intended trajectory and the actual path, especially when the steering angles are not optimized for such small radii.

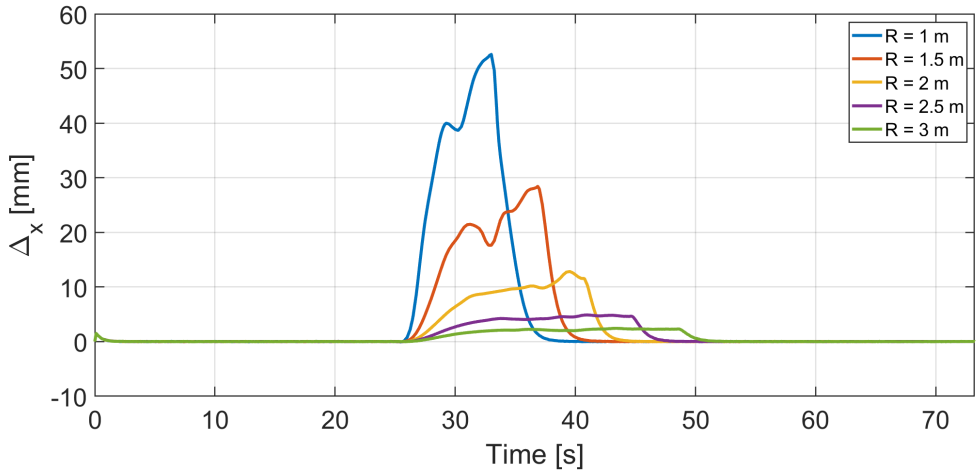

Figure 4.24: Longitudinal error - Radius sensitivity test (Independent steering)

The trends observed in the longitudinal error for the independent steering model can also be applied to the lateral error. In this model, the lateral error exhibits oscillations that were not as evident in the Ackerman steering mechanism. These oscillations indicate that the system requires more frequent corrections in terms of steering angle adjustments. This can be seen in Figure 4.27, where fluctuations in the steering angle correspond to corrections made to reduce lateral error. As the turning radius increases, these oscillations in the lateral error decrease both in number and amplitude. By the time we reach *TEST 4* and *TEST 5* (radius of *2.5 m* and *3m*) the oscillations have almost completely disappeared. The lateral error becomes smoother and more stable during the turns, with minimal fluctuations. This smooth behavior is reflected in the angle trends as well. Despite the presence of initial oscillations in tighter turns, the maximum lateral error peak remains relatively low. The peak values are comparable to those observed with the Ackerman steering mechanism, showing that, overall, the independent steering system maintains good lateral accuracy, particularly as the turning radius increases.

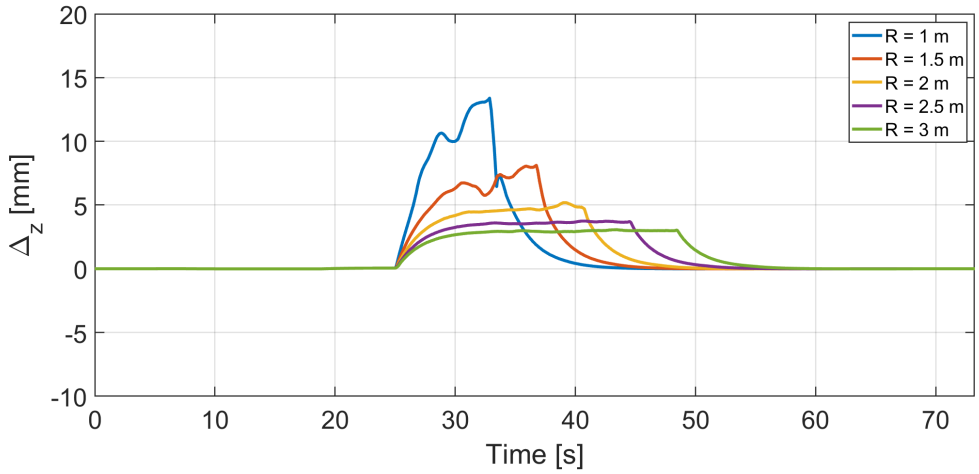

Figure 4.25: Lateral error - Radius sensitivity test (Independent steering)

As the turning radius increases, the centrifugal force acting on the vehicle decreases, which in turn leads to a reduction in the lateral forces exerted on the wheels. This trend is evident in Figure 4.26, where moving from *TEST 1* to *TEST 6* corresponding to an increase in the turning radius—the lateral force exerted by the wheel diminishes. With a larger radius, the system achieves more stable driving conditions, resulting in less oscillation in the lateral forces. This smoother behavior reflects the improved stability of the vehicle at higher turning radii. However, it is important to note that the maximum amplitude of the lateral force in this independent steering system is consistently higher for every test compared to the values observed in the Ackerman steering system.

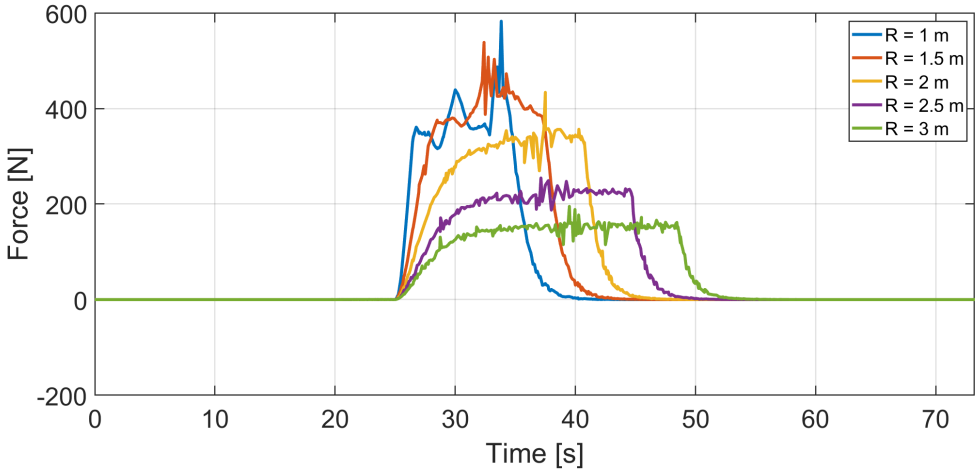

Figure 4.26: Front left force - Radius sensitivity test (Independent steering)

The angle trend illustrated in Figure 4.27 has already been addressed in relation

to the lateral error. In the case of the independent steering system, each wheel is designed to rotate independently around its own axis, allowing for full rotation capability. This unique feature eliminates any angular limits, making all test cases feasible with this model. Additionally, the independent steering system does not impose a minimum turning radius. The vehicle can execute a complete rotation around its own axis without any forward movement simply by rotating each wheel by 90 degrees. In such a scenario, the effective turning radius approaches zero, showcasing the system's remarkable maneuverability and flexibility in tight spaces.

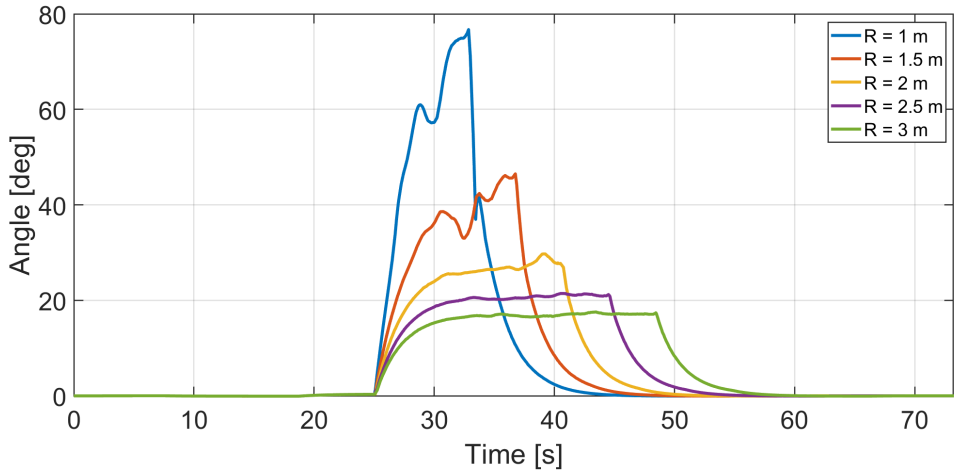

Figure 4.27: Front angle - Radius sensitivity test (Independent steering)

Slip steering What is found in Figure 4.28 is the longitudinal behavior. As seen in the overall test, there are many oscillations present. Increasing the turning radius tends to decrease their amplitude, and for very large radii, the number of oscillations also decreases.

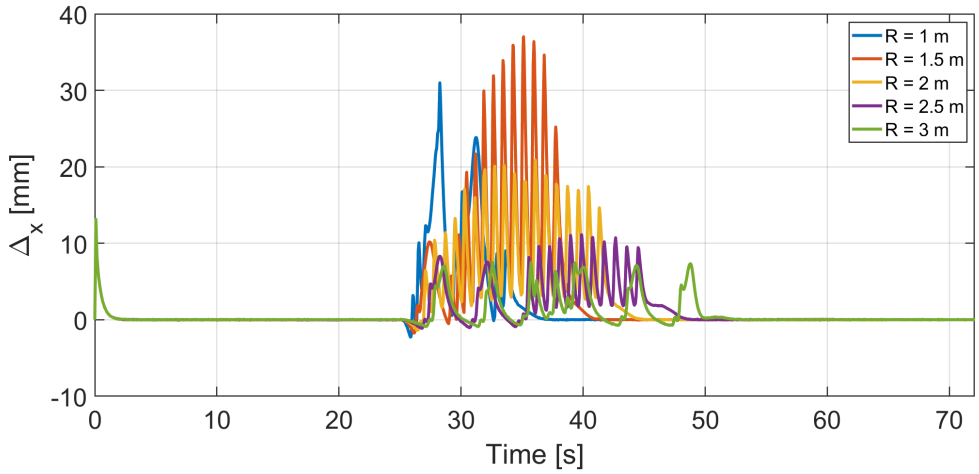

Figure 4.28: Longitudinal error - Radius sensitivity test (Slip steering)

The lateral error exhibits an oscillatory behavior similar to that of the longitudinal error. In this case, the amplitude is not significantly affected by the turning radius. Even with a large radius, the controller struggles to stabilize the lateral behavior, indicating that this steering system has low performance. Observing the green line, which represents TEST 5, one can see how the controller operates and the resulting jerky movements.

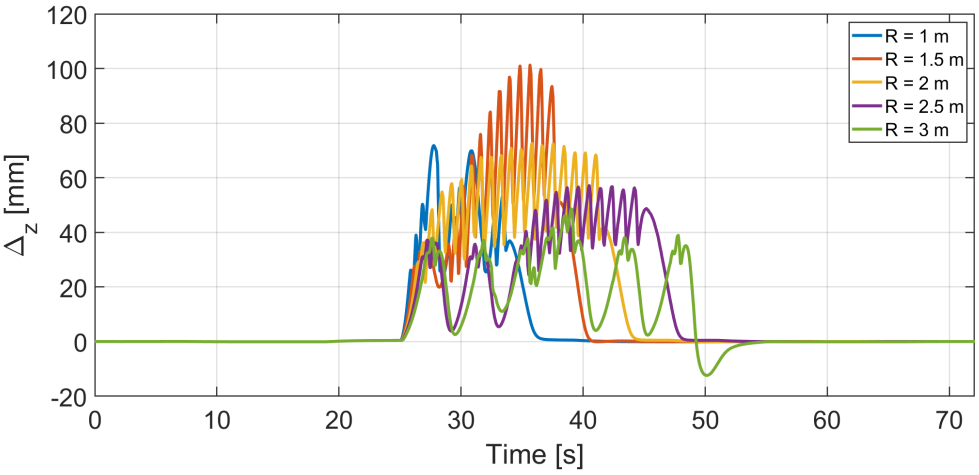

Figure 4.29: Lateral error - Radius sensitivity test (Slip steering)

The lateral force in this case is not affected by the turning radius. This actually goes against what is defined in theory, making it difficult to explain such behavior, particularly for very negative instantaneous peaks. These abrupt variations may produce uncontrolled lateral slipping, and when the turning radius is increased, the

controllability of the vehicle is improved, the fluctuations in the force are more bounded.

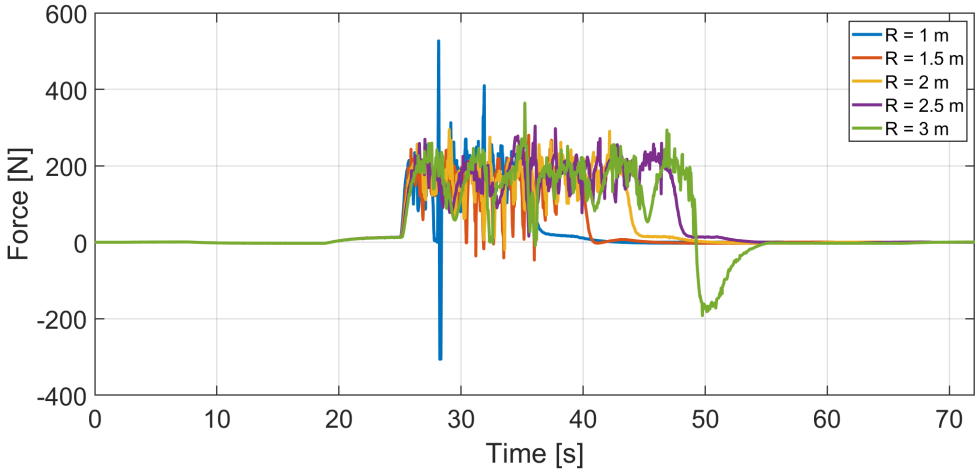

Figure 4.30: Front left force - Radius sensitivity test (Slip steering)

4.1.5 Speed Sensitivity test

This test is designed to evaluate how a vehicle's performance changes in response to variations in speed. It is particularly relevant in automotive testing to assess stability, control accuracy, and overall behavior at different speeds. The test helps define the critical speed beyond which performance may degrade, potentially leading to instability and a loss of control.

Indepedent steering The first model analyzed is the one utilizing the independent steering system. The longitudinal behavior is assessed to determine if the longitudinal controller functions effectively under varying vehicle speeds. At the beginning of the simulation, a significant peak is observed due to the initial speed assigned to the vehicle being lower than that of the dummy. This precaution is necessary to avoid simulation failures. In addition to this initial peak, it is evident that as vehicle speed increases, longitudinal error also increases. Additionally, small oscillations begin to appear, indicating that the controller may require re-tuning for higher speeds. Nonetheless, even in *TEST 6*, where the vehicle speed reaches *4 m/s* (approximately *15 km/h*), the longitudinal error remains below *10 mm*.

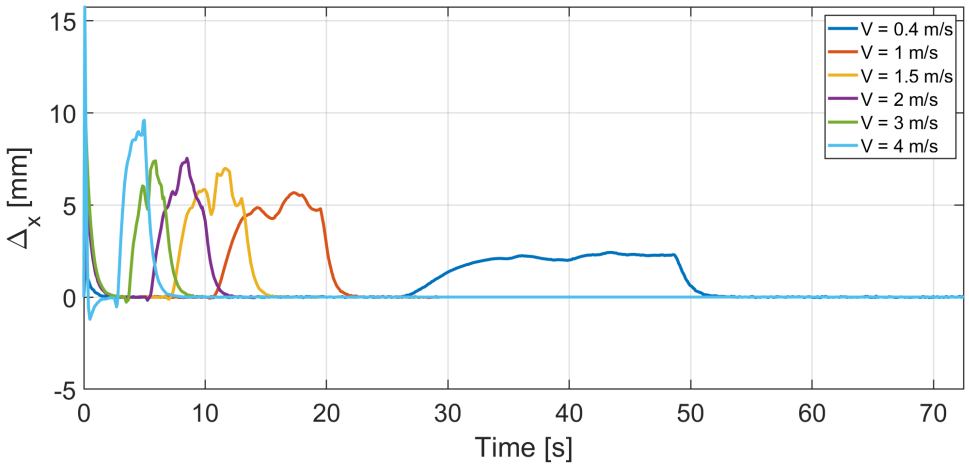

Figure 4.31: Longitudinal error - Speed sensitivity test (Independent steering)

In Figure 4.32, the trend of lateral error is shown as the vehicle speed varies. It is evident that the lateral error remains relatively unaffected by changes in vehicle speed, maintaining a value close to *3 mm* while the vehicle navigates through turns. However, as the speed increases, oscillations begin to appear, and their amplitude also increases with higher speeds. The presence of these oscillations is indicative of increasing instability as the speed rises, suggesting that the controller may struggle to maintain stability at higher velocities.

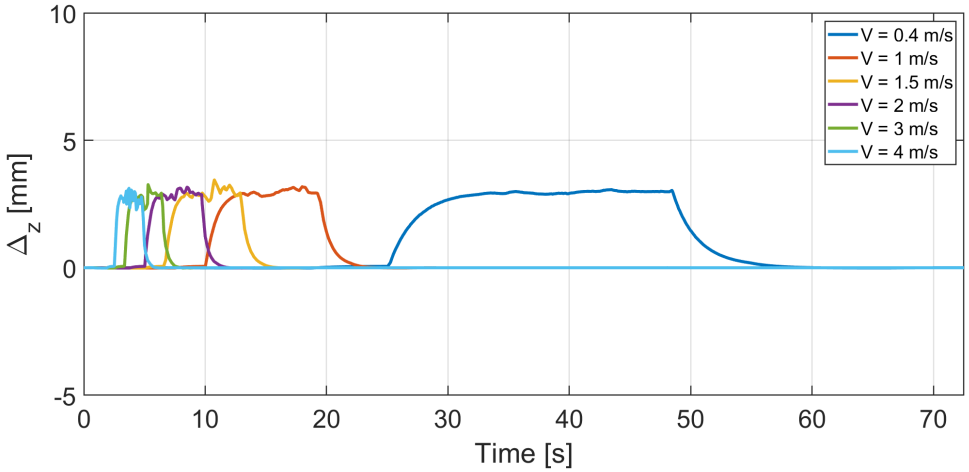

Figure 4.32: Lateral error - Speed sensitivity test (Independent steering)

The presence of oscillations in the lateral error also leads to fluctuations in the lateral force. Consequently, the maximum value of the lateral force increases as the vehicle speed rises. This observation aligns with theoretical predictions: when the vehicle speed increases, the centrifugal force, as described by Equation 11, also

increases. As a result, the lateral force exerted by each wheel rises in response to the greater centrifugal force, demonstrating how speed influences the dynamic behavior of the vehicle during turns.

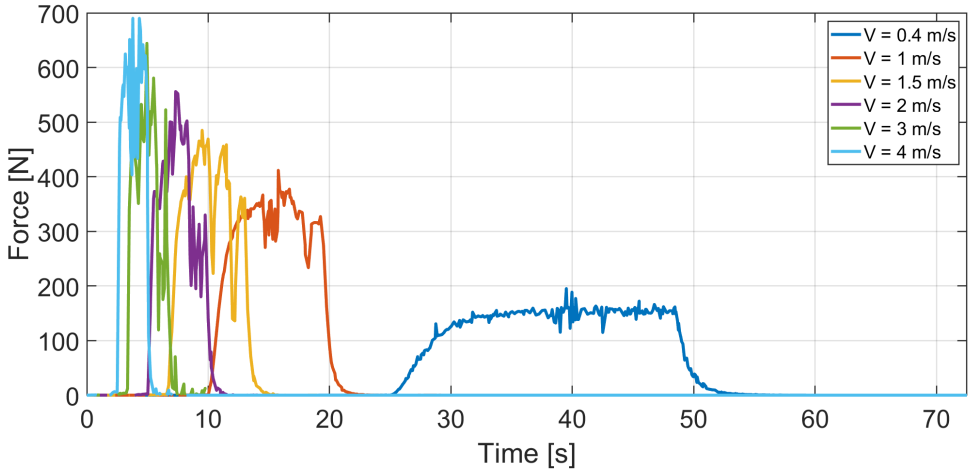

Figure 4.33: Front left force - Speed sensitivity test (Independent steering)

Since the trend of the lateral error is tied to the relationship between the desired angles assigned to the wheels, as indicated in Equation 53, an increase in speed leads to a greater number of oscillations. This suggests that more frequent adjustments to the steering are necessary to compensate for the lateral instability that arises at higher speeds.

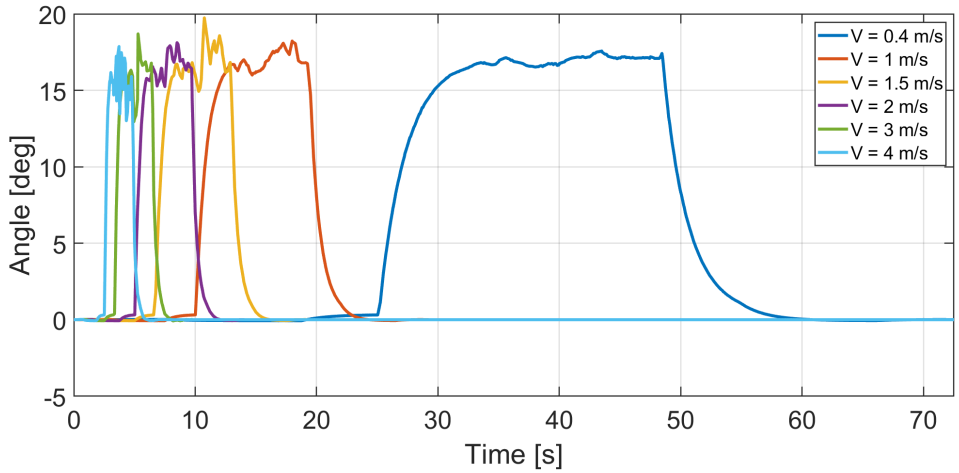

Figure 4.34: Front angle - Speed sensitivity test (Independent steering)

In the final stage of this test, the maximum speed at which the vehicle can safely navigate a turn is determined. This speed is crucial because it allows the rover to

complete the course with deviations and lateral slippage that are considered acceptable, although they may be dangerous. This threshold speed is termed the limit speed; beyond this point, the vehicle loses control, resulting in a failure of the simulation. For the independent steering system, the limit speed has been found to be slightly higher than *4 m/s*, with the exact value recorded at *4.06 m/s*. In Figure 4.35, a comparison is made between TEST 6 (*4 m/s*) and the limit case, focusing on the longitudinal error, lateral error, lateral force, and steering angles of the wheels. While the longitudinal behavior is still relevant, the lateral behavior is of greater interest for assessing vehicle stability. As shown in Figure 4.35(b), numerous oscillations emerge when the vehicle operates at its limit speed, indicating instability. Once this instability is reached, as depicted in Figure 4.35(c), the lateral force can briefly drop to zero, suggesting that the vehicle is sliding laterally. Fortunately, due to the well-tuned controller, the vehicle can regain its trajectory. In response to the lateral error, the steering angle is adjusted accordingly. In Figure 4.35(d), as the vehicle starts to drift away from the reference trajectory, the steering angle is imposed in the negative direction to counteract this drift. Ultimately, the vehicle successfully returns to the intended path and completes the simulation, demonstrating the effectiveness of the control system even at high speeds.

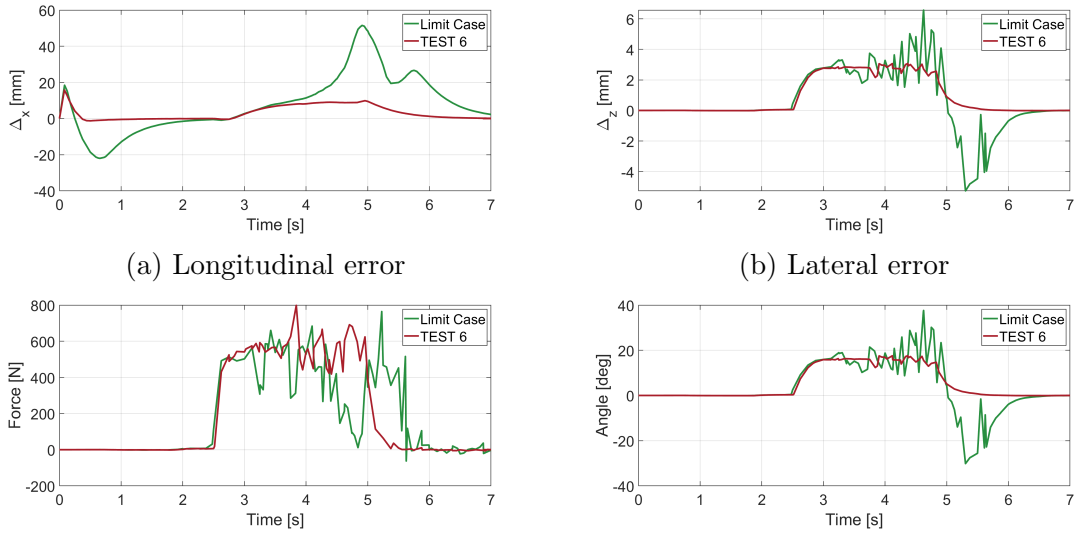

(a) Longitudinal error

(b) Lateral error

(c) Lateral force

(d) Steering angle

Figure 4.35: Comparison between Test 6 and the limit case - Independent steering

To better illustrate the instability experienced during the simulation, Figure 4.36 presents a sequence of movements captured throughout the test. The last four frames specifically depict the moments when instability occurs. In the third-to-last frame, it is evident that the vehicle is no longer aligned with the trajectory; instead, the

wheels are turned in a negative direction to correct the vehicle's orientation. This adjustment is crucial for regaining stability. By the final step in the sequence, the vehicle successfully stabilizes, demonstrating the effectiveness of the control system in responding to dynamic conditions and maintaining trajectory adherence even under challenging circumstances.

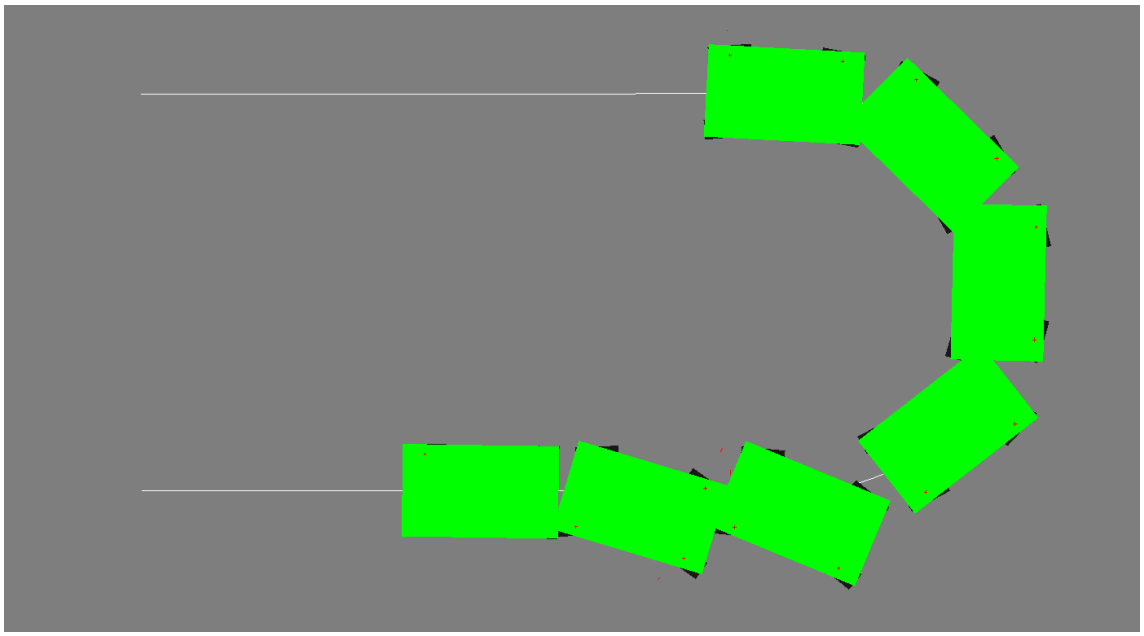

Figure 4.36: Behaviour in the limit case - Independent steering

Ackerman steering A sensitivity analysis regarding speed has been conducted for the Ackerman steering system, similar to the analysis performed for the independent steering. This analysis focuses on determining the maximum speed at which instability occurs. Although the longitudinal behavior is of lesser importance, it is examined for completeness. Figure 4.37 illustrates the longitudinal error, showing a trend consistent with that of the independent steering system. As the speed increases, the longitudinal error also increases, with values aligning closely with those obtained in the previous model.

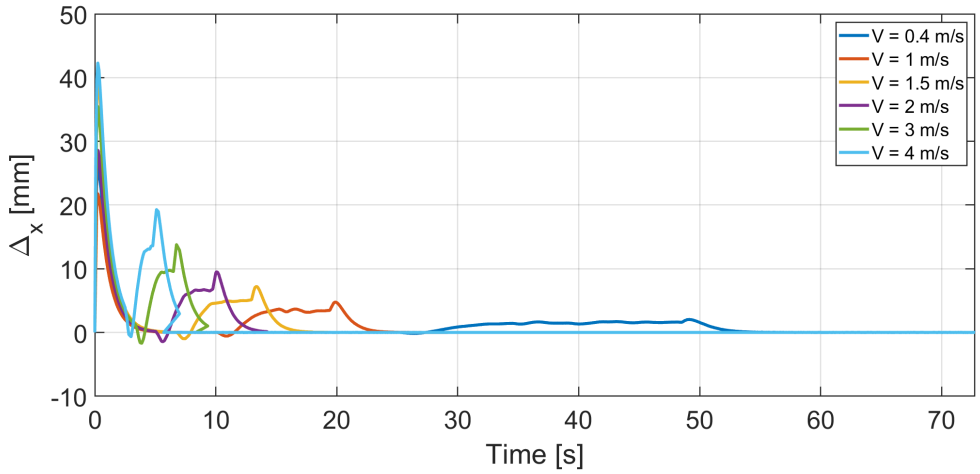

Figure 4.37: Longitudinal error - Speed sensitivity test (Ackerman steering)

In Figure 4.38, it is evident that the lateral error is not affected by changes in speed and is more stable during turns compared to the independent steering system. While the value of the lateral error is slightly higher than in the previous case, this oscillatory behavior subsequently impacts the steering angle.

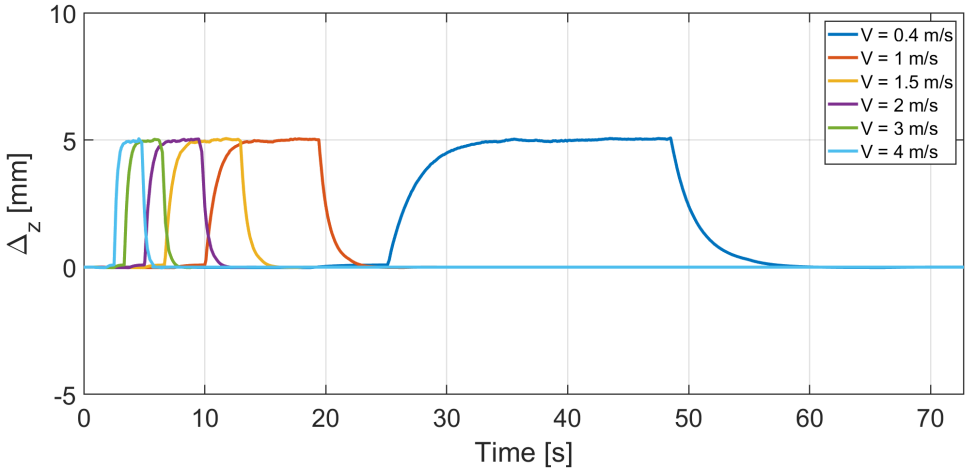

Figure 4.38: Lateral error - Speed sensitivity test (Ackerman steering)

Figures 4.39 and 4.40 illustrate the trends of the left and right wheel angles, respectively. These figures also highlight the relationship between the left and right wheels in the Ackerman steering mechanism. Even for speed of *4 m/s*, the angular corrections required are minimal, and any small oscillations can be effectively mitigated by applying a filter to the input signals.

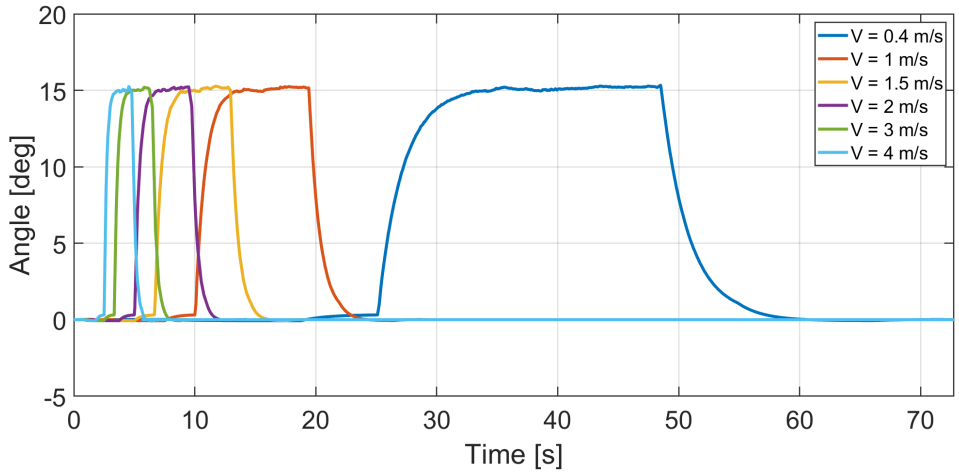

Figure 4.39: Front left angle - Speed sensitivity test (Ackerman steering)

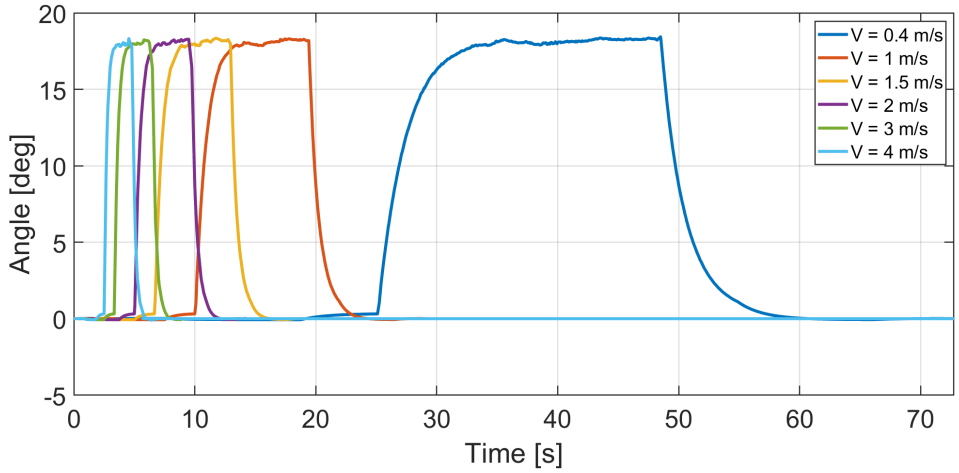

Figure 4.40: Front right angle - Speed sensitivity test (Ackerman steering)

Finally, the lateral force is examined. The observed trend aligns with theoretical expectations. To reiterate, as the vehicle speed increases, the centrifugal force also rises. Since the lateral force exerted on each wheel is a component of the total centrifugal force, it too experiences an increase.

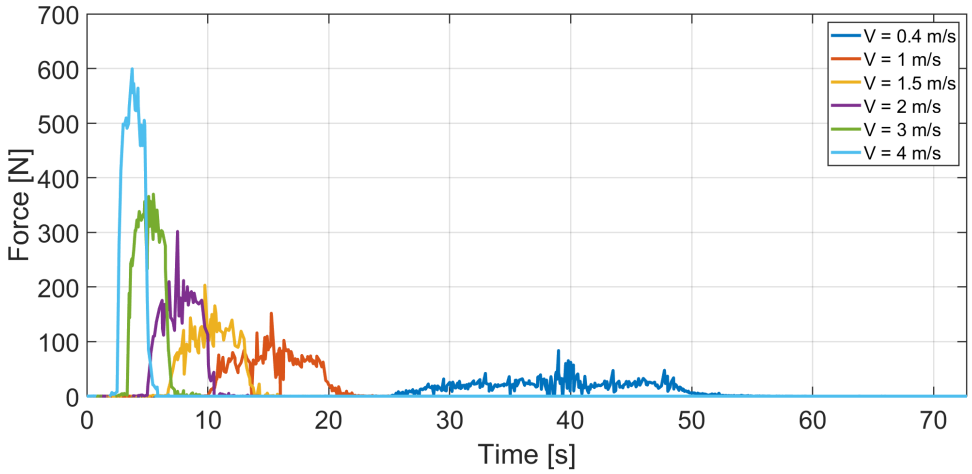

Figure 4.41: Front left force - Speed sensitivity test (Ackerman steering)

The final section investigates the maximum reachable speed. In Figure 4.42, the behavior of *TEST 6* (*4 m/s*) is compared with the identified limit case. Determining the limit speed involves a manual iterative process, where the speed is gradually increased until visible signs of instability appear. For the Ackerman steering system, the limit speed was found to be *4.5 m/s*. At this speed, the vehicle experiences lateral skidding but manages to regain control and complete the course. In Figure 4.42(b), it can be observed that during the first half of the turn, the vehicle aligns well with the reference trajectory; however, instability arises as the rover exits the turn. The lateral error oscillates around the value of *TEST 6* due to variations in the steering angle made to correct the vehicle's orientation. This unstable condition is further confirmed by the lateral force, which drops to 0 when the vehicle is no longer under control. As the vehicle attempts to realign with the reference trajectory, the lateral force increases. Figure 4.42(d) clearly illustrates how the wheels are adjusted to restore stability. Additionally, the sequence depicted in Figure 4.43 effectively shows the resulting instability and the subsequent wheel adjustments necessary to return to the correct trajectory.

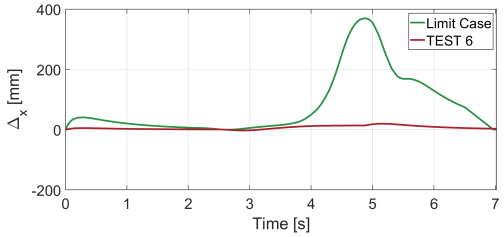

(a) Longitudinal error

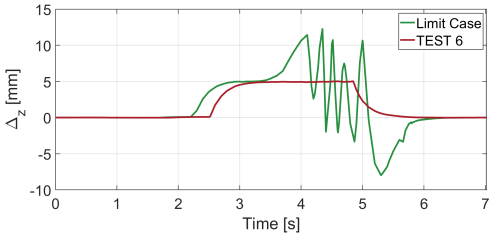

(b) Lateral error

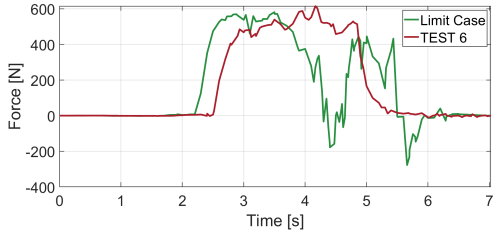

(c) Lateral force

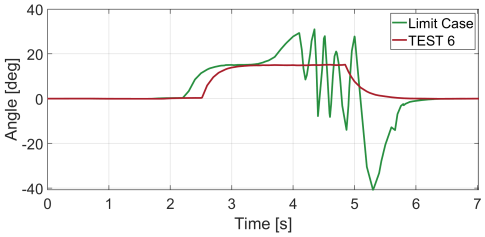

(d) Steering angle

Figure 4.42: Comparison between Test 6 and the limit case - Ackerman steering

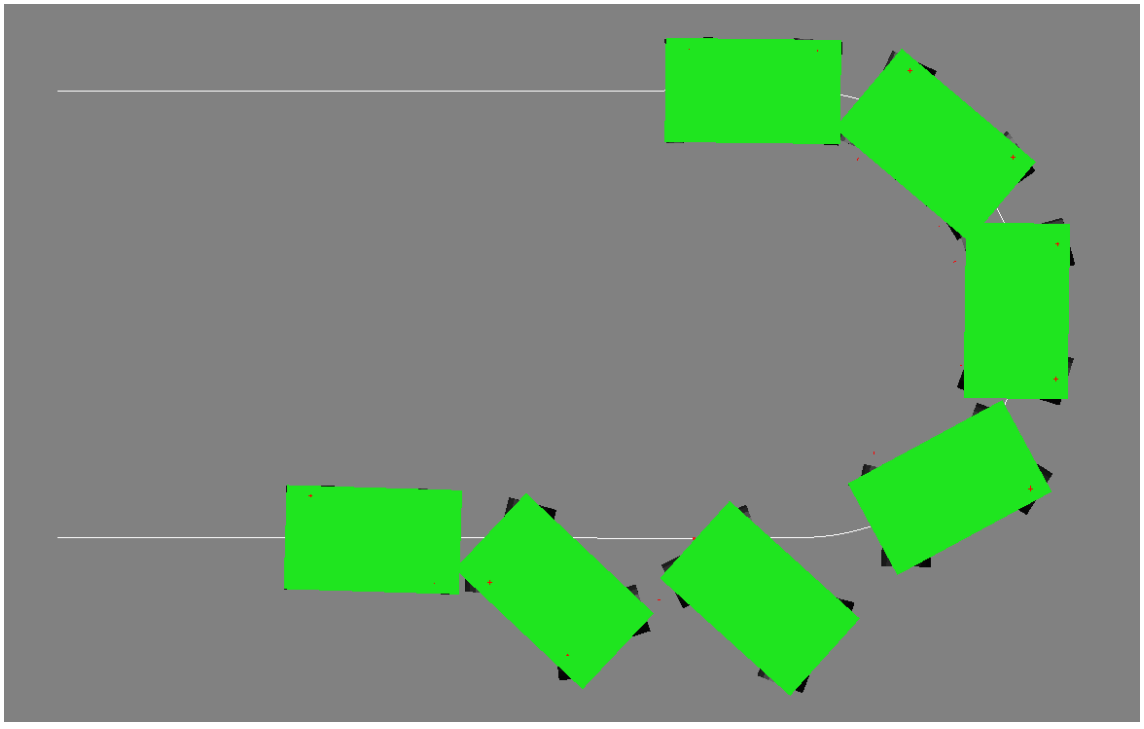

Figure 4.43: Behaviour in the limit case - Ackerman steering

Slip steering Regarding the slip steering, the sensitivity test to speed is conducted in a similar manner. Due to the instability inherent in the model, it is not feasible to complete all the speed tests listed in the table. To provide a nearly comprehensive analysis, an additional speed value is introduced; this test is labeled *TEST 5**, with

the vehicle traveling at *2.5 m/s*. Furthermore, the analysis continues with identifying the speed that induces instability, referred to as the limit speed. In Figure 4.44, the longitudinal behavior is presented, which is closely linked to the performance of the controller. When the speed is varied significantly, the controller becomes less effective. This inefficiency is particularly evident during steering maneuvers, as the vehicle experiences deceleration, which is intrinsically part of the system's dynamics.

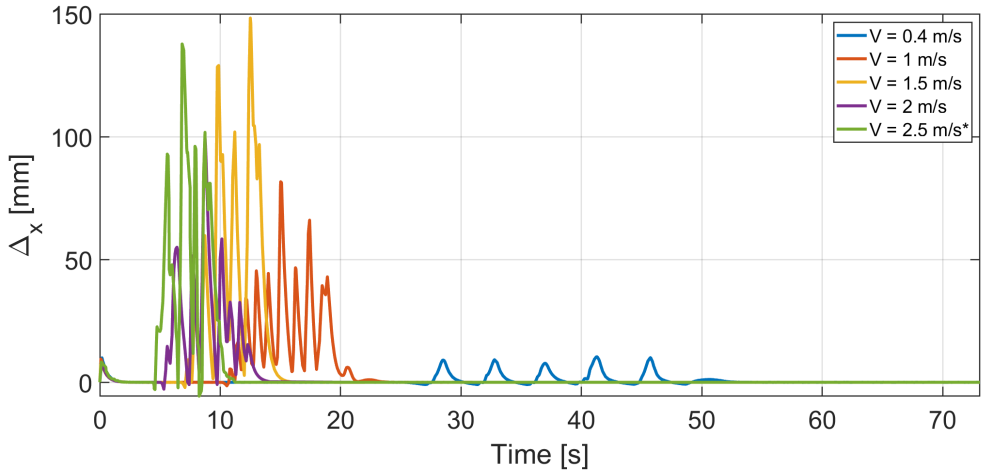

Figure 4.44: Longitudinal error sensitivity test speed - Slip steering

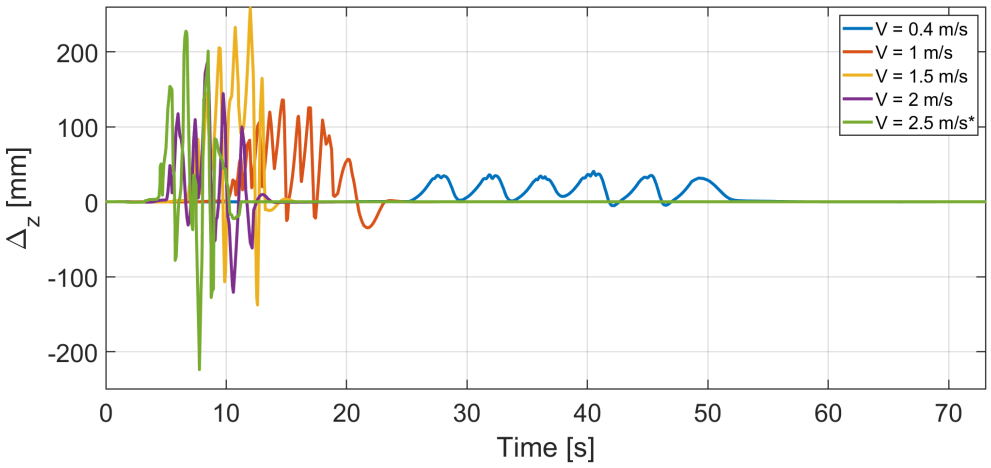

Figure 4.45: Lateral error sensitivity test speed - Slip steering

Analyzing the lateral error in Figure 4.45, it is observed that starting from *TEST 2 (1 m/s)*, the oscillations become increasingly pronounced. In *TEST 1 (0.4 m/s)*, while oscillations are present, their amplitude is small and smooth; however, at speeds beyond *TEST 2*, the oscillations become abrupt, indicating a looming instability. This phenomenon is further emphasized by the trend of the lateral force

in Figure 4.46. Notably, even at low speeds, the lateral force exhibits significant variations. These oscillations result from the jerky movement of the vehicle, and beyond *TEST 2*, this behavior intensifies, moving closer to an instability condition.

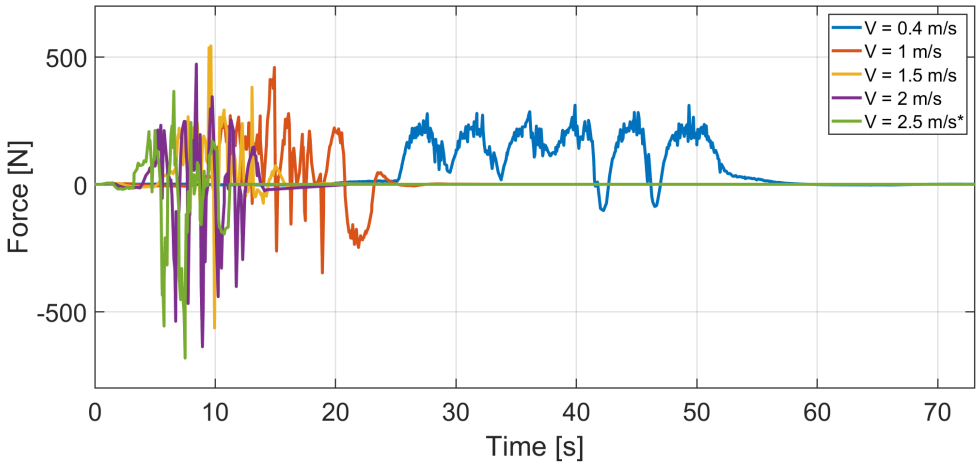

Figure 4.46: Front left force sensitivity test speed - Slip steering

The final step involves comparing the results between the limit case and *TEST 5**. First, the limit speed needs to be established. After several trials, the limit speed is determined to be *2.68 m/s*. At this speed, significant lateral oscillations and lateral movement occur, but the model can still complete the trajectory. In Figure 4.47, it is evident that the behaviors of the two cases are quite similar. As mentioned earlier, signs of instability begin to manifest from *TEST 2*, (*1 m/s*). The behavior of the limit case is illustrated through the sequence of the simulation. In the lower section, the lateral slippage during instability is clearly visible, followed by a return to the reference trajectory, with oscillations continuing around the target path until the end.

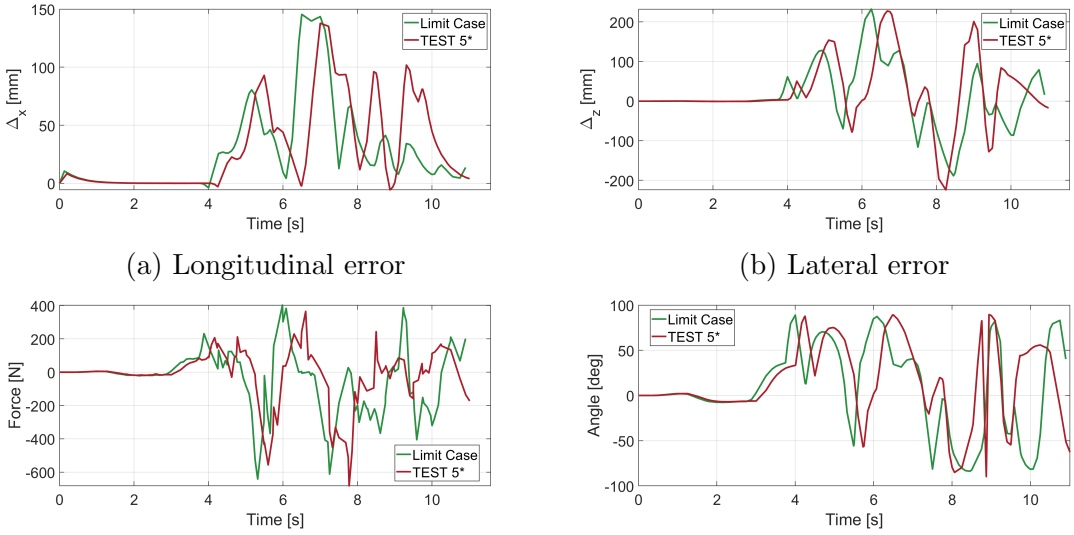

(a) Longitudinal error

(b) Lateral error

(c) Lateral force

(d) Steering angle

Figure 4.47: Comparison between Test 6 and the limit case - Slip steering

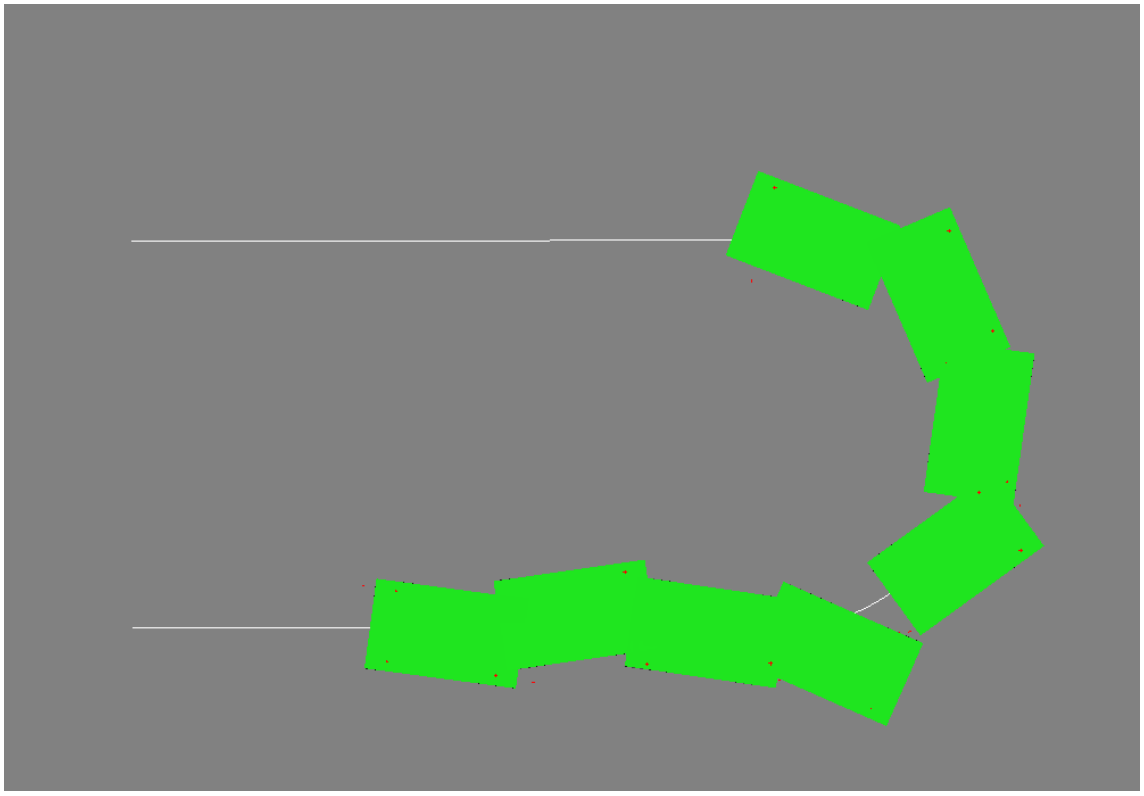

Figure 4.48: Behaviour in the limit case - Slip steering

4.1.6 Three-dimensional analyses

This section presents the results of the three-dimensional analyses. For each model, particular attention will be given to the lateral behavior, highlighting the differences in graph trends when navigating the same trajectory with and without the presence of an obstacle.

Ackerman The first model analyzed is the Ackerman steering. The longitudinal behavior is largely consistent across the three models; therefore, it will only be discussed here. In Figure 4.49, the blue line shows an initial peak caused by the obstacle-induced deceleration, followed by a negative peak as the vehicle descends from the block.

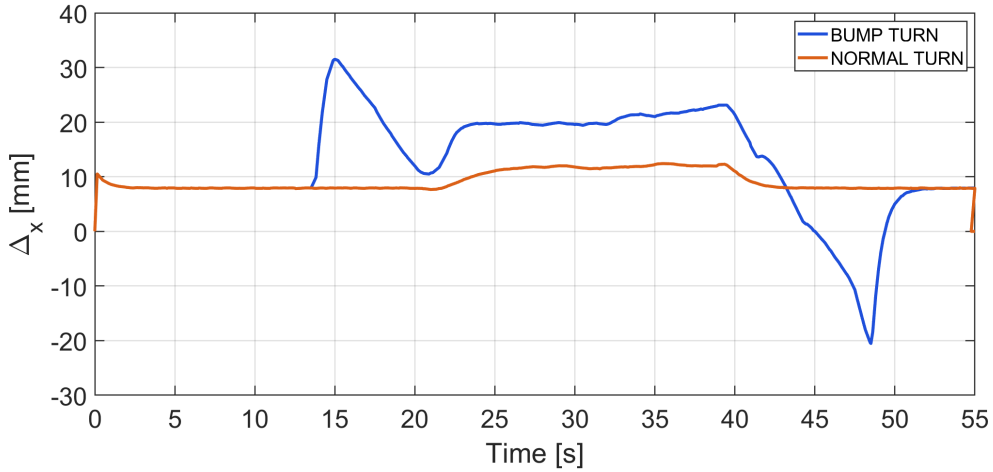

Figure 4.49: Longitudinal error with bump - Ackerman steering

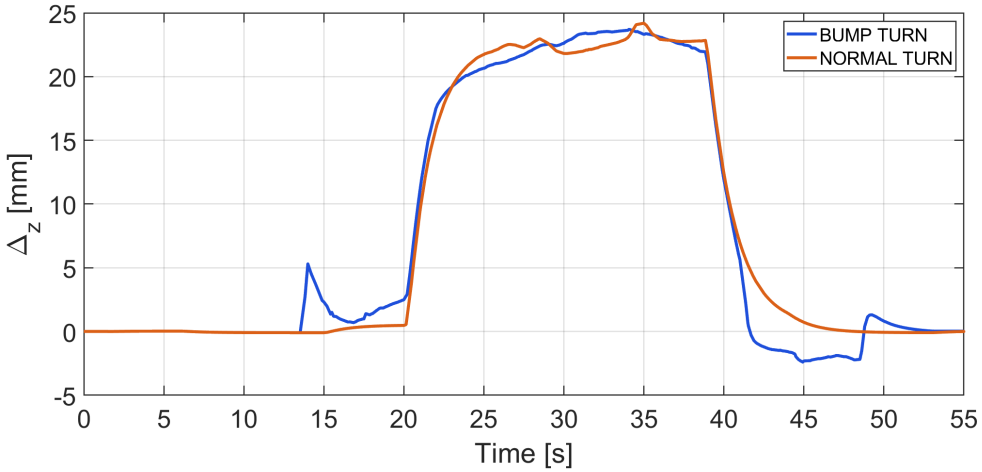

Figure 4.50: Lateral error with bump - Ackerman steering

In Figure 4.50, the impact of the bump on the lateral error is illustrated. Since the obstacle has a lateral slope, the vehicle is initially pushed outward from the curve, resulting in an increase in lateral error. After making the necessary corrections, the lateral error stabilizes and remains close to the value observed in the absence of the obstacle. Examining the trend of the vertical forces in Figures 51(a) and 51(b), we see that, as in the real prototype, when a wheel encounters the obstacle, there is an increase in vertical force for that wheel. Conversely, the opposite wheel on the same axle loses contact with the ground, leading to a drop in force to zero. Figures 51(a) and 51(b) clearly demonstrate that in the absence of the bump, the vertical force oscillates around a constant value. The resulting variations in lateral forces are depicted in Figures 52(a) and 52(b). As the vertical force increases due to the wheel rotation over the obstacle, there is a corresponding increase in lateral force.

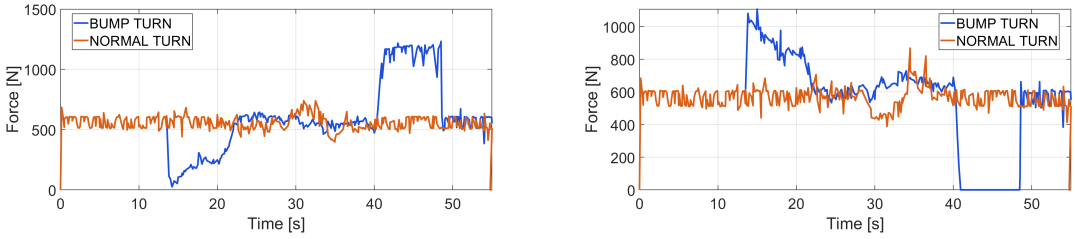

(a) Front left (b) Front right

Figure 4.51: Vertical forces - Ackerman steering

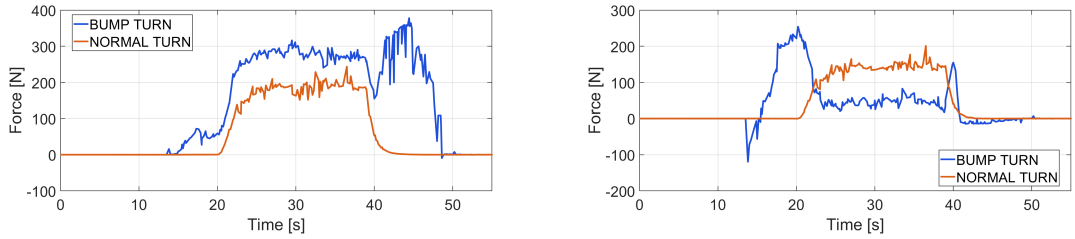

(a) Front left (b) Front right

Figure 4.52: Lateral forces - Ackerman steering

Independent steering In the case of the independent steering system, the lateral behavior closely resembles that of the previous model. An initial peak and a final peak appear due to the lateral slope of the obstacle. This disturbance results in a downward shift along the slope, leading to a lateral error even when the vehicle is traveling in a straight line. However, because the controller is well-tuned and the

steering response is effective, the lateral error remains very similar to the scenario without obstacles.

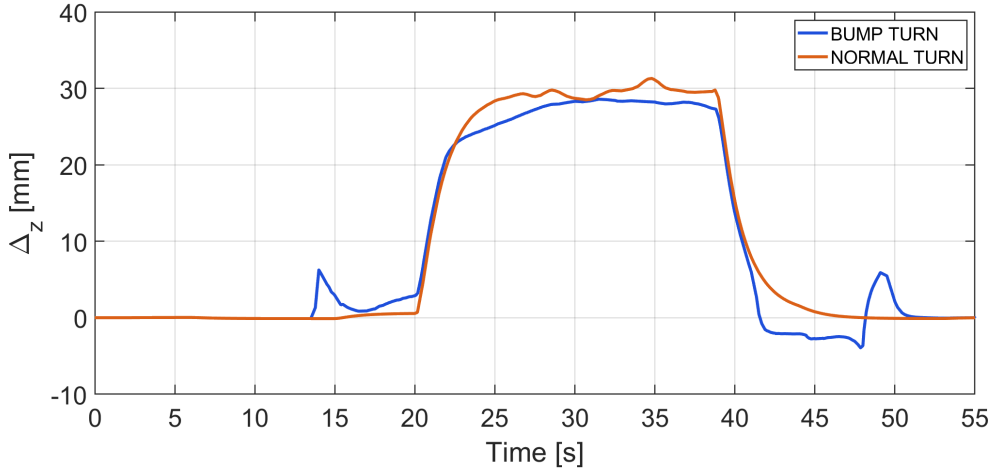

Figure 4.53: Lateral error with bump - Independent steering

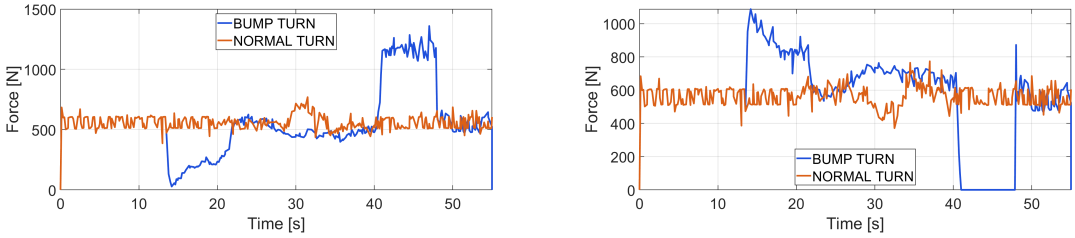

(a) Front left (b) Front right

Figure 4.54: Vertical forces - Independent steering

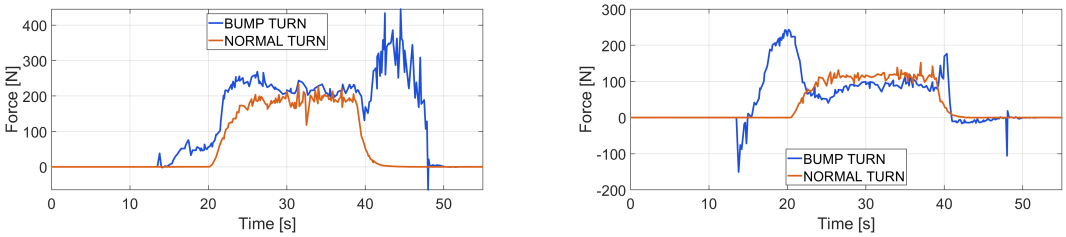

(a) Front left (b) Front right

Figure 4.55: Lateral forces - Independent steering

The data shown in Figures 4.54(a) and 4.54(b) do not differ significantly from what has been previously observed. When one wheel encounters the obstacle, the other wheel loses contact with the ground, resulting in a change in the vehicle's ability to control lateral displacement.

Slip steering In the slip steering case, this analysis underscores the poor performance of the steering system. Specifically, it becomes evident that the system struggles to maintain control, as the lateral slope leads to significant side slippage. Indeed, in Figure 4.56, the lateral error peaks at approximately *1 m*, which corresponds to the end of the obstacle laterally.

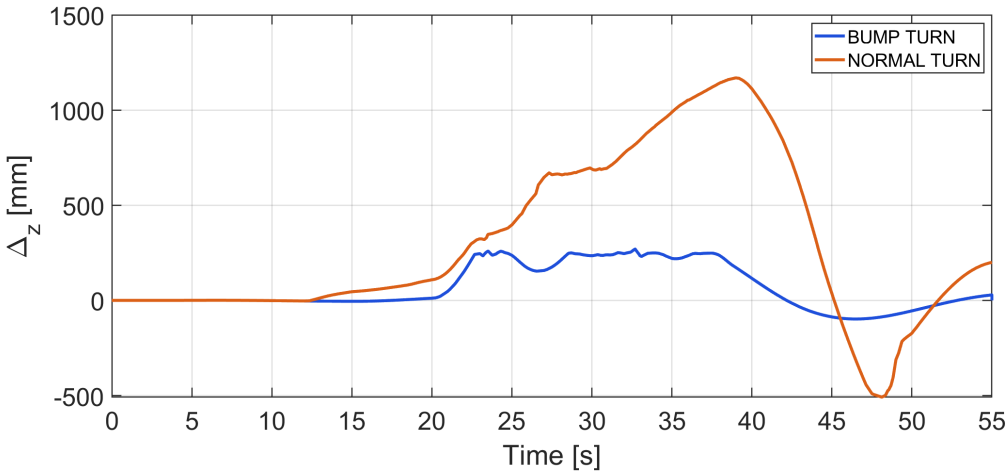

Figure 4.56: Longitudinal error with bump - Slip steering

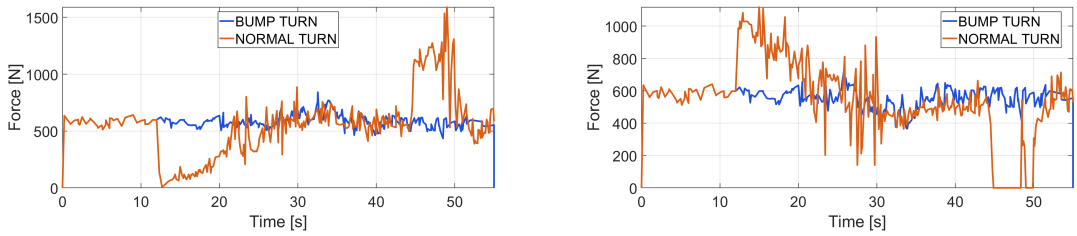

(a) Front left (b) Front right

Figure 4.57: Vertical forces - Slip steering

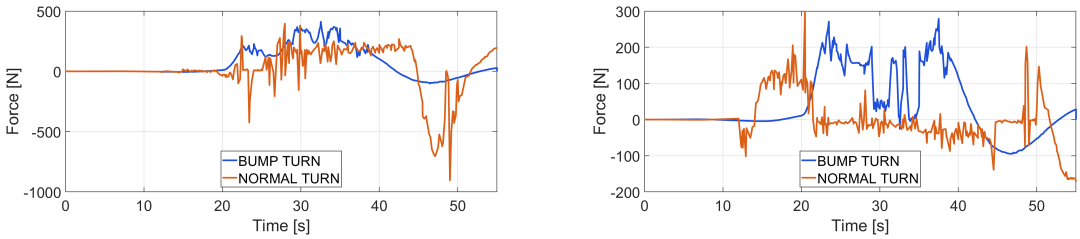

(a) Front left (b) Front right

Figure 4.58: Lateral forces - Slip steering

The trend of the vertical force aligns with the results obtained from the other models. However, the lateral force graphs present some anomalies, particularly in

Figures 4.58(a) and 4.58(b). Specifically, in Figure 4.58(b), the lateral force oscillates around 0 in the center of the graph, even though a vertical force is being applied. During this phase, the vehicle is navigating the turn, which would typically result in a lateral force greater than 0. This behavior is likely attributable to the left wheel being on flat ground, leading to excessive lateral slipping.

4.1.7 Suspension analysis

In the final part of this section, we will analyze how the presence of a suspension system can influence the behavior of the rover. Figure **??** illustrates a frame from the simulation where the front wheels are approaching the bump. In this instance, the right wheel is on the obstacle, while the left wheel in Figure 4.67(a) is in the air. In contrast, the left wheel in Figure 4.67(b) remains in contact with the ground.

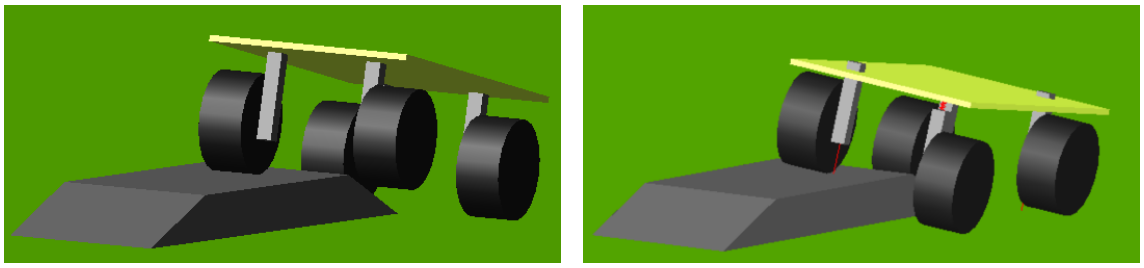

(a) Rigid chassis (b) Suspension system

Figure 4.59: Comparison between the two model

In a more concrete way, Figures 4.60 and 4.61 illustrate the trends of vertical forces in both scenarios. In the rigid chassis model, where the axle is not permitted to rotate, the wheel in contact with the obstacle experiences an increase in vertical force, while the opposite wheel, being airborne, sees its vertical force drop abruptly to zero. This behavior is evident in Figure 4.60, where the variation in forces occurs as the front axle exits the obstacle and the rear axle engages it, resulting in a reversal of behavior. Conversely, when a suspension system is implemented, the impact of the bump on vertical forces is significantly reduced. In Figure 4.61, as the right wheel ascends the bump, its reaction force against the ground experiences a slight increase, while the force on the left wheel decreases. Importantly, throughout the entire simulation, both wheels maintain contact with the ground as intended.

Ackerman As a final step, the behaviors of the two models are compared within the environment depicted in Figure 3.14, utilizing the obstacle shown in Figure 3.15. Both models employ the Ackerman steering system. The trend of the vertical

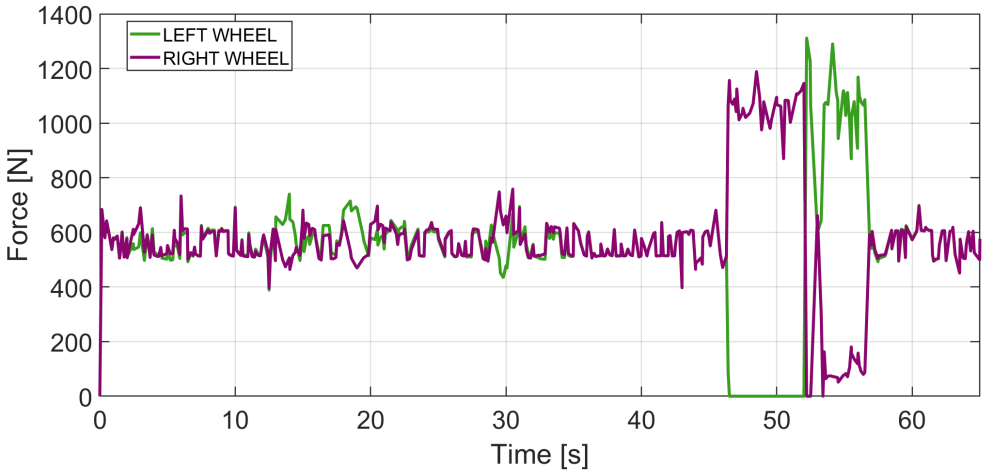

Figure 4.60: Vertical force front - Rigid chassis

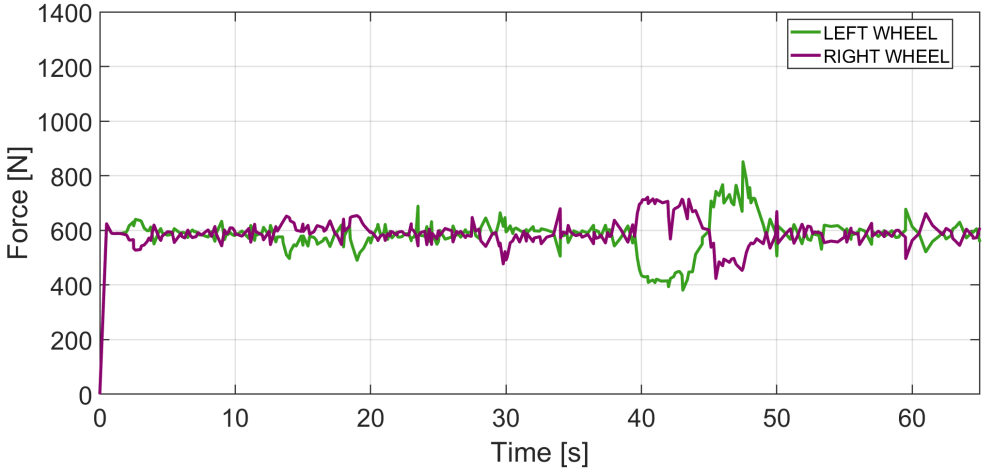

Figure 4.61: Vertical force front - Suspension chassis

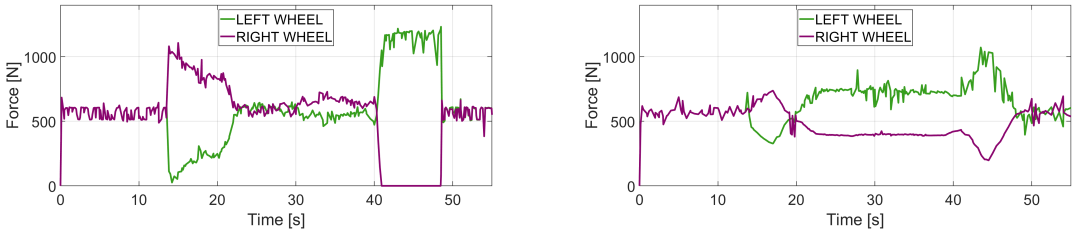

(a) Rigid chassis (b) Suspension system

Figure 4.62: Comparison vertical forces

forces remains consistent with previous observations, with variations in the values attributed to the lateral slope causing an inclination of the chassis. When a suspension system is implemented, the lateral force exhibits a smoother profile compared to

the rigid chassis model, with both the initial and final peaks being less pronounced. The presence of the suspension allows the vehicle to roll toward the slope, resulting in an increase in the roll angle. Consequently, there is a load transfer toward the left wheel, leading to a lower lateral force on the right wheel in the suspension model and a higher lateral force on the left wheel compared to the rigid chassis scenario.

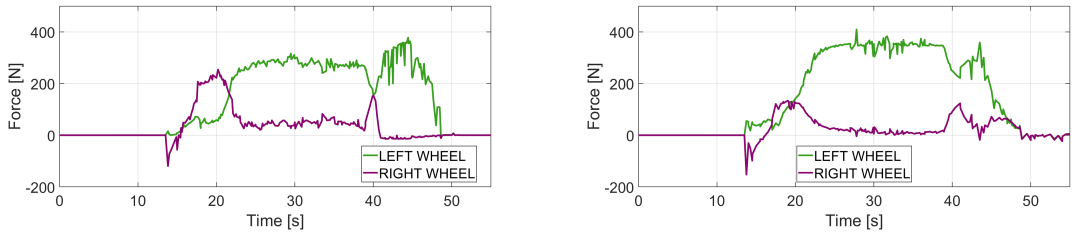

(a) Rigid chassis (b) Suspension system

Figure 4.63: Lateral vertical forces

Independent steering The findings from the turn-back test with the obstacle closely resemble those observed with the Ackerman steering. As the rover approaches the obstacle, the right wheel experiences an increase in vertical force, while the left wheel nearly loses contact with the ground. When the rear wheels also reach the obstacle, the vehicle achieves a steady-state condition. This distribution of vertical forces is influenced by the lateral slope of the obstacle. The lateral behavior also

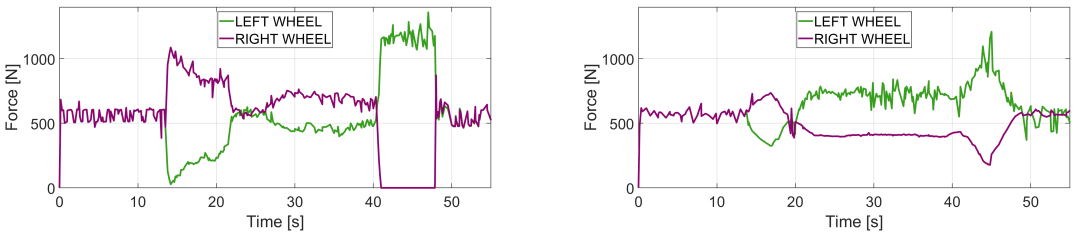

(a) Rigid chassis (b) Suspension system

Figure 4.64: Comparison vertical forces

shows similarities to the previous case. With the presence of suspension, the trend of the lateral force varies more smoothly, with the initial and final peaks being reduced.

Slip steering The behavior observed in all the previous tests is also evident here. In Figure 4.67(a), several large and rapid oscillations in the vertical forces

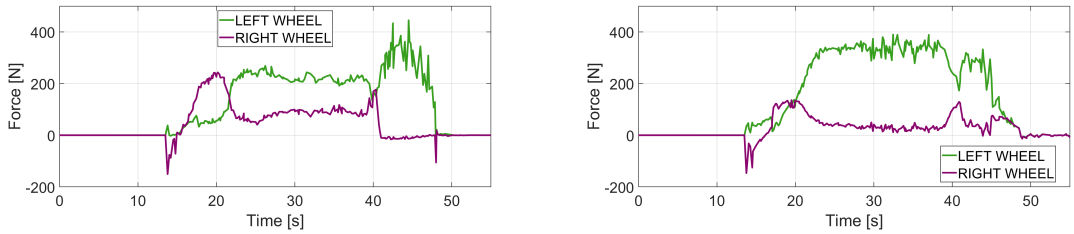

(a) Rigid chassis (b) Suspension system

Figure 4.65: Lateral vertical forces

are present, caused by the jerky movements of the rover, which are further accentuated by the lateral slope. For the slip steering system, the inclusion of suspension leads to a reduction in the peaks caused by climbing the obstacle and also minimizes the oscillations when the vehicle is in a steady-state condition. The changes in ver-

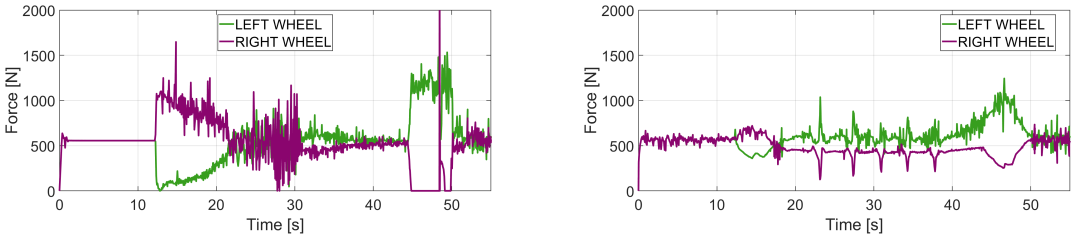

(a) Rigid chassis (b) Suspension system

Figure 4.66: Comparison vertical forces

tical load significantly impact the lateral behavior of the vehicle. As the vehicle approaches the obstacle, a peak in the lateral force of the right wheel is observed, while the force on the left wheel approaches nearly zero. The suspension system helps to dampen these rapid variations, maintaining the peaks in the steady-state region. This stabilization occurs due to the steering action of the torque, which introduces some jerking motion.

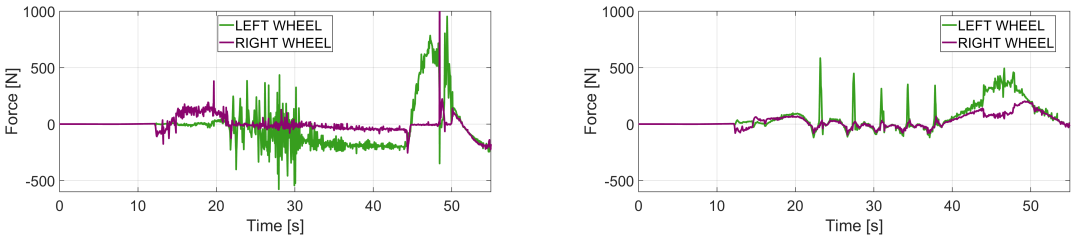

(a) Rigid chassis (b) Suspension system

Figure 4.67: Lateral vertical forces

4.2 Results evaluation

In this section are summarized the main results coming from the previous analysis, concluding with the definition of the best performing steering system.

The first observation is on the accuracy of the steering system, the most representative parameters is the lateral deviation, that, since it is measured along a reference frame integral with the chassis, it will show the lateral distance between the vehicle and the dummy body in any time instant. For all the plane test a reduction of about $80 - 90\%$ in the maximum value of the lateral deviation for both independent steering and Ackerman steering is obtained with respect the reference system, slip steering. To further highlight the accuracy, in the first analysis was also observed the position of the rear axle. In particular, the observation was highlighting how in the slip steering the rear part of the vehicle had the tendency to drag laterally, increasing the encumbrance and considering that the rover operates in an environment with physical limitations, this is certainly not an acceptable behavior. This is does not occur neither in the independent steering or in Ackerman steering system, pointing out that steering system in which is involved a rotation of the wheels around the vertical axis, regardless the type of steering, is better than the slip steering.

Regarding the lateral force in the overall test is present a reduction around $8 - 30\%$ for independent steering and around $50 - 70\%$ for Ackerman steering. This difference in the maximum values can be trace back to the wrong angle of the wheel in the independent wheel case, in sense that the angle assigned to the wheels are equal for inner and outer part of the turn. While for Ackerman it is optimize to perform an almost ideal turn. This phenomena is particularly evident in the radius sensitivity analysis, where the reduction obtained for the independent steering increases with increasing radius (from 30% to 70%), while for for Ackerman steering the increase is lower.

The influence of the speed on the lateral force is very complicated since the lateral movement the slip steering system induce increases as the speed increases and strange variations in the force are found, since the vehicle is close to an instability. Anyway it is possible to affirm that the reduction obtained is of around $10 - 60\%$ for the independent steering and is around $40 - 90\%$ for Ackerman steering. The final part of the sensitivity analyses on the speed was the research of a speed limit. The result is that the instability arise early in the slip steering case, for around 2.6 m/s the vehicle is almost perpendicular to the trajectory and the simulation failed, while for the other two cases the vehicle can reach 4 - 4.5 m/s before failure. Firstly

because the more the speed increase the more is difficult a fast variation in the torque applied at the wheel and second because it is easy and fast to correct the direction of a vehicle which can directly acts on the wheel angle.

The three-dimensional analysis reveals that the vertical force is not influenced by the type of steering. The presence of the obstacle and the lateral slope, however, peaks in the vertical forces which induce peaks and variations of the lateral forces. In presence of a lateral slope the slip steering model has difficulty in turning and tends to slide down, and the left wheels are in contact with the plane. This situation does not allow for comparison of numerical result, clearly the lateral deviation is higher for the slip steering system than the other two systems. Moreover, the behavior of the independent steering and Ackerman steering systems are comparable both for maximum lateral deviation and lateral force, those system are able to counterbalance the effect of the slope.

The last analyses results show how it could be useful introduce an element which account for the asperity of the ground, to avoid peaks in vertical force due to a lost in contact of a wheel. The sense is not to show which difference between the three models. The model propose in this thesis is able to control those behaviors and it is also compatible with the structure of the prototype. When the vehicle is on the obstacle, facing the lateral slope, the presence of the suspension induce an increase of the vertical force on the wheels on the lower side, due to the roll the suspension allow.

To conclude, the slip steering performance are in any case lower than the other two cases. One inconvenient of Ackerman steering is the limit present on the wheel angle, which affects the minimum turning radius. For the independent steering system this problem does not occur, bringing the advantage of a 0 m turning radius. Besides it offer more steering combination like crab steer or a fictitious Ackerman mechanism.

As last step it will be analysed the economic aspect of the implementation of one of the previous solutions. the cheapest of the three is definitely the slip steering system, since does not require additional motor to perform the steer. The most expensive is the independent steering system, since each wheel should have a dedicated e-motor and also a dedicated angular sensor. The cost of implementation for the Ackerman is halved with respect to the independent steering, it only requires an additional mechanism that connects the wheels on both axles.

5 Conclusion

After developing a multi-body model of the existing rover, this thesis compares three steering systems and their effects on vehicle dynamics. The first system is the one already implemented on the real rover, known as slip steering, where the steering occurs through torque differential. This system has proven to be ineffective in real-world applications, a result confirmed by the simulations. For this reason, two additional steering systems were studied, both of which implement steering through the variation of the wheel angle. The first system allows the wheels to rotate independently, with rotation occurring around the vertical axis of each wheel. The second system is a classic Ackerman mechanism, where the wheel rotation takes place around an external axis. In every test, these two new systems proved superior to the original one. Specifically, they demonstrated that the vehicle remains stable at higher speeds compared to the first case, and the variations in forces are much more gradual. A vehicle equipped with an independent steering system is undoubtedly more versatile, as it has no limitations on turning radius and can maneuver more agilely in tight spaces, while also being able to adjust the steering mode according to operational needs. However, when considering the economic aspect, this system is quite expensive. In contrast, the Ackerman steering system, which requires half the components, entails a significantly lower cost, making it a more affordable option. As the rover is currently built, both systems can be implemented. However, considering that the performance is quite similar, it is reasonable to accept a compromise between cost and versatility, and adopt the Ackerman steering system.

Regarding the possible implementation of a suspension, the proposed model does indeed offer improvements. However, it is necessary to find a way to combine the suspension with the steering system. Additionally, it is important to evaluate whether a complex suspension system is the optimal solution for this type of vehicle or if a simpler method would suffice.In conclusion, the results obtained are satisfactory and realistic enough, considering the various approximations made. However, the model can certainly be improved, starting with the treatment of the wheel-ground contact by introducing the tire as a flexible body and in particular come è considerato l'attrito.

References

[1] Antonio Carraro. URL: https://www.antoniocarraro.it/it.

[2] Vitibot. URL: https://vitibot.fr/?lang=it.

[3] Josef Kienzle Santiago Santos Valle. "Agriculture 4.0 –Agricultural robotics and automated equipment for sustainable crop production". In: *Integrated Crop Management* 24 (2020).

[4] INAIL. *Andamento degli infortuni sul lavoro e delle malattie professionali.* 2021. URL: https://www.inail.it/portale/it/attivita-e-servizi/dati-e-statistiche.html.

[5] INAIL. *Andamento degli infortuni sul lavoro e delle malattie professionali.* 2023. URL: https://www.inail.it/portale/it/attivita-e-servizi/dati-e-statistiche.html.

[6] L.Morello G.Genta. *The Automotive Chassis : System Design.* Vol. 2. Springer, 2020.

[7] Yadav R Vala VS. "Steering Geometry of Remote Control Agricultural Vehicle". In: *Ergonomics International Journal* 7 (2023).

[8] Huihuan Qian Tin Lun Lam and Yangsheng Xu. "Omnidirectional Steering Interface and Control for a Four-Wheel Independent Steering Vehicle". In: *ASME TRANSACTIONS ON MECHATRONICS* 15 (2010).

[9] Longfei Cui et al. "Design and Experiment of an Agricultural Field Management Robot and Its Navigation Control System". In: *Agronomy* 14.4 (2024). ISSN: 2073-4395. DOI: 10.3390/agronomy14040654. URL: https://www.mdpi.com/2073-4395/14/4/654.

[10] Timo Oksanen and Raimo Linkolehto. "Control of four wheel steering using independent actuators". In: *IFAC Proceedings Volumes* 46.18 (2013). 4th IFAC Conference on Modelling and Control in Agriculture, Horticulture and Post Harvest Industry, pp. 159–163. ISSN: 1474-6670. DOI: https://doi.org/10.3182/20130828-2-SF-3019.00061. URL: https://www.sciencedirect.com/science/article/pii/S1474667015349776.

[11] S.Richard Tharma M.Viswanath. "Four Wheel Steering Systems". In: *IJERT* 10 (2022).

[12] Verma Singh Sharma. "All Wheel Steering System". In: *Journal of Physical Sciences, Engineering and Technology* 7 (2015), pp. 105–108. DOI: https://doi.org/10.18090/samriddhi.v7i2.8634.

[13] BCS. URL: https://bcsagri.com/it-it/technology/dualsteer/.

[14] NewHolland. URL: https://agriculture.newholland.com/it-it/europe.

[15] Thaker Mahmood Nayl. *On Autonomous Articulated Vehicles*. 2015. URL: www.ltu.se.

[16] Hiroki Tomiyama, Michihisa Iida, and Toho Oh. "Estimation of the Sideslip Angle of an Articulated Vehicle by an Observer". In: *Engineering in Agriculture, Environment and Food* 4.3 (2011), pp. 66–70. ISSN: 1881-8366. DOI: https://doi.org/10.1016/S1881-8366(11)80014-5. URL: https://www.sciencedirect.com/science/article/pii/S1881836611800145.

[17] Michele Asperti, Michele Vignati, and Edoardo Sabbioni. "On Torque Vectoring Control: Review and Comparison of State-of-the-Art Approaches". In: *Machines* 12.3 (2024). ISSN: 2075-1702. DOI: 10.3390/machines12030160. URL: https://www.mdpi.com/2075-1702/12/3/160.

[18] Jie Tian, Jun Tong, and Shi Luo. "Differential Steering Control of Four-Wheel Independent-Drive Electric Vehicles". In: *Energies* 11.11 (2018). ISSN: 1996-1073. DOI: 10.3390/en11112892. URL: https://www.mdpi.com/1996-1073/11/11/2892.

[19] L.Morello G.Genta. *The Automotive Chassis : Components Design*. Vol. 1. Springer, 2020.

[20] Ján Dižo et al. "Multibody simulations in analyses of the vehicles' dynamics". In: *Transportation Research Procedia* 74 (2023). TRANSCOM 2023: 15th International Scientific Conference on Sustainable, Modern and Safe Transport, pp. 664–671. ISSN: 2352-1465. DOI: https://doi.org/10.1016/j.trpro.2023.11.195. URL: https://www.sciencedirect.com/science/article/pii/S2352146523004921.

[21] Francesco Mocera and Andrea Nicolini. "Multibody simulation of a small size farming tracked vehicle". In: *Procedia Structural Integrity* 8 (2018). AIAS2017 - 46th Conference on Stress Analysis and Mechanical Engineering Design, 6-9 September 2017, Pisa, Italy, pp. 118–125. ISSN: 2452-3216. DOI: https://doi.org/10.1016/j.prostr.2017.12.013. URL: https://www.sciencedirect.com/science/article/pii/S2452321617305061.

[22] Adams. URL: https://hexagon.com/it/products/product-groups/computer-aided-engineering-software/adams.

[23] Costamagna Matteo. "Studio comparativo di un modello di contatto ruota-terreno per una trattrice agricola in ambiente multibody." In: (2021).

[24] Peter Šulka et al. "Analysis and synthesis parameters influencing to the effects of impact". In: *MATEC Web of Conferences* 157 (Mar. 2018), p. 03018. DOI: 10.1051/matecconf/201815703018.

[25] Fendt. URL: https://www.fendt.com/it/.